
Electronic Thesis and Dissertation Repository

7-28-2016 12:00 AM

Development and Optimization of Solid Polymer Electrolyte for Lithium Ion Batteries

Ladan Eskandarian
The University of Western Ontario

Supervisor
Oleg Semenikhin
The University of Western Ontario

Graduate Program in Chemistry

A thesis submitted in partial fulfillment of the requirements for the degree in Master of Science
© Ladan Eskandarian 2016

Follow this and additional works at: <https://ir.lib.uwo.ca/etd>

 Part of the [Materials Chemistry Commons](#), and the [Physical Chemistry Commons](#)

Recommended Citation

Eskandarian, Ladan, "Development and Optimization of Solid Polymer Electrolyte for Lithium Ion Batteries" (2016). *Electronic Thesis and Dissertation Repository*. 3897.
<https://ir.lib.uwo.ca/etd/3897>

This Dissertation/Thesis is brought to you for free and open access by Scholarship@Western. It has been accepted for inclusion in Electronic Thesis and Dissertation Repository by an authorized administrator of Scholarship@Western. For more information, please contact wlsadmin@uwo.ca.

Abstract

This thesis focuses on the development of new poly(ethylene oxide) (PEO)-based solid polymer electrolytes (SPEs) in order to enhance their ionic conductivity at ambient temperature and fabricate the prototypes of novel Li ion batteries using these SPEs. Different types of SPEs have been developed: (i) blends of high molecular weight PEO and low molecular weight poly(vinyl acetate) (PVAc); (ii) composites of high molecular weight PEO and titanium dioxide (TiO₂) nanoparticles; and (iii) blend-based composite electrolytes consisting of PEO and PVAc with dispersed TiO₂. The SPEs were characterized by scanning electron microscopy (SEM), thermal gravimetric analysis (TGA), and differential scanning calorimetry (DSC). The electrochemical performance of the battery prototypes were determined by galvanic cycles at various current densities.

The results revealed that the crystallization of PEO was easily suppressed by blending it with PVAc. The resistance of these blends were found to decrease with an increase in the PVAc content. TiO₂ nanoparticles were found to be a compatible filler with the PEO matrix, as was proven by the lowered crystallinity, glass transition and melting temperatures of the matrix, as well as a significantly enhanced conductivity at ambient temperature.

A new type of SPE has been prepared by adding both PVAc and TiO₂ to PEO-based electrolyte. The amorphous nature of the new electrolyte was confirmed by DSC. Several prototypes of a Li-ion battery, based on this blend-based composite electrolyte and utilizing LiFePO₄ as cathode and Al as anode, were assembled and cycled at different current densities at room temperature, resulting in excellent performance. The best prototype so far showed more than 500 charge-discharge cycles with the coulombic efficiency approaching 100% and the resistance decreasing to 500 $\Omega \cdot \text{cm}^2$.

Keywords

solid polymer electrolyte, poly(ethylene oxide), poly(vinyl acetate), titanium dioxide nanoparticle, aluminum anode, lithium-ion batter

To My Family

Acknowledgments

I'd like to thank my supervisor, Dr. Oleg Semenikhin for his expert guidance over the past two years. Whenever I was frustrated and downcast over the most recent batch of seemingly nonsensical results, he would inevitably interpret the same data in a different and much more positive light.

I received incredible support from members of the Semenikhin Lab. From the first day, Mike Nieradko and David Pipher showed me the graduate school ropes. It was a pleasure getting to know Dr. Jamie Noël and Dr. Jiju Joseph, talented chemists who would always greet you with a smile. They were hard workers and willing sounding boards for discussing the finer points of electrochemistry especially impedance spectroscopy.

I'd like to give a special thanks to my undergraduate research assistant, Fareshta Zargarzadah. She helped me in lots of sample preparation and prototype cycling in the summer of 2014. A lot of thanks to my friends, Aria Khalili, Elmira Pajootan, Mehdi Rahimdokht, Mojtaba Momeni and Rohit Kulkarni who have been helpful and cooperative through all stages of my academic study. I could count on them to find the answer to literally any question, and do it with a smile.

Last I'd like to thank my parents and my sister. Despite the many miles between us, I felt their constant love and support throughout the process. They were with me for the good times and bad, and this would not have been possible without them.

Table of Contents

Abstract.....	i
Acknowledgments.....	iii
Table of Contents.....	iv
List of Tables	vii
List of Figures.....	viii
List of Schemes.....	xi
Acronyms.....	xii
Symbols	xiii
Chapter 1.....	1
1 INTRODUCTION	1
1.1 Background/motivation.....	1
1.1.1 General Views on Rechargeable Lithium Batteries	1
1.1.1.1 Negative Electrode Materials: Aluminum	3
1.1.1.2 Positive Electrode Materials	4
1.1.1.3 Electrolyte	6
1.2 Objectives	9
1.3 Contributions.....	9
1.4 References.....	10
Chapter 2.....	13
2 AN OVERVIEW OF SOLID POLYMER ELECTROLYTES	13
2.1 History of solid polymer electrolytes.....	13
2.2 Fundamentals of SPE.....	14
2.2.1 Formation of polymer-lithium salt complex	14
2.2.2 Ion conduction mechanism in SPEs.....	18
2.2.3 Phase diagram of PEO based SPE	19
2.2.4 Ion conduction in semi-crystalline SPEs.....	22
2.2.5 Approaches to improve ionic conductivity in SPEs.....	23
2.2.5.1 Composite SPEs.....	23
2.2.5.2 Blend polymers composite SPEs	26
2.3 Summary	27
2.4 References.....	28
Chapter 3.....	32

3 MATERIALS AND METHODS.....	32
3.1 Materials	32
3.2 Apparatus	32
3.3 Aluminum and Copper Substrate Preparation.....	33
3.4 Cathode Preparation	33
3.5 Preparation and Spin-Coating of SPE.....	34
3.6 Solid Polymer Electrolyte Properties and Electrochemical Characterization Summary	35
3.7 Lithium-Ion Battery Coin Cell Assembly and Testing	37
3.8 Characterizations.....	38
3.8.1 Electrochemistry Techniques and Methodology used in Lithium-Ion Battery Research	38
3.8.1.1 Galvanic Cycling.....	38
3.8.1.2 Determination of the IR drop from galvanic cycles.....	40
3.8.1.3 Analysis of the potential vs. time.....	42
3.8.2 Morphological analysis.....	43
3.8.2.1 Scanning Electron Microscopy (SEM)	43
3.8.3 Thermal analysis	44
3.8.3.1 Thermogravimetric Analysis (TGA).....	46
3.8.3.2 Differential Scanning Calorimetry (DSC)	46
3.8.4 Data Accuracy and Precision	46
3.9 References.....	49
Chapter 4.....	50
4 PREPARATION AND STUDIES OF THE POLYMER COMPOSITES TO BE USED AS ELECTROLYTES IN LI ION BATTERY PROTOTYPES	50
4.1 Thermal behaviour of SPEs with different contents of PVAc	51
4.1.1 DSC analysis.....	51
4.1.2 TGA analysis	53
4.2 Thermal behaviour of SPEs with different contents of TiO ₂	54
4.2.1 Differential scanning calorimetry (DSC).....	54
4.2.2 TGA measurements.....	56
4.3 Thermal behaviour of SPEs with the optimum contents of PVAc and TiO ₂	57
4.3.1 DSC analysis.....	57
4.3.2 TGA analysis	58
4.3.3 Transport mechanism of ions in the PEO-PVAc-TiO ₂ system	59
4.4 Summary	61
4.5 References.....	62

Chapter 5.....	64
5 ELECTROCHEMICAL PROPERTIES OF LI ION BATTERY PROTOTYPES WITH SOLID POLYMER ELECTROLYTES	64
5.1 Galvanic cycles of the battery prototypes	64
5.2 Solid polymer electrolytes with different contents of PVAc	68
5.3 Solid polymer electrolytes with different contents of TiO ₂	71
5.4 Solid polymer electrolyte with the optimum contents of PVAc and TiO ₂	73
5.5 Determination of the properties of the electroformed nanostructure from the resistances and discharging potentials	77
5.6 The performance of the best battery prototype made using PPT solid polymer electrolyte	81
5.7 References.....	87
Chapter 6.....	89
6 CONCLUSIONS AND FUTURE WORK	89
Curriculum Vitae	92

List of Tables

Table 1.1: Electrochemical parameters of several cathode materials.....	5
Table 2.1: Typical polymer hosts with their structure and glass and melting temperatures, reproduced from ref. [22].....	17
Table 3.1: Apparatus used in experiments.	33
Table 3.2: SPEs with different contents of PVAc and their battery prototypes testing procedure.....	35
Table 3.3: SPEs with different contents of TiO ₂ and their battery prototypes testing procedure.	36
Table 3.4: SPEs with different contents of PVAc and TiO ₂ and their battery prototypes testing procedure	36
Table 3.5: Confidence intervals for various values of resistance of SPEs at different current densities....	48
Table 4.1: Properties of solid polymer electrolytes with different contents of PVAc were obtained from DSC heating scans (10°C per minute).	51
Table 4.2: Properties of solid polymer electrolytes with different contents of PVAc were obtained from TGA analysis (heating rate 10°C/min).	53
Table 4.3: Properties of solid polymer electrolytes with different contents (wt.%) of TiO ₂ were obtained from DSC heating scans (10°C per minute).	54
Table 4.4: Properties of solid polymer electrolytes with different contents of TiO ₂ obtained from TGA analysis (10°C per minute).	56
Table 4.5: Properties of solid polymer electrolytes with and without 10 wt.% TiO ₂ and/or 35 wt.% PVAc obtained from DSC heating scans (10°C per minute).	57
Table 4.6: Properties of solid polymer electrolytes with and without 10 wt.% TiO ₂ and/or 35 wt.% PVAc obtained from TGA analysis (10°C per minute).	59
Table 5.1: The average resistance ($\Omega \cdot \text{cm}^2$) of solid polymer electrolytes with different contents of PVAc, with LiFePO ₄ cathode and an Al anode.....	69
Table 5.2: The average coulombic efficiency (%) of solid polymer electrolytes with different contents of PVAc, with LiFePO ₄ cathode and an Al anode.....	71
Table 5.3: The average resistance ($\Omega \cdot \text{cm}^2$) of solid polymer electrolytes with different contents of TiO ₂ , with LiFePO ₄ cathode and an Al anode.....	72
Table 5.4: The average coulombic efficiency (%) of solid polymer electrolytes with different contents of TiO ₂ , with LiFePO ₄ cathode and an Al anode.	73
Table 5.5: The average Resistance ($\Omega \cdot \text{cm}^2$) of solid polymer electrolytes with and without 10 wt.% TiO ₂ and/or 35 wt.% PVAc, with LiFePO ₄ cathode and an Al anode.....	75
Table 5.6: The average coulombic efficiency (%) of solid polymer electrolytes with and without 10 wt.% TiO ₂ and/or 35 wt.% PVAc, with LiFePO ₄ cathode and an Al anode.	77

List of Figures

Figure 1.1: Schematic of lithium-ion battery showing possible anode, cathode and electrolyte materials.	2
Figure 1.2: Chemical potential of Li as a function of mole fraction in Li/Al, from ref.[13].	4
Figure 1.3: The crystal structure of olivine LiFePO ₄ [20].	6
Figure 2.1: Summary of solid polymer electrolyte development during the last four decades adopted from ref. [21].	14
Figure 2.2: Poly(ethylene oxide), PEO, structure viewed; (a) parallel and (b) normal to the axis of the helix. The black and white circles represent oxygen and carbon atoms, respectively. Hydrogen and lithium atoms are not shown. Adopted from ref. [31].	16
Figure 2.3: Schematics of segmental motion assisted Li ⁺ cation conduction in a polymer electrolyte, circles represent ether oxygen on PEO backbone [9].	19
Figure 2.4: Phase diagrams of a series PEO-LiX electrolytes: (a) PEO-LiClO ₄ ; (b) PEO-LiAsF ₆ ; reproduced from ref. [42].	20
Figure 2.5: (a) SEM micrograph and (b) EDX sulfur map of a P(EO) ₂₀ LiCF ₃ SO ₃ SPE, reproduced from ref. [43].	21
Figure 2.6: Ionic conductivity as a function of salt content at various temperatures for (a) PEO-LiClO ₄ system; (b) PEO-LiAsF ₆ system (adapted from ref. [42]).	22
Figure 2.7: Schematic illustration of amorphous to crystalline transition in PEO based SPEs (adapted from ref. [51]).	22
Figure 2.8: Temperature dependent ionic conductivity for solution cast P(EO) _n LiClO ₄ electrolytes, reproduced from ref. [42].	23
Figure 2.9: Temperature dependent ionic conductivity of PEO-LiClO ₄ ceramic-free and nanocomposite SPEs, adopted from ref. [16].	24
Figure 2.10: Illustration of the surface interaction between Al ₂ O ₃ nanoparticles with different surface characteristics and the PEO-LiSO ₃ CF ₃ complex. Adapted from ref. [64].	26
Figure 3.1: Schematic cross-section showing the structure of a coin cell lithium-ion battery with solid polymer electrolyte.	38
Figure 3.2: A battery galvanic cycle of a prototype with a solid polymer electrolyte, LiFePO ₄ cathode and an Al anode at a current density of 6.5·10 ⁻⁵ A.cm ⁻² .	39
Figure 3.3: The typical Randles circuit.	40
Figure 3.4: The equivalent circuit for battery prototypes.	41
Figure 3.5: SEM image of battery cathode and anode before and after galvanic cycling at 6.5·10 ⁻⁵ A.cm ⁻² , (a) LiFePO ₄ -before (b) LiFePO ₄ -after at 100X magnification (c) Al-before (d) Al-after at 10000X magnification.	44
Figure 3.6: (a) DSC scan showing the key features of energy transfer processes in a polymer material; (b) thermogravimetric response illustrating the mass loss as a function of the temperature. Adapted from ref. [3].	46
Figure 4.1: Third heating DSC curves for solid polymer electrolytes with different contents of PVAc. The temperature scan range was between -100°C and 130°C. The heating rate was 10°C/min. ...	52
Figure 4.2: TGA curves for solid polymer electrolytes with different contents of PVAc. The heating rate was 10°C/min.	53
Figure 4.3: Third heating DSC curves for solid polymer electrolytes with different contents of TiO ₂ . The temperature scan range was between -100°C and 130°C. The heating rate was 10°C/min. ...	55

Figure 4.4: TGA curves for solid polymer electrolytes with different contents of TiO ₂ . The heating rate is 10°C/min.	56
Figure 4.5: Third heating DSC curves for solid polymer electrolytes with and without 10 wt.% TiO ₂ and/or 35 wt.% PVAc. The temperature scan range was between -100°C and 130°C. The heating rate was 10°C/min.	58
Figure 4.6: TGA curves for solid polymer electrolytes with and without 10 wt.% TiO ₂ and/or 35 wt.% PVAc. The heating rate is 10°C/min.	59
Figure 4.7: Polymers structure (a) PVAc, (b) PEO.	60
Figure 5.1: Battery galvanic cycles of sample with a PEPV35 solid polymer electrolyte, LiFePO ₄ cathode and an Al anode at current density of 1.3·10 ⁻⁴ A.cm ⁻² for 100 cycles.	65
Figure 5.2: Battery galvanic cycles of prototype with a PEPV35 solid polymer electrolyte, LiFePO ₄ cathode and an Al anode at current density of 1.3·10 ⁻⁴ A.cm ⁻² for 100 cycles. (a) 2 nd , (b) 50 th , (c) 100 th cycle.	66
Figure 5.3: Voltage/time profile of the last charge/discharge cycles obtained at current density of 1.3·10 ⁻⁴ A.cm ⁻² for 100 cycles for an Al/SPE/LiFePO ₄ polymer cell. See the legend for different types of SPEs.	68
Figure 5.4: Resistance of solid polymer electrolytes with different contents of PVAc, with LiFePO ₄ cathode and an Al anode at current densities of 1.6·10 ⁻⁵ , 3.2·10 ⁻⁵ , and 6.5·10 ⁻⁵ A.cm ⁻²	69
Figure 5.5: Coulombic efficiency of solid polymer electrolytes with different contents of PVAc, with LiFePO ₄ cathode and an Al anode at current densities of 1.6·10 ⁻⁵ , 3.2·10 ⁻⁵ , and 6.5·10 ⁻⁵ A.cm ⁻²	70
Figure 5.6: Resistance of solid polymer electrolytes with different contents of TiO ₂ , with LiFePO ₄ cathode and an Al anode at current densities of 1.6·10 ⁻⁵ , 3.2·10 ⁻⁵ , and 6.5·10 ⁻⁵ A.cm ⁻²	72
Figure 5.7: Coulombic efficiency of solid polymer electrolytes with different contents of TiO ₂ , with LiFePO ₄ cathode and an Al anode at current densities of 1.6·10 ⁻⁵ , 3.2·10 ⁻⁵ , and 6.5·10 ⁻⁵ A.cm ⁻²	73
Figure 5.8: Resistance of solid polymer electrolytes with and without 10 wt.% TiO ₂ and/or 35 wt.% PVAc, with LiFePO ₄ cathode and an Al anode at current densities of 1.6·10 ⁻⁵ and 3.2·10 ⁻⁵ A.cm ⁻²	74
Figure 5.9: Resistance of solid polymer electrolytes with and without 10 wt.% TiO ₂ and/or 35 wt.% PVAc, with LiFePO ₄ cathode and an Al anode at current densities of 6.5·10 ⁻⁵ , 1.3·10 ⁻⁴ , 3.2·10 ⁻⁴ , 6.4·10 ⁻⁴ A.cm ⁻²	75
Figure 5.10: Coulombic efficiency of solid polymer electrolytes with and without 10 wt.% TiO ₂ and/or 35 wt.% PVAc, with LiFePO ₄ cathode and an Al anode at current densities of 1.6·10 ⁻⁵ and 3.2·10 ⁻⁵ , A.cm ⁻²	76
Figure 5.11: Coulombic efficiency of solid polymer electrolytes with and without 10 wt.% TiO ₂ and/or 35 wt.% PVAc, with LiFePO ₄ cathode and an Al anode at current densities of 6.5·10 ⁻⁵ , 1.3·10 ⁻⁴ , 3.2·10 ⁻⁴ , 6.4·10 ⁻⁴ A.cm ⁻²	76
Figure 5.12: Discharging potential corrected for IR drop of all SPEs at different current densities and all the cycles.	78
Figure 5.13: SEM image of battery anode with SPE after galvanic cycling followed by separation from the solid polymer electrolyte and cathode at 20000X magnification, (a) PEO (b) PEPV35 (c) PT10 (d) PPT.	80
Figure 5.14: Battery galvanic cycles of sample with a PPT solid polymer electrolyte, LiFePO ₄ cathode and an Al anode at current density of (a) 1.6·10 ⁻⁵ A.cm ⁻² for 8 cycles and (b) 3.2·10 ⁻⁵ A.cm ⁻² for 8 cycles.	82
Figure 5.15: Battery galvanic cycles of sample with a PPT solid polymer electrolyte, LiFePO ₄ cathode and an Al anode at current density of 6.5·10 ⁻⁵ A.cm ⁻² for 100 cycles.	82

Figure 5.16: Battery galvanic cycles of sample with a PPT solid polymer electrolyte, LiFePO ₄ cathode and an Al anode at current density of $1.3 \cdot 10^{-4}$ A.cm ⁻² for further 100 cycles.....	83
Figure 5.17: Battery galvanic cycles of sample with a PPT solid polymer electrolyte, LiFePO ₄ cathode and an Al anode at current density of $3.2 \cdot 10^{-4}$ A.cm ⁻² for further 50 cycles.....	84
Figure 5.18: Battery galvanic cycles of sample with a PPT solid polymer electrolyte, LiFePO ₄ cathode and an Al anode at current density of $4.5 \cdot 10^{-4}$ A.cm ⁻² for further 50 cycles.....	85
Figure 5.19: Battery galvanic cycles of sample with a PPT solid polymer electrolyte, LiFePO ₄ cathode and an Al anode at current density of $5.8 \cdot 10^{-4}$ A.cm ⁻² for further 50 cycles.....	86
Figure 5.20: Battery galvanic cycles of sample with a PPT solid polymer electrolyte, LiFePO ₄ cathode and an Al anode at current density of $6.5 \cdot 10^{-4}$ A.cm ⁻² for further 100 cycles.....	87

List of Schemes

Scheme 4.1: The coordination of cation with the ester oxygen and C-O in PVAc-LiPF ₆ polymer complex. Reproduced from ref. [17].....	60
---	----

Acronyms

ACN	Acetonitrile
BSE	Back Scattered Electron
CE	Counter Electrode
CPE	Constant Phase Element
Cyc	Cycles
EC	Ethylene Carbonate
EDX	Energy Dispersive X-ray
EMC	Ethylmethyl Carbonate
EXO	Exothermic
Endo	Endothermic
DEC	Diethyl Carbonate
DSC	Differential scanning calorimetry
DMC	Dimethyl
LFP	Lithium Iron Phosphate
MEEP	Poly[Bis(Methoxy Ethoxy) Phosphazene]
NMR	Nuclear Magnetic Resonance
NMP	1-methyl-2-pyrrolidinone
PAN	Poly(Acrylonitrile)
PC	Propylene Carbonate
PEO	Poly(Ethylene Oxide)
PMMA	Poly(Methylmethacrylate)
PPO	Poly(Propylene Oxide)
PVAc	Poly(Vinyl Acetate)
PVdF	Poly(Vinylidene Fluoride)
RE	Reference Electrode
RT	Room Temperature
SEM	Scanning Electron Microscope
S.D.	Standard Deviation of Resistance
SE	Standard Error of the Mean
SPEs	Solid polymer electrolytes
TD	Degradation/Decomposition Temperature
TGA	Thermogravimetric Analysis
WE	Working Electrode
XRD	X-ray Diffraction

Symbols

A	Surface Area
C_{dl}	Double Layer Capacitance
E	Potential
E°	Standard Potential
ΔE_{ohm}	Voltage Drop
ΔH	Enthalpy
ΔH_{rec}	Recrystallization Enthalpy
ΔH_m	Heat of Fusion of Sample
$\Delta H_{m,p}$	Heat of Fusion of 100% Crystalline Sample
ΔG	Gibbs Free Energy
ΔS	Entropy
F	Faraday Constant
I	Current
μ_x	Chemical Fraction
M_w	Molecular Weight
\bar{R}	Mean value of Resistance
R	Resistance
R	Gas Constant
R_{ct}	Charge Transfer Resistance
R_e	Electrolyte Resistance
ρ	Density
σ	Ionic Conductivity
t	Value of t-statics
T	Temperature
T_c	Crystallization Temperature
T_i	Procedural Temperature
T_f	Final Temperature
T_g	Glass Transition Temperature
T_m	Melting Temperature
wt. %	Weight Percent
X_c	Crystalline Phase Content
X_i	Weight Fraction
Z_{ct}	Charge Transfer Impedance

Chapter 1

1 INTRODUCTION

1.1 Background/motivation

1.1.1 General Views on Rechargeable Lithium Batteries

Over the last decade reliance on battery technology has increased exceedingly, since the demand for portability in performing daily activities kept growing. Nowadays, lithium-ion batteries are one of the most popular energy storage technologies for sustainable energy sources due to their light weight, compact size, high energy density, high power density and the ability to be recharged and re-used many times [1].

There is an intense and rapid development of batteries; not only in terms of the improvement of their electrical performance, energy and power density, but also safety and production costs. Despite all the advances in battery science and R&D, new materials, still, need to be developed to meet the demands for portable electronic, power tools and transportation. The three most critical factors which affect the overall feasibility of the Li-ion batteries are the performance, cost and durability of energy storage.

In an electrochemical cell during the charge and discharge process, Li ions transfer across an electrolyte between the anode and cathode with oxidation and reduction occurring at the two electrodes as shown in **Fig. 1.1**. During these redox reactions at the anode and cathode, electrical energy is generated via conversion of chemical energy. Because the reactions that occur at the anode are, in general, at lower potentials than at the cathode, the terms negative and positive electrodes are also used respectively [2].

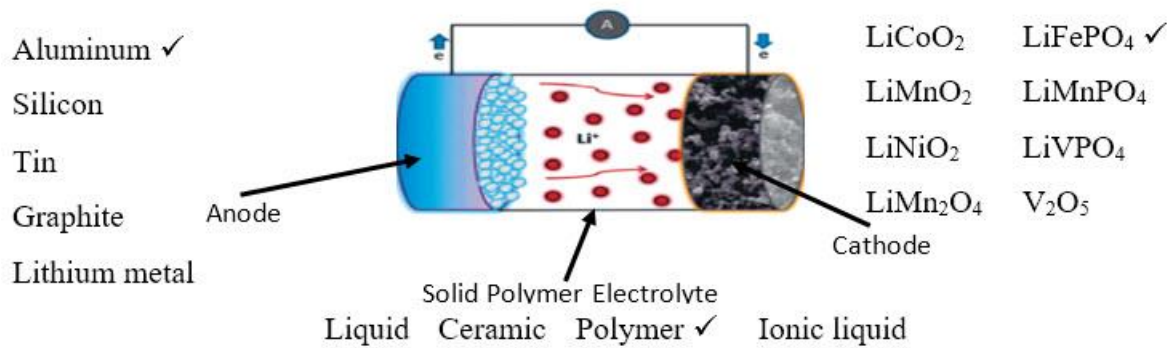


Figure 1.1: Schematic of lithium-ion battery showing possible anode, cathode and electrolyte materials.

A Li-ion rechargeable battery is, also, known as a “swing” battery since two-way movement of lithium ions between anode and cathode via the electrolyte during charging and discharging occurs. Both electrodes allow lithium ions to move in and out of their interiors. During insertion or intercalation, ions move into the electrode while during the reverse process, extraction or deintercalation, ions move back out from the electrode [3]. Lithium ions can also be accumulated at the electrodes as the result of phase formation and conversion reactions.

Before we continue it is important to clarify some terminology from the literature. In lithium ion batteries the main parameter of interest for electrode material performance is typically "capacity" (1). This term generally refers to specific capacity, gravimetric capacity or mass capacity denoting charge per mass (mAh/g). This value is often cited because it can be calculated easily with reasonable accuracy and is important for weight sensitive applications. The mass in this term is only the mass of active material of the particular electrode, not including additional mass for example from binders or collector foils. In many applications it is important for an electrode material to show good performance at a sufficiently high mass loading. In this case another term is specified, the "volumetric capacity" or charge per volume (mAh/cm³) which can be calculated from specific capacity, mass loading and the thickness of the electrode active material. Since each electrode undergoes both charge then discharge there are capacities associated with both processes, and they may differ significantly. The ratio of the capacities for the two processes in a particular cycle is termed the "coulombic efficiency" and is expressed in percent.

1.1.1.1 Negative Electrode Materials: Aluminum

The anode is the electrode where the oxidative chemical reactions takes place that give up electrons to the external circuit. In batteries, this makes the anode a negative electrode. The negative electrode material most widely used in today's Li ion batteries is graphitic carbon, also a layered material [4]. However, these materials, still, suffer from poor mechanical properties and relatively low theoretical mass capacity [5].

Many investigations have been conducted to develop new electrode materials in order to provide high power, large capacity, high rate capability and safety for the next generation of Li-ion batteries. If such an electrode is associated with a proper structure/material design to reduce the need for a separator membrane, binders, conductive additives, or current collectors, it is possible to amplify the overall battery energy density.

Silicon and tin were recently reported as higher theoretical capacity anode materials for Li-ion systems. While Si and SnO₂ anodic materials may offer very high theoretical mass or volumetric capacities, they suffer from severe irreversible capacity loss during the discharge of the first cycle [6, 7]. Therefore, one needs to continue looking for other possible replacement for graphite in Li-ion batteries.

The traditional method for alloying lithium with other metals including aluminum was mixing the metals in liquid condition at temperatures above their melting point [8]. In 1971, Dey succeeded in electrochemical alloying of metallic lithium with various metals by using lithium salts in organic carbonate electrolytes at room temperature through spontaneous reactions with high coulombic efficiency [9]. Electrochemical alloying is a more feasible method to prepare lithium alloys with metals like Sn and Al containing the same intermetallic phases and stoichiometry as thermally produced alloys. On the other hand, lithium and alloys like stainless steel and metals like copper do not form such alloys, which is the reason why these materials are widely used as common current collectors in both primary and secondary lithium batteries. Considering the low cost, wide availability, high conductivity, mechanical stability and low environmental impact of aluminum, many researchers focused on exploring aluminum anodes as a replacement for metallic lithium in primary lithium batteries [8].

Studies of Al anodes in lithium ion batteries over the past 15 years have revealed that a LiAl alloy phase is formed during lithiation/delithiation in aprotic polar carbonate solvents at room temperature [9-12]. To illustrate the electrochemical alloying behavior of LiAl at room temperature more clearly, **Fig. 1.2** shows a plot of the lithium chemical potential (in eV) versus the mole fraction of lithium in the LiAl system [13]. Overlaid near the top of the graph are the charge and discharge curves for formation and dissolution of LiAl on an Al foil electrode from an organic carbonate electrolyte with a lithium salt. The formation of LiAl phase at room temperature will be important in describing the mechanism of lithiation/delithiation for the rechargeable Al based lithium-ion batteries with solid polymer electrolyte described in this work.

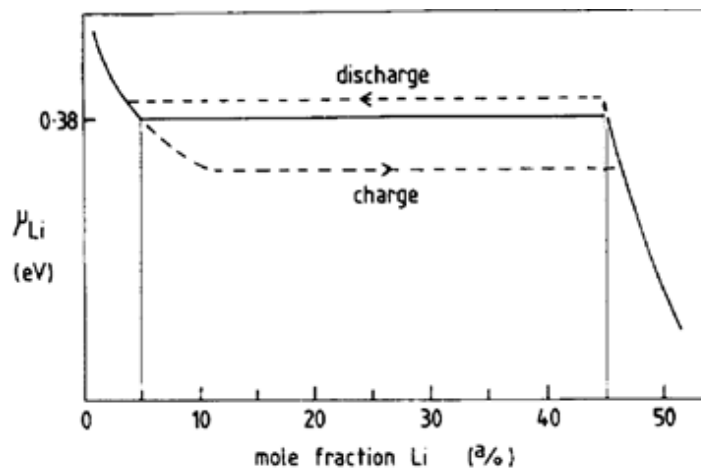


Figure 1.2: Chemical potential of Li as a function of mole fraction in Li/Al, from ref.[13].

1.1.1.2 Positive Electrode Materials

The cathode of a battery is the positive electrode which gains electrons from the external circuit and is reduced during the electrochemical reaction.

The positive electrode materials in a rechargeable lithium ion battery need to meet some crucial requirements to be successfully used [14]: the material should contain a readily reducible/oxidizable element; for example, a transition metal; the material should react with lithium ion in a reversible manner, very rapidly both on insertion and removal, and at high positive potentials. A lithium ion cell should be assembled in the discharge state; therefore, the cathode must act as a source of lithium which requires the use of air-stable lithiated intercalation compounds to facilitate the cell assembly. The properties of an ideal cathode include readily

reversible reactions, little bonding and structural modification during the charge-discharge process [15].

So-called intercalation compounds, specifically lithiated transition metal oxides, are usually used in lithium ion cells. An intercalation compound can interact with cations and electrons from external sources, forming a new compound in which the structural elements of the initial compound are maintained. Lithium ions act as guest species that can be inserted in the host lattice during discharge and extracted from the host with little structural modification [16].

Recently, transition metal phosphates such as olivine (LiFePO_4) and other lithium transition-metal phosphates, including vanadium, were demonstrated as possible candidates for cathode materials [17]. The most common cathode materials are summarized in **Table 1.1** [18].

Table 1.1: Electrochemical parameters of several cathode materials.

cathode	LiFePO_4	LiFePO_4 +5%C	LiMn_2O_4	LiCoO_2
Density/ g cm^{-3}	3.60	3.48	4.31	5.10
Potential/V	3.50	3.50	4.05	3.90
Specific capacity /mAh g^{-1}	169	159	148	274
Specific energy /Wh g^{-1}	0.59	0.56	0.56	0.98

These materials are particularly attractive because of their low cost and perceived thermodynamic and kinetic stability. The crystal structure of olivine LiFePO_4 is shown in **Fig. 1.3** [19], the olivine host FePO_4 allows a reversible insertion of Li to LiFePO_4 with a theoretical specific capacity of 169 mAh g^{-1} at a $V = 3.45$ V versus Li^+/Li^0 [18].

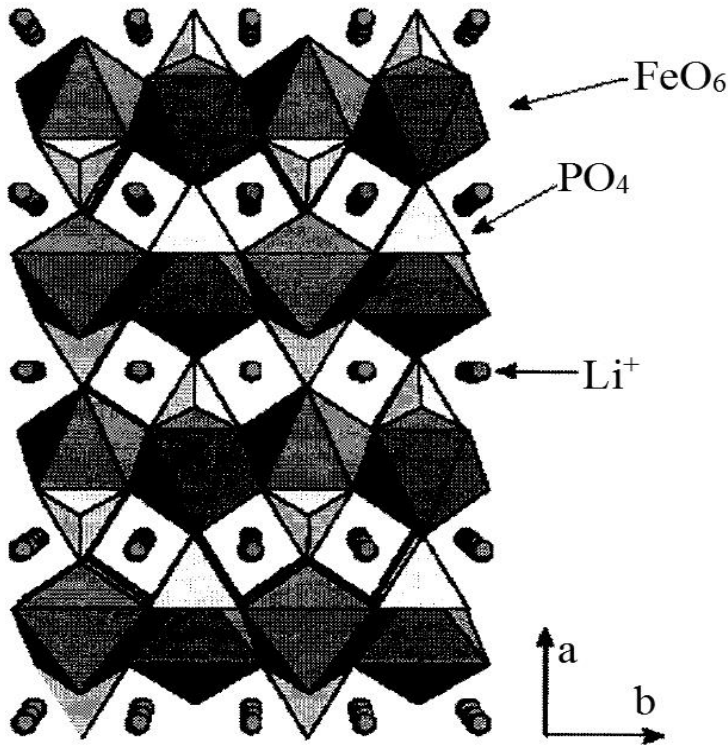


Figure 1.3: The crystal structure of olivine LiFePO_4 [20].

1.1.1.3 Electrolyte

In the charge-discharge process, lithium ions are inserted in to or extracted from the active materials of the anode and the cathode. Conceptually, the electrolyte should undergo no net chemical changes during the operation of the battery, and all Faradic processes are expected to occur within the electrodes. Therefore, in an oversimplified expression, an electrolyte could be viewed as the inert component in the battery, which must demonstrate stability against both cathode and anode surfaces. The electrolyte must have good ionic conductivity, but not be electronically conductive, as it would, otherwise, cause internal short-circuiting [21].

For a commercial Li-ion battery, the cell materials and design need to satisfy mechanical and chemical stability, high energy and power density, extensive operation temperature, safety and affordability which are some of the significant challenges in this area [22].

Four types of electrolytes have been used in lithium ion batteries: liquid electrolytes, polymer gel electrolytes, solid polymer electrolytes and ceramic electrolytes. Most of the Li-ion batteries use conventional liquid electrolytes containing a lithium salt such as LiPF_6 , LiBF_4 , LiClO_4 , LiBC_4O_8 ,

which dissolves in a mixture of organic alkyl carbonate solvents that are liquid at room temperature, like ethylene (EC), dimethyl (DMC), diethyl (DEC) and ethylmethyl (EMC) carbonate to yield high ionic and electronic conductivity. The presence of these high vapor pressure, toxic, flammable liquids requires expensive and heavy stainless steel hermetic seals to prevent leakage. This not only adds to the packaging cost and lowers the energy density, but also limits the design of thin flexible shapes and sizes. Moreover, many of these organic solvents have undesirably high reactivity towards electrodes [23].

Polymer gel electrolytes compose another category of electrolytes whose mechanical integrity is retained by crystalline phases while amorphous phase of semi-crystalline polymer is swollen by conventional liquid electrolytes (60-95%). The ionic conductivity of polymer gel electrolytes is less than that of liquid ones by 2-5 times which, still, suffices for an electrolyte in a lithium ion battery. Some examples of polymer gel electrolytes include poly(ethylene oxide) (PEO) [24], poly(acrylonitrile) (PAN) [25], poly(methylmethacrylate) (PMMA) [26], and poly(vinylidene fluoride) (PVdF) [27]. Similar to liquid electrolytes, polymer gel electrolytes, also, suffer from the presence of considerable amounts of volatile/reactive solvents.

Ceramic or glassy electrolytes are used in applications like microelectronics since they need to tolerate solder re-flow conditions typical for such applications (250°C in air or nitrogen for 10 minutes). They are produced by techniques common to the microelectronics industry (sputtering, vacuum evaporation, etc.) to form all solid state thin film batteries. Although the concentration of Li^+ in glasses is low, its conductivity is sufficient for these applications; also, many oxidizing species could be employed as positive electrodes [28-29].

Development of safe electrolytes with high ionic conductivity, a wide electrochemical window, and high stability at both electrodes is one of the prime needs in the field of Li-ion batteries today. Solid polymer electrolytes (SPEs) are formed by incorporating lithium salts into polymer matrices and casting them into thin films. There are several possible advantages with the solid polymer electrolyte compared to conventional liquid ones [30]. First and foremost, the SPE may function as a separator in a cell isolating the negative and positive electrodes from each other and preventing the cathode reaction products from diffusing to the anode side. In addition, it solves the electrolyte leakage issue, at the same time it enables the battery to have high energy density,

easy processability, a good cycle life, and flexible geometry. Compared to liquid electrolytes, solid polymer electrolytes show lower ionic conductivities and lower lithium-ion transport numbers (<0.3), yet they are less reactive towards electrodes [31-32].

In the past two decades, poly(ethylene oxide) (PEO) has emerged as a major polymer host matrix used in SPEs, and significant research efforts have been devoted to the development and improvement of PEO based SPEs. PEO features a high dielectric constant, strong lithium ion solvating ability and a glass transition temperature well below zero (around -60°C), which makes it a strong candidate to become a leading solid polymer electrolyte for Li-ion batteries [33-37]. At the same time, PEO-based polymer electrolytes have problems associated with low ionic conductivities ($<10^{-4}$ S/cm) at the near ambient operating temperatures desired for Li-ion battery applications, which is due to PEO's high degree of crystallinity (60-70%) and the regularity of the backbone at room temperature. The conduction of PEO-based solid polymer electrolytes is mainly through the ion hopping along the polymer chain assisted by the ether oxygen and in most of the cases it takes place in the amorphous region along with the long range segmental motion of the polymer chains [38, 39].

The general rule of SPE design is to suppress the PEO crystallinity in order to maximize the mobile phase for ion conduction. Such strategies include blending high molecular weight PEO with polymers having a high glass transition temperature, such as polystyrene [40], poly(methyl methacrylates) [41, 42], poly(vinyl acetate) [43], polyacryloamides [44]. Several reports have indicated improvements in the ionic conductivity due to the enhanced segmental motion of amorphous regions and interfacial stability of PEO-based polymer electrolytes by the incorporation of these polymers [45-47].

Certain ceramic nanoparticles such as TiO_2 , SiO_2 and Al_2O_3 were shown to be able to impede the PEO recrystallization process, as well as to provide specific conducting pathways along the PEO-ceramic interface and stabilize the lithium interface more efficiently. Moreover, these nanoparticles were also found to compensate and even improve the mechanical strength of solid polymer electrolyte lost due to a decrease in the degree of crystallization [32, 37, 48-51].

Although the short-term tests (several days) at room temperature illustrated the stability of ionic conduction, no report covered the long-term stability of these amorphous structures [48-50]. The

specific role of ceramic fillers is still under debate since contradictory results have been published in the literature [52-55].

Thus, one approach to prepare room temperature solid-state polymer electrolytes is to investigate composite (one polymer, one inorganic material) or blended (two polymers) solid electrolytes, in which the mechanical strength derives from one component, and the conductivity from the other component.

Overall, the impact of crystallization on ion conduction is not a simple matter due to complicated phase morphologies of semicrystalline SPEs, which are highly dependent on salt concentration, anions, and thermal history of material [56-59]. Considering the superior mechanical properties of semicrystalline polymers, they could be used in high performance SPEs which would compete with PEO based block-copolymer electrolytes and other nanocomposite SPEs, provided that the ion conductivity could be controlled and improved.

1.2 Objectives

The objective of the dissertation study is to develop solid PEO-based polymer electrolytes with improved ionic conductivity at ambient temperature, to fabricate the prototypes of novel Li ion batteries using these SPEs, and to evaluate the performance of the electrolytes and battery prototypes using them.

1.3 Contributions

This thesis is divided into 6 chapters. **Chapter 1** describes the general background, motivation and objectives of this research. **Chapter 2** gives a detailed literature review on the history, ion conduction mechanism and state-of-the-art of the development of SPEs. **Chapter 3** discusses the materials and methods, characterization techniques, and experimental setups employed in this research. **Chapter 4** presents the effect of poly(vinyl acetate) (PVAc) and TiO₂ on PEO-based solid polymer electrolyte at room temperature and formulate the best blend-based composite electrolyte with the optimum amount of PVAc and TiO₂. **Chapter 5** presents the main properties of the Li ion battery prototypes made using selected solid polymer electrolytes and discusses the morphological analysis and ion conduction behavior of the system that produced the batteries

with the best performance. **Chapter 6** includes conclusion of the outcomes from this thesis and recommendations for future work.

1.4 References

1. Armand, M.; Tarascon, J. M., *Nature*, **2008**, *451*, 7179, 652-7.
2. Horiba, T., *Proceedings of the IEEE*, **2014**, *102*, 6, 939-950.
3. Wang, Q.; Ping, P.; Zhao, X.; Chu, G.; Sun, J.; Chen, C., *Journal of Power Sources*, **2012**, *208*, 210-224.
4. Wakihara, M., *Materials Science and Engineering: R: Reports*, **2001**, *33*, 4, 109-134.
5. Winter, M.; Besenhard, J. O.; Spahr, M. E.; Novák, P., *Advanced Materials*, **1998**, *10*, 10, 725-763.
6. Courtney, I. A.; Dahn, J. R., *Journal of The Electrochemical Society*, **1997**, *144*, 6, 2045-2052.
7. Wang, J.; Wang, H.; Zhang, B.; Wang, Y.; Lu, S.; Zhang, X., *Electrochimica Acta*, **2015**, *176*, 321-326.
8. Li, Q.; Bjerrum, N. J., *Journal of Power Sources*, **2002**, *110*, 1, 1-10.
9. Nitta, N.; Yushin, G., *Particle & Particle Systems Characterization*, **2014**, *31*, 3, 317-336.
10. Lindsay, M. J.; Wang, G. X.; Liu, H. K., *Journal of Power Sources*, **2003**, *119-121*, 84-87.
11. Lei, X.; Xiang, J.; Ma, X.; Wang, C.; Sun, J., *Journal of Power Sources*, **2007**, *166*, 2, 509-513.
12. Au, M.; McWhorter, S.; Ajo, H.; Adams, T.; Zhao, Y.; Gibbs, J., *Journal of Power Sources*, **2010**, *195*, 10, 3333-3337.
13. Owen, J. R.; Maskell, W. C.; Steele, B. C. H.; Nielsen, T. S.; Sørensen, O. T., *Solid State Ionics*, **1984**, *13*, 4, 329-334.
14. Whittingham, M. S., *Chemical Reviews*, **2004**, *104*, 10, 4271-4302.
15. Linden, D. R., T. B., *Handbook of Batteries*. Third ed.; McGraw-Hill Inc.: New York, 2001.
16. Tarascon, J. M.; Armand, M., *Nature*, **2001**, *414*, 6861, 359-67.
17. Kudryavtsev, E. N.; Sibiryakov, R. V.; Agafonov, D. V.; Naraev, V. N.; Bobyl', A. V., *Russian Journal of Applied Chemistry*, **2012**, *85*, 6, 879-882.
18. Dunn, J., James, C, Gaines, LL, Gallagher, K, Dai, Q, Kelly, JC *Material and Energy Flows in the Production of Cathode and Anode Materials for Lithium Ion Batteries*; ANL/ESD-14/10 Rev.; Argonne National Laboratory: Argonne, IL USA, 2015.
19. Whittingham, M. S.; Song, Y.; Lutta, S.; Zavalij, P. Y.; Chernova, N. A., *Journal of Materials Chemistry*, **2005**, *15*, 33, 3362-3379.
20. Yuan, L.-X.; Wang, Z.-H.; Zhang, W.-X.; Hu, X.-L.; Chen, J.-T.; Huang, Y.-H.; Goodenough, J. B., *Energy & Environmental Science*, **2011**, *4*, 2, 269-284.
21. Xu, K., *Chemical Reviews*, **2004**, *104*, 10, 4303-4418.
22. Andreev, Y. G.; Bruce, P. G., *Electrochimica Acta*, **2000**, *45*, 1417-1423.
23. Baril, D.; Michot, C.; Armand, M., *Solid State Ionics*, **1997**, *94*, 1, 35-47.
24. Appetecchi, G. B.; Aihara, Y.; Scrosati, B., *Journal of The Electrochemical Society*, **2003**, *150*, 3, A301-A305.
25. Dautzenberg, G.; Croce, F.; Passerini, S.; Scrosati, B., *Chemistry of Materials*, **1994**, *6*, 4, 538-542.

26. Stallworth, P. E.; Greenbaum, S. G.; Croce, F.; Slane, S.; Salomon, M., *Electrochimica Acta*, **1995**, *40*, 13, 2137-2141.
27. Choe, H. S.; Giaccari, J.; Alamgir, M.; Abraham, K. M., *Electrochimica Acta*, **1995**, *40*, 13, 2289-2293.
28. Adachi, G.-y.; Imanaka, N.; Aono, H., *Advanced Materials*, **1996**, *8*, 2, 127-135.
29. Bouchet, R.; Miller, S.; Duclot, M.; Souquet, J. L., *Solid State Ionics*, **2001**, *145*, 1-4, 69-78.
30. Fergus, J. W., *Journal of Power Sources*, **2010**, *195*, 15, 4554-4569.
31. Armand, M., *Solid State Ionics*, **1994**, *69*, 3, 309-319.
32. Croce, F.; Appetecchi, G. B.; Persi, L.; Scrosati, B., *Nature*, **1998**, *394*, 6692, 456-458.
33. Armand, M., *Solid State Ionics*, **1983**, *9*, 745-754.
34. Armand, M. B., *Annual Review of Materials Science*, **1986**, *16*, 1, 245-261.
35. Armand, M., *Advanced Materials*, **1990**, *2*, 6-7, 278-286.
36. Hickner, M. A., *Materials Today*, **2010**, *13*, 5, 34-41.
37. Di Noto, V.; Lavina, S.; Giffin, G. A.; Negro, E.; Scrosati, B., *Electrochimica Acta*, **2011**, *57*, 4-13.
38. Bailey Jr, F. E.; Koleske, J. V., Chapter 6 - PROPERTIES OF POLY(ETHYLENE OXIDE). In *Poly (ethylene Oxide)*, Academic Press: 1976; pp 105-149.
39. Berthier, C.; Gorecki, W.; Minier, M.; Armand, M. B.; Chabagno, J. M.; Rigaud, P., *Solid State Ionics*, **1983**, *11*, 1, 91-95.
40. Gray, F. M.; Vincent, C. A.; Kent, M., *Solid State Ionics*, **1988**, *28*, 936-940.
41. Morita, M.; Ishikawa, M.; Matsuda, Y., *Journal of Alloys and Compounds*, **1997**, *250*, 1-2, 524-527.
42. Stevens, J. R.; Such, K.; Cho, N.; Wiecek, W., *Solar Energy Materials and Solar Cells*, **1995**, *39*, 2, 223-237.
43. Baskaran, R.; Selvasekarapandian, S.; Kuwata, N.; Kawamura, J.; Hattori, T., *Journal of Physics and Chemistry of Solids*, **2007**, *68*, 3, 407-412.
44. Wiecek, W.; Such, K.; Florjanczyk, Z.; Przyłuski, J., *Electrochimica Acta*, **1992**, *37*, 9, 1565-1567.
45. Gorecki, W.; Andreani, R.; Berthier, C.; Armand, M.; Mali, M.; Roos, J.; Brinkmann, D., *Solid State Ionics*, **1986**, *18*, 295-299.
46. Radhakrishnan, C. K.; Sujith, A.; Unnikrishnan, G., *Journal of Thermal Analysis and Calorimetry*, **2007**, *90*, 1, 191-199.
47. Yang, L.-Y.; Wei, D.-X.; Xu, M.; Yao, Y.-F.; Chen, Q., *Angewandte Chemie International Edition*, **2014**, *53*, 14, 3631-3635.
48. Bruce, P. G.; Scrosati, B.; Tarascon, J. M., *Angewandte Chemie (International ed. in English)*, **2008**, *47*, 16, 2930-46.
49. Quartarone, E.; Mustarelli, P., *Chemical Society Reviews*, **2011**, *40*, 5, 2525-2540.
50. Croce, F.; Persi, L.; Ronci, F.; Scrosati, B., *Solid State Ionics*, **2000**, *135*, 1-4, 47-52.
51. Croce, F.; Curini, R.; Martinelli, A.; Persi, L.; Ronci, F.; Scrosati, B.; Caminiti, R., *The Journal of Physical Chemistry B*, **1999**, *103*, 48, 10632-10638.
52. Best, A. S.; Adebahr, J.; Jacobsson, P.; MacFarlane, D. R.; Forsyth, M., *Macromolecules*, **2001**, *34*, 13, 4549-4555.
53. Marcinek, M.; Bac, A.; Lipka, P.; Zalewska, A.; Żukowska, G.; Borkowska, R.; Wiecek, W., *The Journal of Physical Chemistry B*, **2000**, *104*, 47, 11088-11093.
54. Lim, Y.-J.; An, Y.-H.; Jo, N.-J., *Nanoscale Research Letters*, **2012**, *7*, 1, 1-6.
55. Xie, J.; Duan, R. G.; Han, Y.; Kerr, J. B., *Solid State Ionics*, **2004**, *175*, 1-4, 755-758.

56. Marcinek, M.; Syzdek, J.; Marczewski, M.; Piszcz, M.; Niedzicki, L.; Kalita, M.; Plewa-Marczewska, A.; Bitner, A.; Wieczorek, P.; Trzeciak, T.; Kasprzyk, M.; P.Łężak; Zukowska, Z.; Zalewska, A.; Wieczorek, W., *Solid State Ionics*, **2015**, 276, 107-126.
57. Fullerton-Shirey, S. K.; Maranas, J. K., *Macromolecules*, **2009**, 42, 6, 2142-2156.
58. Marzantowicz, M.; Dygas, J. R.; Krok, F.; Nowiński, J. L.; Tomaszewska, A.; Florjańczyk, Z.; Zygadło-Monikowska, E., *Journal of Power Sources*, **2006**, 159, 1, 420-430.
59. Marzantowicz, M.; Dygas, J. R.; Krok, F.; Florjańczyk, Z.; Zygadło-Monikowska, E., *Electrochimica Acta*, **2007**, 53, 4, 1518-1526.

Chapter 2

2 AN OVERVIEW OF SOLID POLYMER ELECTROLYTES

2.1 History of solid polymer electrolytes

The development of solid polymer electrolytes (SPEs) started shortly after Wright *et al.* reported the semicrystalline structure in complexes between poly(ethylene oxide) (PEO) and alkali salts in 1973 [1] followed by the studies on their electrical properties [2]; subsequently, the application of these polymer-alkali salt complexes as solid electrolyte for the high-energy-density batteries was proposed by Armand due to their combined solid-state electrochemistry, flexible structure and easy processing [3]. The early mechanism to describe the correlation between morphology and conductivity of SPEs complexes was similar to inorganic ion conductors based on ion transportation through the polymer helices in the crystalline phase, yet it was soon replaced with a new mechanism describing that it is the amorphous phase that accounts for the ion conduction [4-6].

Studying the linkage between polymer segmental dynamics and ion transport largely determined the direction of SPE development in early 1980s. Several strategies were developed in order to inhibit polymer crystallization in SPEs by modification of the polymer structure with different architectures, such as comb-like type with short PEO chain and cross-linked network polymers [7-10]. Nevertheless, these approaches weakened the mechanical properties by degrading the crystallinity of the polymer, which is against the original reasons of using robust polymer membranes for safer battery applications. During the middle to late 1980s, tremendous efforts were devoted to find a balance between the fast ion transport and good mechanical properties by developing polymer blend SPEs, block copolymer SPEs and ceramic reinforced SPEs [11, 12]. Progress had been made in understanding of the SPE structure by Chatani *et al.* in 1987; they used X-ray diffraction method for the first time to find more about the crystallographic structure of a PEO:NaI 3:1 crystalline complex [13].

In the 1990s the development of “classic” PEO-based SPEs continued with efforts on increasing the charge carrier density and decoupling the ion transport from the mechanical support. Angell

et al. showed the advantage of using a novel “polymer in- salt” electrolyte with superior performance [14], besides the conventional SPE systems.

Lastly, Scrosati *et al.* developed a class of nanocomposite SPEs with enhanced mechanical, thermal and electrochemical stability as well as room temperature conductivity, which appear to be promising candidates for high performance lithium battery applications [15-17]. Bruce *et al.* discovered some P(EO)₆LiX crystalline complexes with fast ion transport that have led to reconsideration of the fundamentals of the ion conduction mechanism in polymer electrolytes [18-20]. **Fig. 2.1** gives a general summary of the development of the SPE systems during the last four decades.

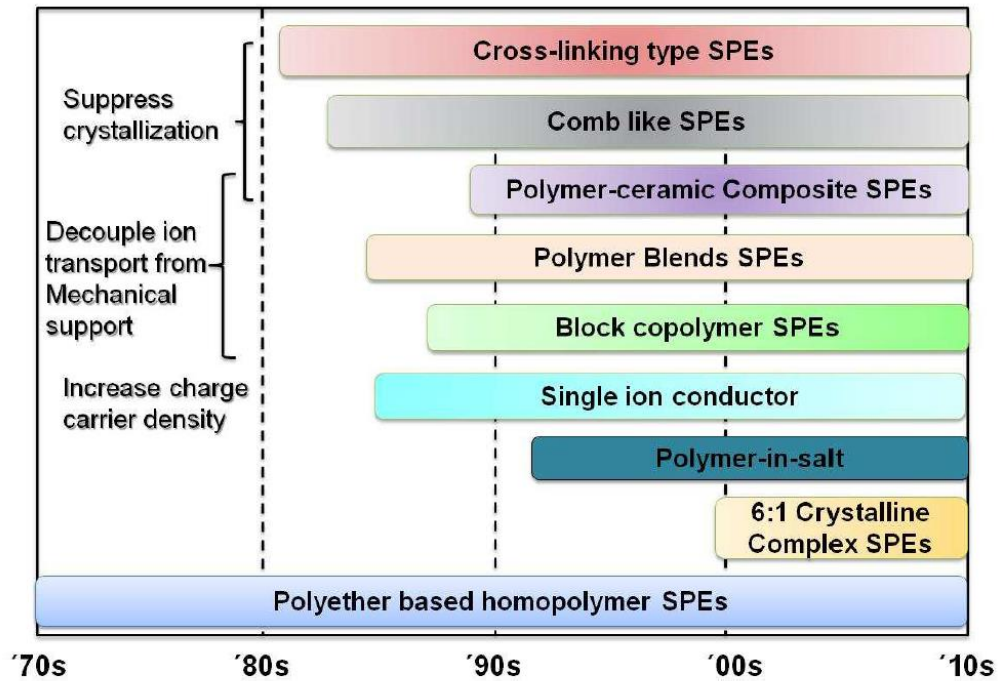


Figure 2.1: Summary of solid polymer electrolyte development during the last four decades adopted from ref. [21].

2.2 Fundamentals of SPE

2.2.1 Formation of polymer-lithium salt complex

At constant temperature and pressure, the dissolution of salt in any solvent, whether liquid or polymer, must be accompanied by a reduction in the Gibbs free energy, $\Delta G = \Delta H - T\Delta S$.

The factors that influence the change in the enthalpy include the lattice energy of the salt (high lattice energy for ions with high charges and small radii); the need to create coordination sites in the polymer (both these factors lead to positive ΔH , making the dissolution less favourable), as well as the interaction between polymer coordinating group and cation, and the electrostatic interaction between the dissolved ions, which both lead to negative ΔH , favouring the dissolution [22, 23].

The change in the entropy results from competition of two components. The entropy increases as the salt crystalline lattice is broken and ions are dissolved in the polymer. The entropy decreases as the polymer chains stiffen due to coordination with ions. This reduces the segmental motion of the polymer. It has been reported that the decrease in entropy due to the pinning of polymer chains is larger than the increase in entropy due to lattice breaking, and the net change in entropy is typically negative, disfavoring salt dissolution, especially at high temperatures at which the salt precipitates out [22, 24].

Therefore, to achieve higher room temperature conductivity, the polymer hosts should have the glass transition temperature (T_g) as low as possible since if the T_g is low enough, more amorphous regions should be available at ambient temperature for segmental mobility of the polymer chain, which could favour lithium cation transport. Similar to T_g , a lower melting point (T_m) could also produce higher ionic conductivity. Also, the polymer hosts should have the ability to dissolve lithium salts; hence, the dielectric constant of the polymer host which is related to the repeated unit of the polymer should be high [1, 6].

In summary, to effectively solvate the salt and form a polymer-lithium complex, the following basic criteria need to be satisfied for the host polymers: (i) high dielectric constant (ϵ); (ii) high electron-donor characteristics; polymers with high concentration of sequential polar groups on their backbone such as ether (-O-), sulfide (-S-), amine (-N-), phosphine (-P-), carbonyl (C=O) and cyano (C=N) are good candidates for complex formation [9, 25, 26]; (iii) appropriate distance between coordinating centers, which is best illustrated by crown ethers [27, 28]; (iv) flexible backbone and low steric hindrance for bond rotation; (v) the ease of synthesis and processing.

Poly(ethylene oxide), PEO, is a crystalline, thermoplastic, water-soluble polymer formed by ring opening polymerization of ethylene oxide, preferably catalyzed by bases or coordinated anionic polymerization catalysts [29]. PEO is soluble in water and a number of common organic solvents such as acetonitrile, anisole, chloroform, ethylene dichloride, and dimethylformamide. There are seven crystalline units in the crystalline state of PEO polymer chain: $\text{CH}_2\text{CH}_2\text{O}$, and two helical turns per fiber identity period [30]. The chains have dihedral symmetry, two-fold axes, one passing through the oxygen atoms and the other bisecting the carbon-carbon bond. The conformational assignment to internal rotation about the $\text{O}-\text{CH}_2$, CH_2-CH_2 , and CH_2-O bonds is trans, gauche, trans, respectively (**Fig. 2.2**) [22].

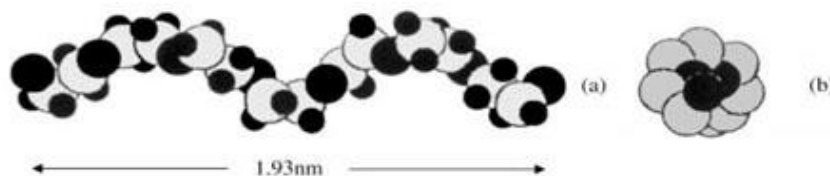


Figure 2.2: Poly(ethylene oxide), PEO, structure viewed; (a) parallel and (b) normal to the axis of the helix. The black and white circles represent oxygen and carbon atoms, respectively. Hydrogen and lithium atoms are not shown. Adopted from ref. [31].

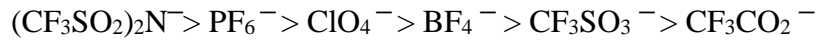
Table 2.1 lists a few selected polymer hosts, their chemical formulations and thermal characteristics. As poly[bis(methoxy ethoxy) phosphazene] (MEEP) has a low T_g , it has very high segmental motions and flexibility at ambient temperatures. Nonetheless, due to its poor dimensional stability, the room temperature ionic conductivity cannot reach the liquid electrolytes level. Poly(propylene oxide) (PPO) has a less effective solvation ability compared with PEO due to its lower dielectric constant and the stereo hindrance imposed by the additional methyl groups [26, 32]. Among the other polymers such as polysiloxanes, and poly(ethylene imine), all have shown certain capacity of complex formation with alkali metal salts [7, 32, 33], but they have limited chemical stabilities and are far less competitive compared to PEO based polyethers [25, 26, 32].

Table 2.1: Typical polymer hosts with their structure and glass and melting temperatures, reproduced from ref. [22].

Polymer Hosts	Structure	Repeat Unit	T _g (°C)	T _m (°C)
Poly (ethylene oxide)		-CH ₂ CH ₂ O-	-61	65
Poly (propylene oxide)		-CH(-CH ₃)CH ₂ O-	-60	-
Poly(dimethylsiloxane)		-Si (-CH ₃) ₂ O-	-127	-40
Poly (acrylonitrile)		-CH ₂ CH(-CN)-	125	317
Poly (methyl methacrylate)		-CH ₂ C(CH ₃)(COOCH ₃)-	105	-
Poly (ethylene imine)		-CH ₂ CH ₂ NH-		73-75
Poly (alkylene sulfide)		-CH ₂ CH ₂ S-		
Poly[bis(methoxyethoxy) phosphazene]		N=P(OCH ₂ CH ₂ OC H ₃) ₂		

Among the polymers listed, poly(ethylene oxide) PEO (CH₂CH₂O)_n has gained by far the highest popularity as a SPE. PEO has just the right spacing between coordinating ether oxygen atoms for maximum ion solvation [7, 12, 14]. PEO has the solvating properties and polarizability that are comparable to water due to the oxygen spacing in this polymer (2.88 Å), which is close to that in water (2.85 Å) [34]. This makes PEO an ideal solvent for alkali metal, alkaline-earth metal, and transition metal cations [6]. According to the hard-soft acid-base theory, the strongest interaction is between hard-hard and soft-soft matches. PEO can be considered a hard base and thus exhibits the strongest solvation with hard acids or such cations as Li⁺, Na⁺, Mg²⁺, and Ca²⁺. However, unlike water, PEO is a weak solvent for anions. The most soluble anions are large, polarizable, and have monovalent delocalized charge. The commonly used anions include ClO₄⁻, CF₃SO₃⁻,

$(\text{CF}_3\text{SO}_2)_2\text{N}^-$, PF_6^- , CF_3CO_2^- , and BF_4^- [26, 35-37]. The dissociation constant for these anions follows the order below [33, 38]:



Water has a high dielectric constant of 78 at 298K; the dipoles associated with the H_2O molecules surround the ions and reduce their association and mutual interaction. However, PEO, has a much lower dielectric constant between 5 and 8. In PEO, the ions interact strongly and re-associate to form ion clusters or ion aggregates, especially at high salt concentrations. This reduces the effect of ion dissociation during lattice breaking, decreases the entropy, and disfavours the salt dissolution. In PEO/salt complexes, the cations fit within the PEO helix, and leave empty sites around the cations to be occupied by anions [6].

2.2.2 Ion conduction mechanism in SPEs

The structure of the polymers determines their unique ion conduction mechanism. In polymers, the long range movement of the polymer chain is restricted due to entanglement. The ion conduction in polymers then occurs through a unique segmental motion assisted ion hopping mechanism. **Fig. 2.3** illustrates the mechanism of lithium cation transport through polymer chains. X-ray diffraction data have shown that Li^+ cations are located within the PEO helix. Each turn of the helix contains one Li^+ cation coordinated by three to five ether oxygens on the PEO backbone. The movement of the Li^+ cations involves breaking bonds and forming new bonds with neighbouring coordination sites assisted by the local reorganization of the PEO segments. Berthier *et al.* first demonstrated the ion migration (hopping) between coordination sites in high molecular weight semicrystalline PEO, which takes place only in the amorphous phase of the polymer above its T_g where the chain mobility is the highest [6, 32]. This phenomenon of ion conduction only in the amorphous domain limits lithium ion migration. The low lithium ion mobility, represented as low ionic conductivity at ambient temperatures, is a major obstacle in the commercialization of polymer batteries.

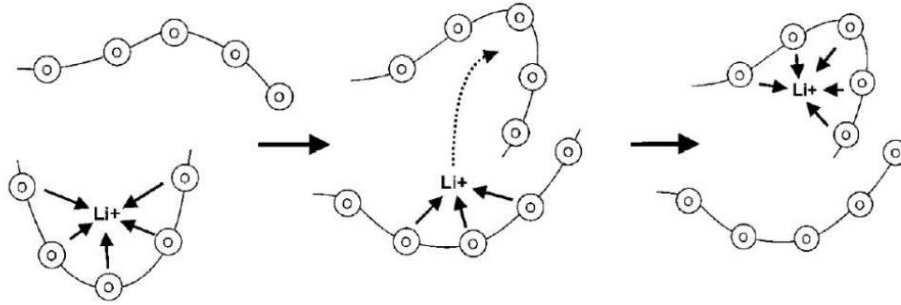


Figure 2.3: Schematics of segmental motion assisted Li^+ cation conduction in a polymer electrolyte, circles represent ether oxygen on PEO backbone [9].

2.2.3 Phase diagram of PEO based SPE

Since 1980s the phase behaviour and crystalline morphology of PEO-lithium salt SPEs have been extensively studied [5, 6, 39-44]. Several phases are defined in PEO-lithium salt SPEs: crystalline PEO phase, stoichiometric crystalline PEO-lithium complex phases, and amorphous PEO-lithium complex phase. X-ray diffraction, NMR spectroscopy, thermal analysis, and polarized light microscopy can be used to determine the number and type of phases depending on the anion identity and salt concentration as well as the thermal history [42]. Three regions of semicrystalline SPEs were defined based on the type of phases in the electrolyte at room temperature. Semi-dilute electrolytes (O/Li molar ratio around 8-20) have the most complicated morphology where multiple phases co-exist, including crystalline PEO, amorphous PEO-lithium complex phase and crystalline PEO-lithium complex phases. Concentrated SPEs (or polymer in salt) only consist of crystalline complexes with stoichiometry of 6:1, 4:1, 3:1 or 2:1 depending on the type of anion.

Fig. 2.4 shows the phase diagrams of two commonly studied PEO-lithium salt SPEs [42, 45]. Stoichiometric compound of 6:1 and 3:1 are found in SPEs containing LiClO_4 and LiAsF_6 . An eutectic with melting temperature of 50-55°C is observed for all types of SPEs at composition range $10 < \text{O/Li molar ratio} < 100$. $\text{P(EO)}_6\text{LiAsF}_6$ has a melting temperature of 136°C, which is 70°C higher than that of $\text{P(EO)}_6\text{LiClO}_4$. Most $\text{P(EO)}_3\text{LiX}$ complexes have melting temperatures above 100°C.

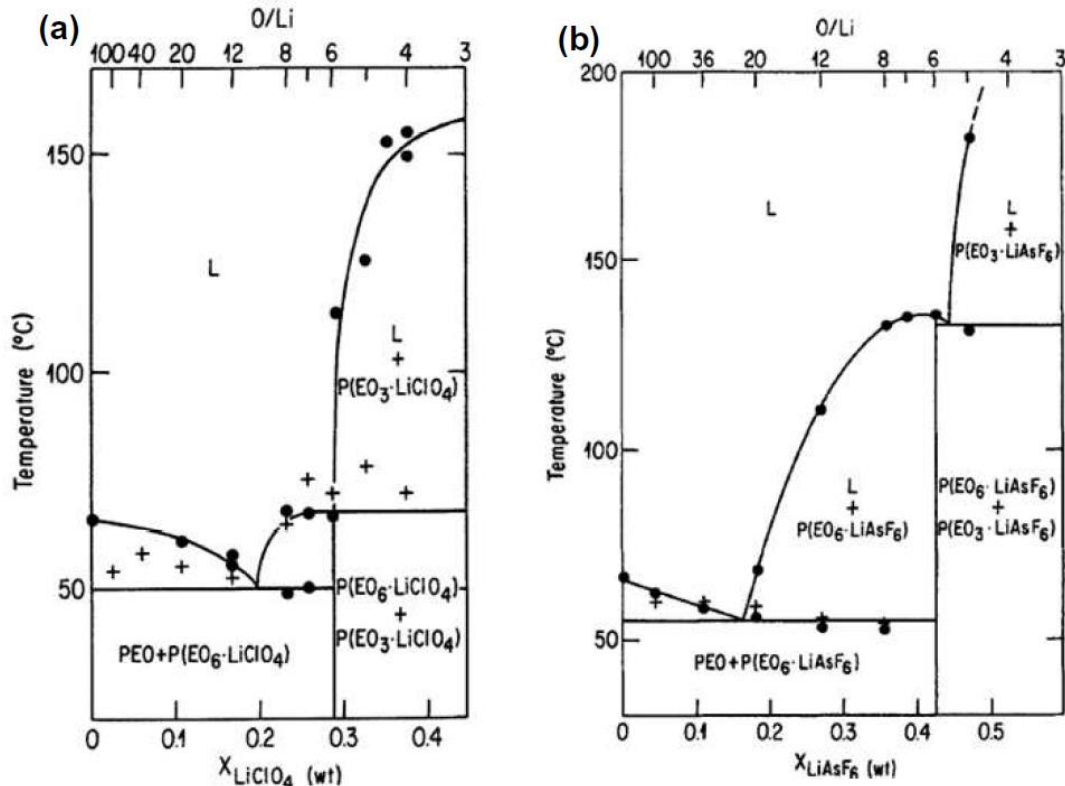


Figure 2.4: Phase diagrams of a series PEO-LiX electrolytes: (a) PEO-LiClO₄; (b) PEO-LiAsF₆; reproduced from ref. [42].

PEO crystallizes into a fringed spherulite structure in dilute SPEs due to strong interference with lithium salts as revealed by polarized light microscopy experiments [46-48]. Lithium salts which are not able to participate in crystal formation begin to concentrate within amorphous phases in the intervals between spherulites and the amorphous inter-lamellar regions. Impedance spectroscopy can be used to probe the inhomogeneity of the SPEs [49]. In semi-dilute electrolytes, both PEO-lithium complex (salt-rich) phases and PEO (salt-poor) phases crystallize into spherulitic morphology [39, 43]. SEM along with EDX analysis in **Fig. 2.5** clearly reveal the morphology and salt distribution in a P(EO)₂₀LiCF₃SO₃ SPE [43]. Those salt-rich crystalline complexes also exhibit regular and densely packed spherulitic morphology, but with higher melting temperatures [5, 6, 50].

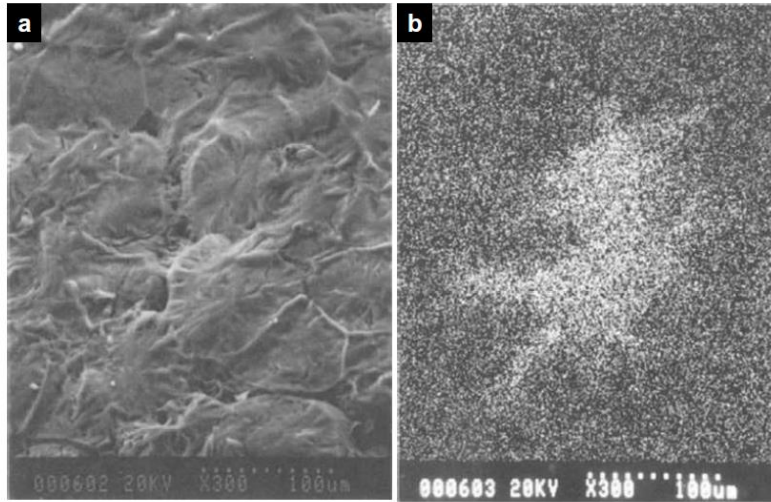


Figure 2.5: (a) SEM micrograph and (b) EDX sulfur map of a $\text{P(EO)}_{20}\text{LiCF}_3\text{SO}_3$ SPE, reproduced from ref. [43].

The overall conductivity of the polymer electrolytes is determined by (i) the number of charge carriers; (ii) degree of charge dissociation and (iii) the interaction between the ions and the polymer chain, all of which are strongly affected by the ion concentration. **Fig. 2.6** shows that the optimized conductivity of most SPEs at temperatures higher than melting point (T_m) is achieved when the O/Li molar ratio is about 8-20. Due to the increased number of charge carriers in the dilute region, the ionic conductivity increases monotonically with ion concentration. Above the optimal concentration, the ionic conductivity decreases due to significant ion pairing and physical crosslinking between polymer chain and Li^+ , as well as the formation of PEO-Li^+ crystalline complex that restricts the ion mobility. At temperatures below T_m , the concentration dependence of the ionic conductivity is complicated by PEO crystallization [42].

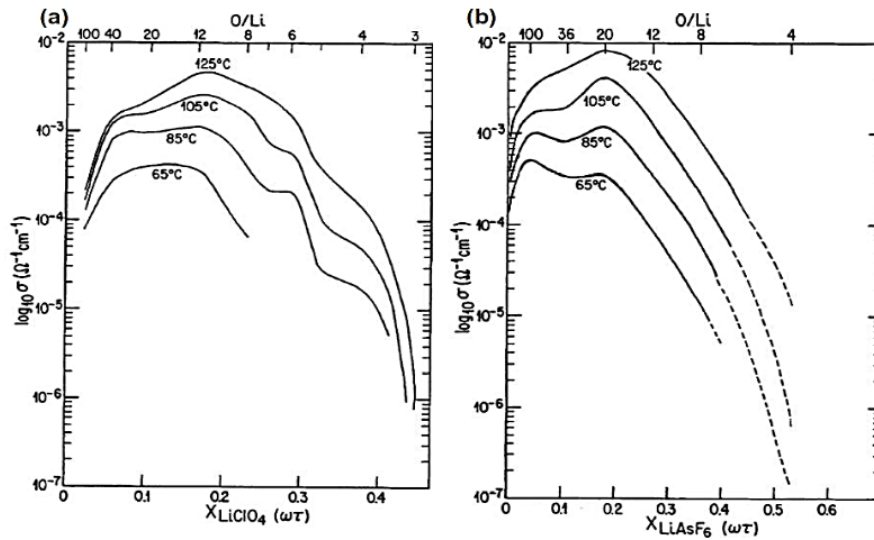


Figure 2.6: Ionic conductivity as a function of salt content at various temperatures for (a) PEO-LiClO₄ system; (b) PEO-LiAsF₆ system (adapted from ref. [42]).

2.2.4 Ion conduction in semi-crystalline SPEs

Ion conduction considerably decreases when linear PEO crystallization occurs. The crystallization of linear PEO has been long viewed as unfavourable for ion conduction. Generally speaking, the detrimental impact of crystallization can be categorized into three aspects as illustrated in **Fig. 2.7**: (i) a decrease in the effective fraction of amorphous conducting phase; (ii) restricted chain mobility (dynamic/tethered chain effect) and (iii) occurrence of more tortuous pathways for ion transport (tortuosity effect). Until now, despite numerous studies, the exact correlation between crystallization and ionic conductivity could not be determined as long as those three intertwined factors restrained the efforts to achieve a quantitative analysis.

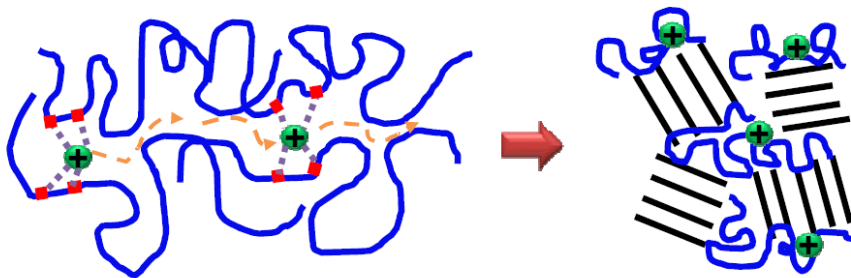


Figure 2.7: Schematic illustration of amorphous to crystalline transition in PEO based SPEs (adapted from ref. [51]).

However, the temperature dependent conductivity plots of semicrystalline PEO SPEs are helpful in understanding the degree of conductivity reduction as a result of PEO crystallization. **Fig. 2.8** is a typical conductivity plot for a series of $P(EO)_nLiClO_4$ electrolytes. There is a “knee-like” shape in conductivity diagrams for all concentration ranges when PEO temperature is close to the melting point T_m (~60 to 70°C). At temperatures below the melting point, there is a 2-3 order of magnitude drop in conductivity (down to 10^{-7} S.cm⁻¹) that emanates from the decrement in the volume fraction of conducting phase, restriction of chain mobility and the increased tortuosity as mentioned earlier; yet the quantitative contribution of individual factors could not be defined. In these conditions, ion hopping is the dominant mechanism, whereas the segmental motion is restricted for all SPEs.

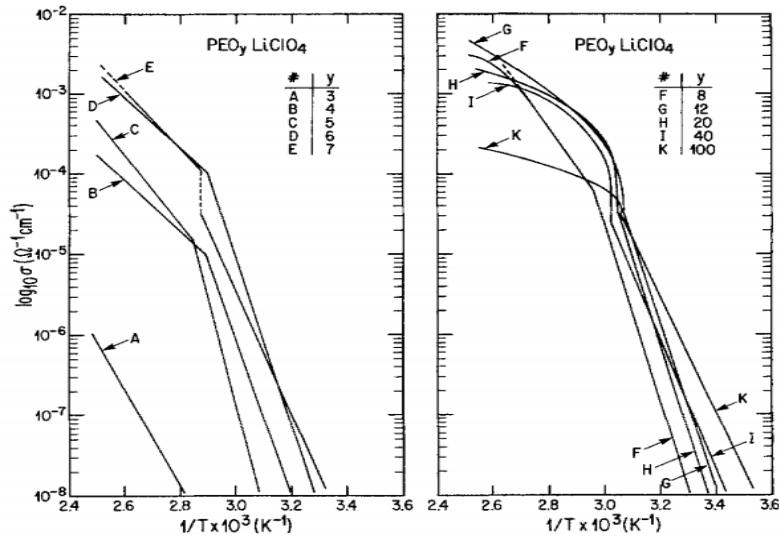


Figure 2.8: Temperature dependent ionic conductivity for solution cast $P(EO)_nLiClO_4$ electrolytes, reproduced from ref. [42].

2.2.5 Approaches to improve ionic conductivity in SPEs

2.2.5.1 Composite SPEs

The transport properties, the resistance to crystallization and the stability of the electrode-electrolyte interfaces of the SPE can be improved by the incorporation of certain inorganic fillers with Lewis acid characteristics like TiO_2 , SiO_2 , or Al_2O_3 [12, 15, 16, 52-71]. The maximal conductivities of SPEs after addition of nanoparticles were found to be around 10^{-4} - 10^{-5} S.cm⁻¹ at 20°C [72-76]. During their early investigations, Scrosati and co-workers found that the addition of ceramic particles of γ - $LiAlO_2$ smaller than 4 μm into a $P(EO)_8LiClO_4$ SPE improved

the mechanical property, interfacial stability and ionic conductivity [63]. However, the mechanism of this enhancement was not well understood. In the subsequent studies, the ion conduction mechanism in these nanocomposite SPEs have been systematically investigated [15, 16, 53, 55, 62, 64].

The ion conduction in $P(EO)_8LiClO_4$ nanocomposite SPEs was studied by Scrosati's group [16]. **Fig. 2.9** compares the temperature dependent conductivity curves of ceramic-free SPE with those for nanocomposite SPEs containing 10 wt.% TiO_2 (13 nm) and Al_2O_3 (5.8 nm) nanoparticles, respectively. The as-cast composite SPE containing Al_2O_3 nanoparticles exhibits similar curve as the ceramic-free SPE. However, subsequent cooling curves show completely different behaviour. The conductivity "knee" around $60^\circ C$ that is commonly observed for neat PEO SPEs disappeared for both TiO_2 and Al_2O_3 nanocomposite SPEs. The room temperature conductivities of the nanocomposite SPEs were over 2 orders of magnitude higher than that of ceramic-free SPE. The mechanism of this enhancement was explained as the Lewis acid interactions between the surface of the nanoparticles, the anions and the ether oxygen on the PEO chains. The ceramic nanoparticles with Lewis acid characteristics are competing with lithium cations to form complexes with PEO segments and anions, which act as crosslinking centers to inhibit polymer re-crystallization.

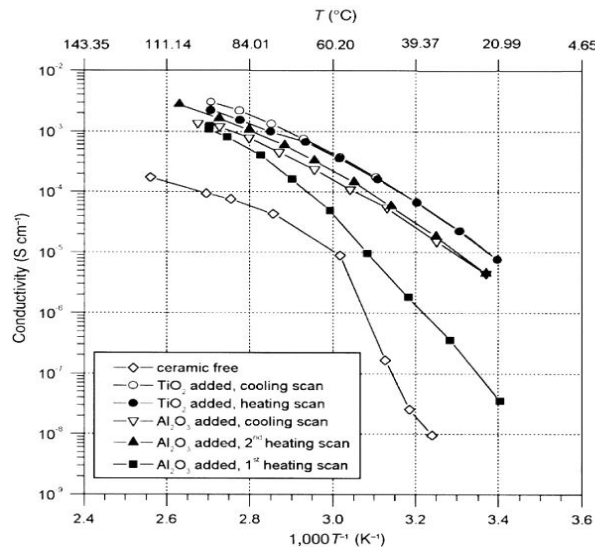


Figure 2.9: Temperature dependent ionic conductivity of PEO- $LiClO_4$ ceramic-free and nanocomposite SPEs, adopted from ref. [16].

This evidence likely suggests that the specific Lewis acid-base interactions between the ceramic surface groups, lithium salt and the polymer segments facilitate the ion dissociation and possibly create preferential conducting pathways at the boundaries of the ceramic particles to promote Li^+ transport.

The type of functional groups on the surface of the ceramic particles plays a critical role in the ion conduction in nanocomposite SPEs. In a study conducted by Croce *et al.*, Al_2O_3 nanoparticles with different surface characteristics: acidic, neutral and basic had been incorporated into a $\text{P}(\text{EO})_{20}\text{LiSO}_3\text{CF}_3$ SPE [64]. The acidic/neutral Al_2O_3 based SPEs showed higher degree of conductivity enhancement over basic Al_2O_3 SPE. The author proposed the mechanism to be the specific Lewis-acid interactions as illustrated in **Fig. 2.10**. Acidic/neutral Al_2O_3 formed hydrogen bonding with the anions as well as the ether oxygen on the PEO chain, promoting the salt dissociation and weakening the cation-polymer coordination, whereas the basic Al_2O_3 could only interact with Li^+ . However, the study conducted by Jayathilaka *et al.* on a $\text{P}(\text{EO})_9\text{LiTFSI}$ SPE system suggested that there was no direct interaction between the filler particles and the polymer chains. The Al_2O_3 particles interacted with both cations and anions, providing additional sites for ion hopping. The degree of conductivity improvement by the nanoparticles followed the order: acidic > basic > neutral > weakly acidic > filler free [77]. Another study on low M_w PEG $\text{LiClO}_4\text{-Al}_2\text{O}_3$ system showed that the neutral fillers produced a higher conductivity as compared with acidic and basic fillers [54]. There is no clear trend regarding the role of surface groups and it seems the specific interactions also depend on the type of anions and the polymer matrix being used.

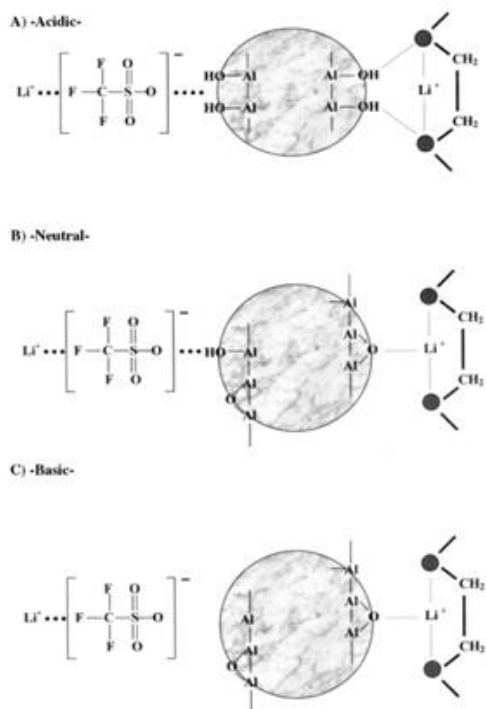


Figure 2.10: Illustration of the surface interaction between Al_2O_3 nanoparticles with different surface characteristics and the PEO- LiSO_3CF_3 complex. Adapted from ref. [64].

Depending on the type of anions, the nature of the nanoparticles, the structure and M_w of the polymer, different ion conduction mechanisms may be proposed. A better understanding of the fundamentals of ion transport in these multiphase SPE systems still needs to be developed.

2.2.5.2 Blend polymers composite SPEs

Blending of PEO-electrolytes with other polymers has been adopted as an easy and useful technique for suppressing crystallinity and enhancing the room temperature conductivity. The best room temperature conductivities were found to be of the order of 10^{-4} - 10^{-5} $\text{S}\cdot\text{cm}^{-1}$ [78-80]. The polymer blends often exhibit properties that are superior to the properties of each individual component polymer [81-85]. The simplicity of preparation and the ease of control of physical properties by compositional change are the main advantages of the blend systems [86-88]. However, the miscibility of homopolymers on the molecular scale affects the superior properties. The major advantages of blend polymer electrolytes are improved ionic conductivity, interfacial stability, mechanical stability and good thermal stability compared to other electrolyte systems.

Over the past few years many blend electrolytes have been reported based on poly(ethylene oxide) (PEO)-polyacrylonitrile (PAN) [89-92], poly(vinylidene fluoride-co-hexafluoropropylene) (P(VdF-HFP))-poly (vinyl acetate) (PVAc) [93], poly(vinyl chloride) (PVC)-poly(methyl methacrylate) (PMMA) [94-96], PVAc-PMMA [97], PVC-PAN [78], PEO-PVC [98, 99], PEO-P(VdF-HFP) [100], and so on.

PEO can act as a proton acceptor and form miscible blends with a variety of proton-donating polymers, due to its partial negative charge on the oxygen atoms [101]. On the other hand, PMMA and PVAc have partial positive charge on their carbonyl carbon atoms. A number of researchers have offered experimental evidence to indicate that the blends of PEO with PMMA and PVAc are miscible [102-109]. Russel and co-workers measured the interaction parameters of PEO-PMMA by applying neutron-scattering method and found very small negative values that suggested that the possible interaction between two components should be very weak [110]. Ramana Rao *et al.* also confirmed the existence of a very weak specific interaction between PEO and PMMA using vibrational spectroscopy [111]. They pointed out that the attractive forces between the negatively charged oxygen atoms of PEO and positively charged carbonyl carbon atoms of PMMA are weakened by the repulsive forces offered by the negatively charged oxygen atoms of PMMA. Due to the molecular structure of PVAc which has more or less similar carbonyl groups to PMMA, a similar situation should appear between PEO and PVAc. Xue Chen *et al.* obtained a negative value of the heat of mixing for PEO-PMMA (50/50, wt.%) and PEO-PVAc (20/80, 39/61, 66/34, wt.%) blends and confirmed the miscibility of the two blending systems [101].

2.3 Summary

In this chapter, a brief introduction of the history of polymer electrolyte was first described; the basics of ion conduction in PEO based SPEs were discussed and the state of the art development of the current SPE systems was reviewed in details. Depending on the nature of the SPE system, the ion transport properties could be quite different (for example, nanocomposite SPEs compared with blend polymers SPEs). Although the ion conduction in polymers is strongly associated with chain dynamics, it is not an essential requisite for the fast ion transport. Further understanding of the fundamentals of ion conduction mechanism in the current SPE systems is highly desirable.

2.4 References

1. Fenton, D. E.; Parker, J. M.; Wright, P. V., *Polymer*, **1973**, *14*, 11, 589.
2. Wright, P. V., *British Polymer Journal*, **1975**, *7*, 5, 319-327.
3. Armand, M. B., Chabagno, J. M., and Duclot, M. J., *Fast ion transport in solids: electrodes, and electrolytes : proceedings of the International Conference on Fast Ion Transport in Solids, Electrodes, and Electrolytes*. North Holland, New York, **1979**; p 131–136.
4. Lee, C. C.; Wright, P. V., *Polymer*, **1982**, *23*, 5, 681-689.
5. Payne, D. R.; Wright, P. V., *Polymer*, **1982**, *23*, 5, 690-693.
6. Berthier, C.; Gorecki, W.; Minier, M.; Armand, M. B.; Chabagno, J. M.; Rigaud, P., *Solid State Ionics*, **1983**, *11*, 1, 91-95.
7. Ratner, M. A.; Shriver, D. F., *Chemical Reviews*, **1988**, *88*, 1, 109-124.
8. Murata, K.; Izuchi, S.; Yoshihisa, Y., *Electrochimica Acta*, **2000**, *45*, 8–9, 1501-1508.
9. Meyer, W. H., *Advanced Materials*, **1998**, *10*, 6, 439-448.
10. Takeoka, S.; Ohno, H.; Tsuchida, E., *Polymers for Advanced Technologies*, **1993**, *4*, 2-3, 53-73.
11. Quartarone, E.; Mustarelli, P., *Chemical Society reviews*, **2011**, *40*, 5, 2525-40.
12. Quartarone, E.; Mustarelli, P.; Magistris, A., *Solid State Ionics*, **1998**, *110*, 1–2, 1-14.
13. MacGlashan, G. S.; Andreev, Y. G.; Bruce, P. G., *Nature*, **1999**, *398*, 6730, 792-794.
14. Angell, C. A.; Liu, C.; Sanchez, E., *Nature*, **1993**, *362*, 6416, 137-139.
15. Croce, F.; Persi, L.; Ronci, F.; Scrosati, B., *Solid State Ionics*, **2000**, *135*, 1–4, 47-52.
16. Croce, F.; Appetecchi, G. B.; Persi, L.; Scrosati, B., *Nature*, **1998**, *394*, 6692, 456-458.
17. Berman, M. B.; Greenbaum, S. G., *Membranes*, **2015**, *5*, 4, 915-923.
18. Gadjourova, Z.; Andreev, Y. G.; Tunstall, D. P.; Bruce, P. G., *Nature*, **2001**, *412*, 6846, 520-3.
19. Stoeva, Z.; Martin-Litas, I.; Staunton, E.; Andreev, Y. G.; Bruce, P. G., *Journal of the American Chemical Society*, **2003**, *125*, 15, 4619-26.
20. Christie, A. M.; Lilley, S. J.; Staunton, E.; Andreev, Y. G.; Bruce, P. G., *Nature*, **2005**, *433*, 7021, 50-3.
21. Cheng, S.; Smith, D. M.; Pan, Q.; Wang, S.; Li, C. Y., *RSC Advances*, **2015**, *5*, 60, 48793-48810.
22. Anonymous, *Polymer yearbook*. harwood academic publishers.
23. Panayiotou, C.; Vera, J. H., *Polym J*, **1984**, *16*, 2, 89-102.
24. Armand, M., *Solid State Ionics*, **1994**, *69*, 3, 309-319.
25. Armand, M. B., *Annual Review of Materials Science*, **1986**, *16*, 1, 245-261.
26. Armand, M., *Solid State Ionics*, **1983**, *9*, 745-754.
27. Vögtle, F. W., E., *Crown ethers and analogs*, Wiley: New York, 1989.
28. Pedersen, C. J., *Angewandte Chemie International Edition in English*, **1988**, *27*, 8, 1021-1027.
29. Olagoke Olabisi, K. A., *Handbook of Thermoplastics*. 1997.
30. Christopoulou, K.; Andrikopoulos, K. S.; Fotiadou, S.; Bollas, S.; Karageorgaki, C.; Christofilos, D.; Voyiatzis, G. A.; Anastasiadis, S. H., *Macromolecules*, **2011**, *44*, 24, 9710-9722.
31. Kumar, B.; Scanlon, L. G., *Journal of Electroceramics*, **2000**, *5*, 2, 127-139.
32. Armand, M., *Advanced Materials*, **1990**, *2*, 6-7, 278-286.
33. Baril, D.; Michot, C.; Armand, M., *Solid State Ionics*, **1997**, *94*, 1, 35-47.

34. Spencer, N. D., *Tailoring Surfaces: Modifying Surface Composition and Structure for Applications in Tribology, Biology and Catalysis (Iisc Centenary Lecture)*. first ed.; World Scientific Publishing Company.
35. Reale, P.; Panero, S.; Scrosati, B., *Journal of The Electrochemical Society*, **2005**, *152*, 10, A1949-A1954.
36. Sakellariou, P.; Abraham, M. H.; Whiting, G. S., *Colloid and Polymer Science*, **1994**, *272*, 7, 872-875.
37. Shodai, T.; Owens, B. B.; Ohtsuka, H.; Yamaki, J. i., *Journal of The Electrochemical Society*, **1994**, *141*, 11, 2978-2981.
38. Ue, M., *Journal of The Electrochemical Society*, **1994**, *141*, 12, 3336-3342.
39. Marzantowicz, M.; Dygas, J. R.; Krok, F.; Nowiński, J. L.; Tomaszewska, A.; Florjańczyk, Z.; Zygadło-Monikowska, E., *Journal of Power Sources*, **2006**, *159*, 1, 420-430.
40. Marzantowicz, M.; Dygas, J. R.; Krok, F.; Łasińska, A.; Florjańczyk, Z.; Zygadło-Monikowska, E.; Affek, A., *Electrochimica Acta*, **2005**, *50*, 19, 3969-3977.
41. Marzantowicz, M.; Dygas, J. R.; Krok, F.; Florjańczyk, Z.; Zygadło-Monikowska, E., *Electrochimica Acta*, **2007**, *53*, 4, 1518-1526.
42. Robitaille, C. D.; Fauteux, D., *Journal of The Electrochemical Society*, **1986**, *133*, 2, 315-325.
43. Neat, R.; Glasse, M.; Linford, R.; Hooper, A., *Solid State Ionics*, **1986**, *18*, 1088-1092.
44. Marzantowicz, M.; Krok, F.; Dygas, J. R.; Florjańczyk, Z.; Zygadło-Monikowska, E., *Solid State Ionics*, **2008**, *179*, 27-32, 1670-1678.
45. Lascaud, S.; Perrier, M.; Vallee, A.; Besner, S.; Prud'homme, J.; Armand, M., *Macromolecules*, **1994**, *27*, 25, 7469-7477.
46. Choi, B.-K., *Solid State Ionics*, **2004**, *168*, 1-2, 123-129.
47. Marzantowicz, M.; Dygas, J. R.; Krok, F.; Łasińska, A.; Florjańczyk, Z.; Zygadło-Monikowska, E., *Electrochimica Acta*, **2006**, *51*, 8-9, 1713-1727.
48. Zhang, Y.; Li, J.; Huo, H.; Jiang, S., *Journal of Applied Polymer Science*, **2012**, *123*, 4, 1935-1943.
49. Dygas, J. R.; Misztal-Faraj, B.; Florjańczyk, Z.; Krok, F.; Marzantowicz, M.; Zygadło-Monikowska, E., *Solid State Ionics*, **2003**, *157*, 1-4, 249-256.
50. Minier, M.; Berthier, C.; Gorecki, W., *Journal de Physique*, **1984**, *45*, 4, 739-744.
51. Cheng, S.; Smith, D. M.; Li, C. Y., *Macromolecules*, **2014**, *47*, 12, 3978-3986.
52. Walls, H. J.; Zhou, J.; Yerian, J. A.; Fedkiw, P. S.; Khan, S. A.; Stowe, M. K.; Baker, G. L., *Journal of Power Sources*, **2000**, *89*, 2, 156-162.
53. Chung, S. H.; Wang, Y.; Persi, L.; Croce, F.; Greenbaum, S. G.; Scrosati, B.; Plichta, E., *Journal of Power Sources*, **2001**, 97-98, 644-648.
54. Marcinek, M.; Bac, A.; Lipka, P.; Zalewska, A.; Żukowska, G.; Borkowska, R.; Wiczorek, W., *The Journal of Physical Chemistry B*, **2000**, *104*, 47, 11088-11093.
55. Croce, F.; Curini, R.; Martinelli, A.; Persi, L.; Ronci, F.; Scrosati, B.; Caminiti, R., *The Journal of Physical Chemistry B*, **1999**, *103*, 48, 10632-10638.
56. Capuano, F.; Croce, F.; Scrosati, B., *Journal of The Electrochemical Society*, **1991**, *138*, 7, 1918-1922.
57. Krawiec, W.; Scanlon, L. G.; Fellner, J. P.; Vaia, R. A.; Vasudevan, S.; Giannelis, E. P., *Journal of Power Sources*, **1995**, *54*, 2, 310-315.
58. Wiczorek, W.; Lipka, P.; Żukowska, G.; Wyciślik, H., *The Journal of Physical Chemistry B*, **1998**, *102*, 36, 6968-6974.

59. Capiglia, C.; Mustarelli, P.; Quartarone, E.; Tomasi, C.; Magistris, A., *Solid State Ionics*, **1999**, *118*, 1–2, 73-79.
60. Lim, Y.-J.; An, Y.-H.; Jo, N.-J., *Nanoscale Research Letters*, **2012**, *7*, 1, 19-19.
61. Kumar, B.; Scanlon, L. G., *Solid State Ionics*, **1999**, *124*, 3–4, 239-254.
62. Appetecchi, G. B.; Croce, F.; Persi, L.; Ronci, F.; Scrosati, B., *Electrochimica Acta*, **2000**, *45*, 8–9, 1481-1490.
63. Scrosati, B.; Croce, F.; Persi, L., *Journal of The Electrochemical Society*, **2000**, *147*, 5, 1718-1721.
64. Croce, F.; Persi, L.; Scrosati, B.; Serraino-Fiory, F.; Plichta, E.; Hendrickson, M. A., *Electrochimica Acta*, **2001**, *46*, 16, 2457-2461.
65. Wiczorek, W.; Florjanczyk, Z.; Stevens, J. R., *Electrochimica Acta*, **1995**, *40*, 13, 2251-2258.
66. Siekierski, M.; Wiczorek, W.; Przyłuski, J., *Electrochimica Acta*, **1998**, *43*, 10–11, 1339-1342.
67. Kim, Y. W.; Lee, W.; Choi, B. K., *Electrochimica Acta*, **2000**, *45*, 8–9, 1473-1477.
68. Yamamoto, O.; Ogumi, Z.; Morita, M.; Choi, B.-K.; Kim, Y.-W.; Shin, K.-H., *Journal of Power Sources*, **1997**, *68*, 2, 357-360.
69. Best, A. S.; Ferry, A.; MacFarlane, D. R.; Forsyth, M., *Solid State Ionics*, **1999**, *126*, 3–4, 269-276.
70. Polu, A. R.; Rhee, H.-W., *Journal of Industrial and Engineering Chemistry*, **2016**, *37*, 347-353.
71. Liu, L.; Wang, Z.; Zhao, Z.; Zhao, Y.; Li, F.; Yang, L., *Journal of Solid State Electrochemistry*, **2016**, *20*, 3, 699-712.
72. Oleg, B.; Grant, D. S.; Rajdip, B.; Paul, R.; Larry, A. C., *Modelling and Simulation in Materials Science and Engineering*, **2004**, *12*, 3, S73.
73. Pan, C.-y.; Feng, Q.; Wang, L.-j.; Zhang, Q.; Chao, M., *Journal of Central South University of Technology*, **2007**, *14*, 3, 348-352.
74. Singh, P. K.; Bhattacharya, B.; Nagarale, R. K., *Journal of Applied Polymer Science*, **2010**, *118*, 5, 2976-2980.
75. Fullerton-Shirey, S. K.; Maranas, J. K., *The Journal of Physical Chemistry C*, **2010**, *114*, 20, 9196-9206.
76. Ni'mah, Y. L.; Cheng, M.-Y.; Cheng, J. H.; Rick, J.; Hwang, B.-J., *Journal of Power Sources*, **2015**, *278*, 375-381.
77. Jayathilaka, P. A. R. D.; Dissanayake, M. A. K. L.; Albinsson, I.; Mellander, B. E., *Electrochimica Acta*, **2002**, *47*, 20, 3257-3268.
78. Subbu, C.; Rajendran, S.; Kesavan, K.; Premila, R., *Ionics*, **2016**, *22*, 2, 229-240.
79. Xiao, Q.; Wang, X.; Li, W.; Li, Z.; Zhang, T.; Zhang, H., *Journal of Membrane Science*, **2009**, *334*, 1–2, 117-122.
80. Xi, J.; Qiu, X.; Li, J.; Tang, X.; Zhu, W.; Chen, L., *Journal of Power Sources*, **2006**, *157*, 1, 501-506.
81. Al-Ramadin, Y., *Optical Materials*, **2000**, *14*, 4, 287-290.
82. Fontanella, J. J.; Wintersgill, M. C.; Calame, J. P.; Andeen, C. G., *Solid State Ionics*, **1983**, *8*, 4, 333-339.
83. Reddeppa, N.; Reddy, T. J. R.; Achari, V. B. S.; Rao, V. V. R. N.; Sharma, A. K., *Ionics*, **2009**, *15*, 2, 255-259.
84. Płocharski, J.; Wiczorek, W.; Przyłuski, J.; Such, K., *Applied Physics A*, **1989**, *49*, 1, 55-60.

85. Whang, W.-T.; Yang, L.-H.; Fan, Y.-W., *Journal of Applied Polymer Science*, **1994**, *54*, 7, 923-933.
86. Urbach, F., *Physical Review*, **1953**, *92*, 5, 1324-1324.
87. Wu, W. B.; Chiu, W. Y.; Liao, W. B., *Journal of Applied Polymer Science*, **1997**, *64*, 3, 411-421.
88. Anonymous, *Polymer Blends Academic Press*,: New York, **1978**.
89. Munichandraiah, N.; Sivasankar, G.; Scanlon, L. G.; Marsh, R. A., *Journal of Applied Polymer Science*, **1997**, *65*, 11, 2191-2199.
90. Chun-Guey, W.; Chiung-Hui, W.; Ming-I, L.; Huey-Jan, C., *Journal of Applied Polymer Science*, **2006**, *99*, 4, 1530-1540.
91. Rajendran, S.; Mahalingam, T.; Kannan, R., *Solid State Ionics*, **2000**, *130*, 1–2, 143-148.
92. Yang, H.-Y.; Wu, G.; Chen, H.; Yuan, F.; Wang, M.; Fu, R.-J., *Journal of Applied Polymer Science*, **2006**, *101*, 1, 461-464.
93. Ulaganathan, M.; Rajendran, S., *Ionics*, **2010**, *16*, 6, 515-521.
94. Ramesh, S.; Leen, K. H.; Kumutha, K.; Arof, A. K., *Spectrochimica Acta Part A: Molecular and Biomolecular Spectroscopy*, **2007**, *66*, 4–5, 1237-1242.
95. Stephan, A. M.; Kumar, T. P.; Renganathan, N. G.; Pitchumani, S.; Thirunakaran, R.; Muniyandi, N., *Journal of Power Sources*, **2000**, *89*, 1, 80-87.
96. Choi, N.-S.; Park, J.-K., *Electrochimica Acta*, **2001**, *46*, 10–11, 1453-1459.
97. Baskaran, R.; Selvasekarapandian, S.; Kuwata, N.; Kawamura, J.; Hattori, T., *Solid State Ionics*, **2006**, *177*, 26–32, 2679-2682.
98. Ramesh, S.; Winie, T.; Arof, A. K., *European Polymer Journal*, **2007**, *43*, 5, 1963-1968.
99. Ramesh, S.; Yahaya, A. H.; Arof, A. K., *Solid State Ionics*, **2002**, *148*, 3–4, 483-486.
100. Fan, L.; Dang, Z.; Nan, C.-W.; Li, M., *Electrochimica Acta*, **2002**, *48*, 2, 205-209.
101. Chen, X.; Yin, J.; Alfonso, G. C.; Pedemonte, E.; Turturro, A.; Gattiglia, E., *Polymer*, **1998**, *39*, 20, 4929-4935.
102. Rajendran, S.; Kesavan, K.; Nithya, R.; Ulaganathan, M., *Current Applied Physics*, **2012**, *12*, 3, 789-793.
103. Ulaganathan, M.; Pethaiah, S. S.; Rajendran, S., *Materials Chemistry and Physics*, **2011**, *129*, 1–2, 471-476.
104. Zhou, S.; Kim, D., *Polymers for Advanced Technologies*, **2011**, *22*, 12, 2130-2135.
105. Marcos, J. I.; Orlandi, E.; Zerbi, G., *Polymer*, **1990**, *31*, 10, 1899-1903.
106. Martuscelli, E.; Pracella, M.; Wang, P. Y., *Polymer*, **1984**, *25*, 8, 1097-1106.
107. Liberman, S. A.; Gomes, A. D. S.; Macchi, E. M., *Journal of Polymer Science: Polymer Chemistry Edition*, **1984**, *22*, 11, 2809-2815.
108. Muñoz, E.; Calahorra, E.; Cortazar, M.; Santamaría, A., *Polymer Bulletin*, **1982**, *7*, 5, 295-301.
109. Chen, X.; Hu, H.; Yin, J.; Zheng, C., *Journal of Applied Polymer Science*, **1995**, *56*, 2, 247-252.
110. Ito, H.; Russell, T. P.; Wignall, G. D., *Macromolecules*, **1987**, *20*, 9, 2213-2220.
111. Rao, G. R.; Castiglioni, C.; Gussoni, M.; Zerbi, G.; Martuscelli, E., *Polymer*, **1985**, *26*, 6, 811-820.

Chapter 3

3 MATERIALS AND METHODS

3.1 Materials

Aluminum foil (alloy 1100, 99%, half-hard, 0.3 mm thickness) and copper foil (99.9%, half-hard, 0.3 mm thickness) were purchased from Goodfellow and cut into discs of 14 mm diameter before any further preparation. Lithium iron phosphate (LiFePO_4) nanoparticles (97%, <5 μm dia.), lithium hexafluorophosphate (LiPF_6 , 99.99%, battery grade), polyvinylidene fluoride (PVdF, avg. M_w 275,000), polyethylene oxide (PEO, avg. M_w 4 million), and polyvinyl acetate (PVAc, avg. M_w 140,000) were obtained from Aldrich. "Super P" conductive carbon black (99%) was obtained from Alfa Aesar. Anatase titanium dioxide (TiO_2) nanoparticles (99%, 15 nm dia.) were obtained from "Nanostructured and Amorphous Materials". Propylene carbonate (PC, 99.7%, anhydrous) and 1-methyl-2-pyrrolidinone (NMP, 99.5%) were obtained from Aldrich. Acetonitrile (ACN), potassium hydroxide (KOH), hydrochloric acid (HCl) and ethanol were obtained from Caledon. Ultra-pure argon and nitrogen gases were obtained from Praxair.

All materials were used as received without further purification except LiFePO_4 , PEO and TiO_2 which were first dried overnight under vacuum at 150°C, 50°C, and 120°C respectively.

3.2 Apparatus

The name, model and manufacturer of apparatus used in the experiments are listed in **Table 3.1**.

Table 3.1: Apparatus used in experiments.

Name	Model	Manufacturer
Magnetic Stirrer	Isotemp™ Basic	Fisher Scientific™
Analytical Balance	BP 61	Sartorius
Ultrasonic Bath	100004	Sper Scientific Direct
Oven	DX 400	Yamato
Argon glovebox	PW personal workstation glovebox	LC Technology Solutions Inc.
Spin coater	WS-400B-6NPP/LITE	Laurell
Potentiostat/Galvanostat	Model 263A	Princeton Applied Research
Scanning Electron Microscope	LEO 1540 XB	Zeiss
Thermogravimetric Analysis	Q 600	TA Instruments
Differential Scanning Calorimetry	Q 10	TA Instruments

3.3 Aluminum and Copper Substrate Preparation

Electrodes were first polished by hand with coarse (1200 grit) sandpaper and with fine (4000 grit) sandpaper. Aluminum electrodes were sonicated in detergent + milli-Q water, etched in 1 M potassium hydroxide solution and sonicated in ethanol for 15 minutes each. The substrates were dried using argon gas and placed under vacuum in a desiccator before further use. A similar procedure was followed for copper electrodes except for the etching step which was replaced by pickling with 1 M hydrochloric acid for 15 minutes.

3.4 Cathode Preparation

For anode samples tested in a two-electrode battery coin cell, a complementary cathode material was prepared outside the glove box under ambient conditions based on literature procedure [1]:

6 wt.% polyvinylidene fluoride (PVdF) binder was dissolved in 1-methyl-2-pyrrolidinone (NMP). 85 wt.% active material (LiFePO_4) and 5 wt.% "super P" conductive carbon black were ground and mixed together in a mortar and pestle, followed by mixing in a vortex apparatus for 10 minutes. The dissolved NMP-binder mixture was added to the ground LiFePO_4 -C mixture,

such that the binder constituted 10 wt.% of the total weight of the final mixture. The above mixture was vortexed at maximum rpm for about 30 minutes. If needed, more NMP was added in order to obtain a slurry with the required consistency. The final slurry was magnetically stirred at 300 rpm for 24 hours. The following day this slurry was spin coated on the polished and etched copper substrate at 300 rpm under N_2 gas. At this rotation speed the slurry uniformly spreads on the copper disc. The resulting cathode was dried under vacuum in a desiccator at $90^\circ C$ overnight. The cathode was placed between two weighing papers to protect the coating and pressed under a load of ~5 ton using a hydraulic press. The cathodes were transferred into an argon-filled glove box (H_2O and $O_2 < 1$ ppm) and stored there before spin-coating of the prepared solid polymer electrolyte mixture.

3.5 Preparation and Spin-Coating of SPE

$LiPF_6$ were dissolved in acetonitrile, followed by the addition of high-molecular weight PEO; the relative amounts of PVAc were expressed as weight percent (15, 35, and 50 wt.%), and the amount of $LiPF_6$ was given as the O:Li based on the amount of ethylene oxide and vinyl acetate. The mixture was stirred for 24 hours to form a viscous slurry which was cast on a Teflon plate in an Ar purged glove box, and left undisturbed for a day until a thin film was achieved. The electrolyte films were further dried under vacuum at $50^\circ C$ for 24 hours to remove acetonitrile residue.

In the case of solid polymer electrolyte with TiO_2 , the relative amounts of TiO_2 nanoparticles (5, 10 and 15 wt.%) were ground in a mortar and pestle, and then added to the solution of acetonitrile and $LiPF_6$. The resulting slurry was then ultrasonically agitated for 30 min. This procedure was used both to avoid agglomeration of TiO_2 nanoparticles and to remove gas bubbles present in the solution which could significantly affect the spin coating process. Then, the slurry was stirred for an additional 2 hours at RT. PEO (or the blend of PEO and PVAc) was added to the mixture at a O:Li ratio of 12:1 and stirred at RT for 20 hours. The spincoating and drying procedure was the same as above.

3.6 Solid Polymer Electrolyte Properties and Electrochemical Characterization Summary

A variety of SPE samples were prepared and spincoated on aluminum anode and LiFePO₄ (LFP) cathode substrates and characterized electrochemically in a prototype solid-state two-electrode coin cell. The various solid polymer electrolyte compositions and their battery prototypes testing procedure are summarized in **Tables 3.2 to 3.4**.

Table 3.2: SPEs with different contents of PVAc and their battery prototypes testing procedure.

Sample Code	PEO	PEPV15	PEPV35	PEPV50
Substrate	LFP cathode - Al	LFP cathode - Al	LFP cathode - Al	LFP cathode - Al
Polyethylene oxide wt%	100	85	65	50
Poly(vinyl acetate) wt%	0	15	35	50
O:Li	12:1	12:1	12:1	12:1
Spincoating speed (rpm)	150	150	150	150
Cyc. @ $1.6 \cdot 10^{-5}$ A.cm ⁻² *	8	8	8	8
Cyc. @ $3.2 \cdot 10^{-5}$ A.cm ⁻²	8	8	8	8
Cyc. @ $6.5 \cdot 10^{-5}$ A.cm ⁻²	100	100	100	100
Cyc. @ $1.3 \cdot 10^{-4}$ A.cm ⁻²	100	-	100	-

* Cyc. @ $1.6 \cdot 10^{-5}$ A.cm⁻² means galvanic cycle at that current density

Table 3.3: SPEs with different contents of TiO₂ and their battery prototypes testing procedure.

Sample Code	PEO	PT5	PT10	PT15
Substrate	LFP cathode - Al	LFP cathode - Al	LFP cathode - Al	LFP cathode - Al
Polyethylene oxide wt%	100	100	100	100
TiO ₂ wt%	0	5	10	15
O:Li	12:1	12:1	12:1	12:1
Spincoating speed (rpm)	150	150	150	150
Cyc. @ $1.6 \cdot 10^{-5}$ A.cm ⁻²	8	8	8	8
Cyc. @ $3.2 \cdot 10^{-5}$ A.cm ⁻²	8	8	8	8
Cyc. @ $6.5 \cdot 10^{-5}$ A.cm ⁻²	100	100	100	100
Cyc. @ $1.6 \cdot 10^{-4}$ A.cm ⁻²	100	-	100	-

Table 3.4: SPEs with different contents of PVAc and TiO₂ and their battery prototypes testing procedure

Sample Code	PEO	PEPV35	PT10	PPT10
Substrate	LFP cathode - Al	LFP cathode - Al	LFP cathode - Al	LFP cathode - Al
Polyethylene oxide wt%	100	65	100	65
Polyvinyl acetate wt%	-	35	-	35
TiO ₂ wt%	-	-	10	10
O:Li	12:1	12:1	12:1	12:1
Spincoating speed (rpm)	150	150	150	150
Cyc. @ $1.6 \cdot 10^{-5}$ A.cm ⁻²	8	8	8	8
Cyc. @ $3.2 \cdot 10^{-5}$ A.cm ⁻²	8	8	8	8
Cyc. @ $6.5 \cdot 10^{-5}$ A.cm ⁻²	100	100	100	100
Cyc. @ $1.3 \cdot 10^{-4}$ A.cm ⁻²	100	100	100	100
Cyc. @ $3.2 \cdot 10^{-4}$ A.cm ⁻²	100	100	50	50
Cyc. @ $4.6 \cdot 10^{-4}$ A.cm ⁻²	-	-	50	50
Cyc. @ $5.9 \cdot 10^{-4}$ A.cm ⁻²	-	-	50	50
Cyc. @ $6.5 \cdot 10^{-4}$ A.cm ⁻²	-	-	100	100

3.7 Lithium-Ion Battery Coin Cell Assembly and Testing

The schematics of a two-electrode cell is shown in **Fig. 3.1**. The working electrode (WE), reference electrode (RE) and counter electrode (CE) as well as the cathode, electrolyte and anode are shown. In this cell the cathode is considered the working electrode (WE) and the anode is both the counter (CE) and reference electrodes (RE). The anode and cathode are separated by the solid polymer electrolyte (SPE) layer. The inner diameter of the cell opening was 14 mm and 10 mm in depth. Copper metal rod through the base serves as the current collector for the cathode, and a copper spring through the lid as the collector for the anode. The assembly and testing of the cell was performed inside an argon-filled glovebox according to the following procedure: first the Teflon cup with a copper metal rod through its base and the spring through its lid were cleaned. These components were rinsed with acetonitrile and dried at 90°C for approximately 3 hours. A polymer-coated cathode was placed face up inside the bottom of the Teflon cell and connected as the working electrode. To enhance the ion mobility and conductivity in the SPE layer via partial swelling of the polymer electrolyte, 1 μL of propylene carbonate was dispensed onto the polymer-coated cathode using a micropipette. Then, the polymer-coated aluminum anode was placed face down on top. The spring-loaded cap for the Teflon cell was, then, tightened to complete assembly. A wire welded to the copper spring was connected as both counter and reference electrodes. Finally, the cell was allowed to stabilize for 2 hours before commencing the galvanic cycling.

Cell testing was performed using a PAR 263A potentiostat/galvanostat controlled by Corrware software. To form enough porous nanostructure on the surface of bulk aluminum, firstly preconditioning of the battery prototype was performed at room temperature by applying low current densities of $1.6 \cdot 10^{-5}$ and $3.3 \cdot 10^{-5}$ $\text{A}\cdot\text{cm}^{-2}$ for 8 cycles at each current density. Right after preconditioning the galvanostatic charge-discharge cycles were conducted at higher current densities of $6.5 \cdot 10^{-5}$, $1.3 \cdot 10^{-4}$, and $3.2 \cdot 10^{-4}$ $\text{A}\cdot\text{cm}^{-2}$ for 100 cycles each. Charge and discharge steps were set at a maximum of 1000 s. Exposed sample diameters were 14 mm for both anode and cathode electrodes.

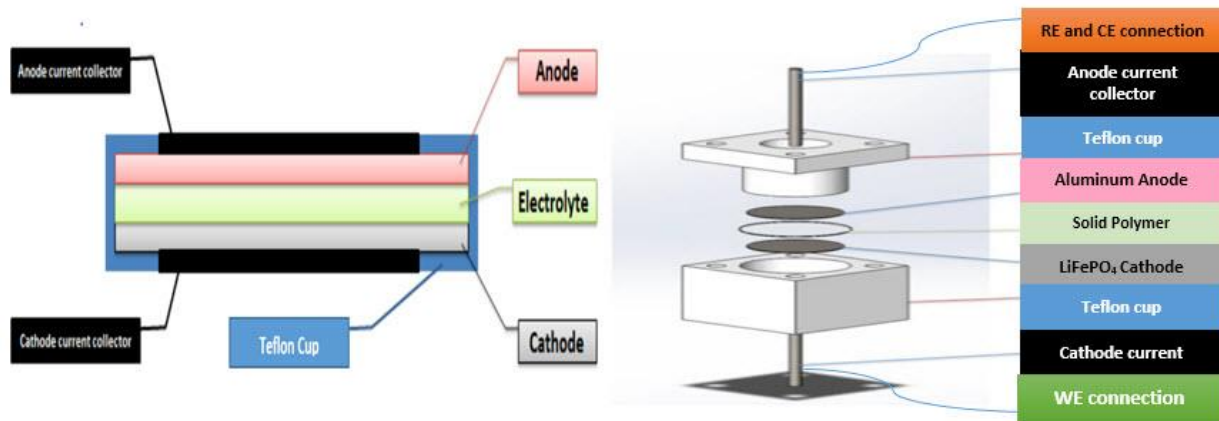


Figure 3.1: Schematic cross-section showing the structure of a coin cell lithium-ion battery with solid polymer electrolyte

3.8 Characterizations

3.8.1 Electrochemistry Techniques and Methodology used in Lithium-Ion Battery Research

3.8.1.1 Galvanic Cycling

Galvanic cycles are practically useful for simulating the real charge/discharge behavior of battery materials. The cycles involve a current being applied to a system while the potential is monitored. The current is applied until a particular limit of charge or potential is reached at which the current is stopped or the reverse current is applied. To illustrate the features of galvanic cycles for a battery with solid polymer electrolyte and their meaning, a battery with LiFePO_4 cathode, SPE and Al anode can be considered.

Shown in **Fig. 3.2** are the typical features of a galvanic cycle at a current density of $6.5 \cdot 10^{-5} \text{ A.cm}^{-2}$. The galvanic cycle shows the charging and discharging regions, the IR drop due to the electrolyte resistance, the coulombic efficiency and the discharging voltage.

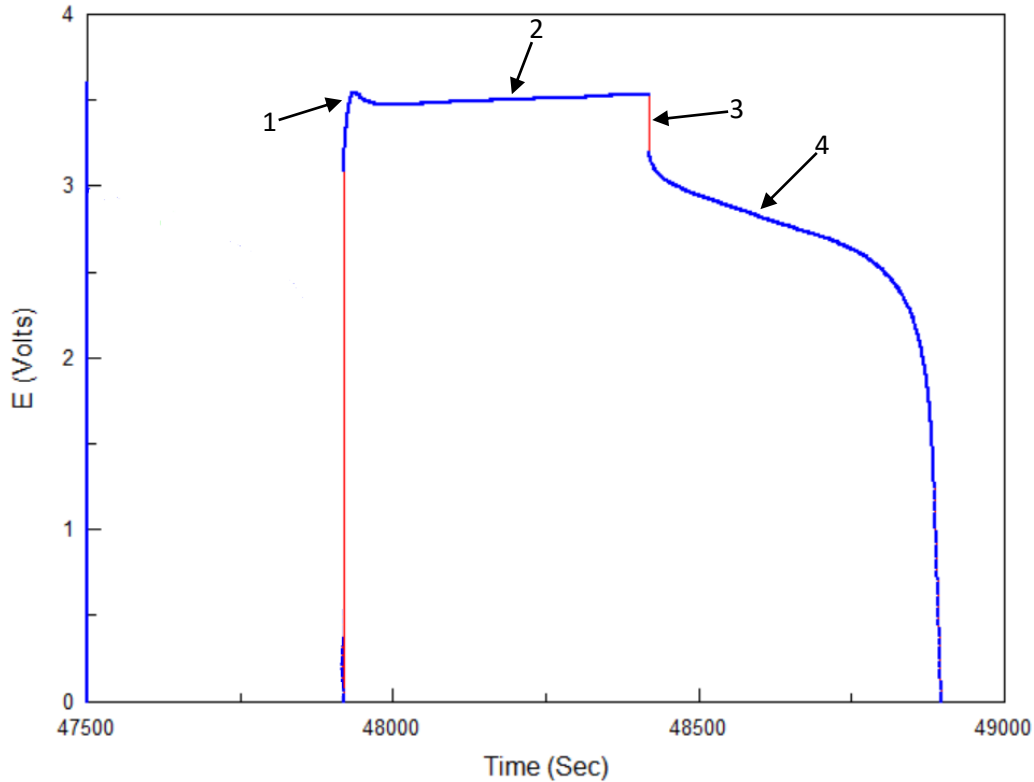


Figure 3.2: A battery galvanic cycle of a prototype with a solid polymer electrolyte, LiFePO_4 cathode and an Al anode at a current density of $6.5 \cdot 10^{-5} \text{ A.cm}^{-2}$.

Firstly, the current density that charges the prototype was applied. The corresponding portion of the galvanic cycle is referred to as the "charging region". At the beginning of each charging region a small overshoot of the potential was observed, which indicates the start of the charging process (1). This overshoot in potential was followed by a charging plateau (2). The charging portion typically continued until it was terminated by time since there is no limit in the amount of Al available for lithiation (bulk Al anodes were used) and the capacity of the cathode was intentionally made to exceed many times the charges used in the galvanic cycles. Then, the opposite current density was applied and the instantaneous potential drop observed is termed the "IR drop" (3). This drop is associated with all resistances that are in series with the complex impedances of the two electrodes and will mainly represent the resistance of the solid polymer electrolyte. The IR drop portion is followed by a long discharging plateau (4) involving delithiation of the anode and lithiation of the cathode.

Dividing the total discharging time by the total charging time produces the coulombic efficiency, or the ratio of the charges associated with the charging and discharging processes which is directly related to the reversibility of lithiation/delithiation. The discharging voltage is also a very important parameter that shows the performance of the battery. The higher the discharging voltage, the higher the battery energy and power density. The measured output voltage differs from the difference in thermodynamic potentials at the electrodes by IR drops and overvoltages associated with possible slow electrode kinetics and transport. Correction for the IR drop can be performed by adding half of the IR drop (part **(3)**) to the potential of the discharging plateau **4** because the current associated with part **(3)** changes from +I to -I and thus the change is equal to 2·I.

3.8.1.2 Determination of the IR drop from galvanic cycles

The Randles circuit is the simplest and most common cell model. It includes a bulk electrolyte resistance, a double layer capacitor and a polarization resistance. The Randles circuit can be used as a general model representing the various phenomena going on at the interface of the anode in a lithium ion battery. It describes the electrochemical process of charge transfer for one electrode in an electrolyte. **Fig. 3.3** shows the Randles circuit with the electrolyte resistance R_e , the charge transfer resistance R_{ct} , in parallel with the double layer capacitance C_{dl} . In more advanced models, the simple charge-transfer resistance can be replaced with a complex charge-transfer impedance Z_{ct} or even more complex circuits; however, the most important fact for us is that these circuit elements will always be in parallel with the double-layer capacitance of the electrode.

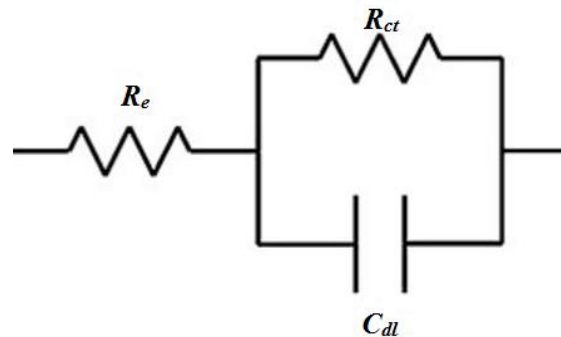


Figure 3.3: The typical Randles circuit.

In a Li-ion battery, the current flows between the anode: Al and cathode: LiFePO₄ through an ionically conducting electrolyte. Therefore, an appropriate equivalent circuit for the cell is shown in **Fig. 3.4** and includes the impedances of the anode and the cathode, with their corresponding double-layer capacitances, as well as the resistance of the electrolyte in series with the two electrodes.

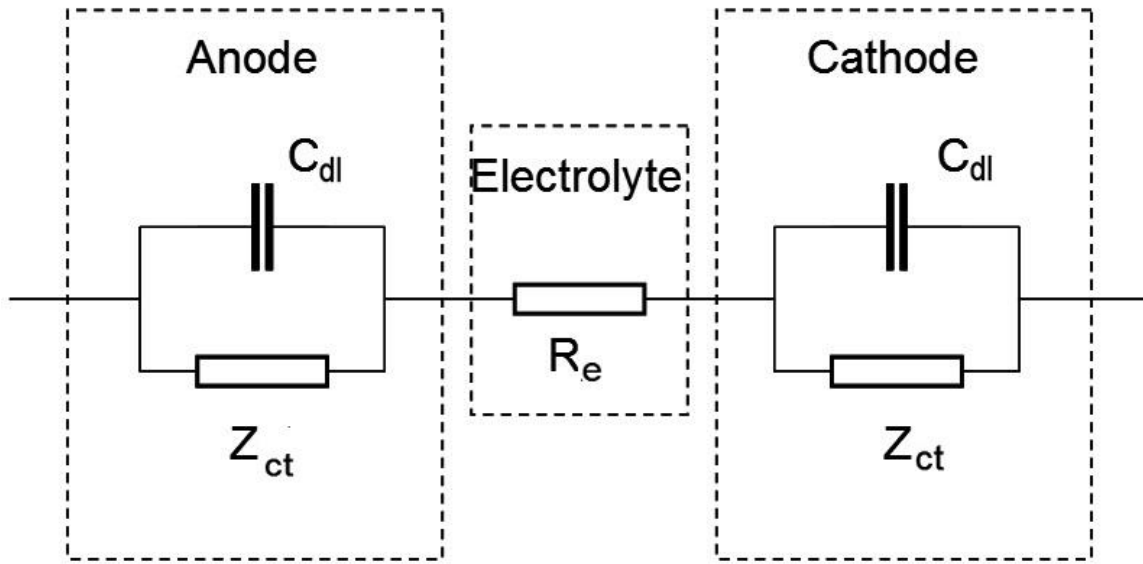


Figure 3.4: The equivalent circuit for battery prototypes.

When a current is flowing in an electrochemical cell, there is a voltage drop between the two electrodes. This voltage drop is caused by the electrolyte conductivity and the magnitude of the current.

Using Ohm's law, the voltage drop can be calculated to be equal to the product of the current (*I*) and the electrolyte resistance (*R_e*):

$$\Delta E_{ohmic} = I \cdot R_e \quad (1)$$

where ΔE_{ohmic} is the ohmic drop or IR drop. The IR drop is inversely proportional to the electrolyte conductivity. The lower the conductivity of the electrolyte, the higher the ohmic resistance and therefore the higher the IR drop [2].

The IR drop and thus the value of *R_e* can be determined using the current interrupt method. In this method, the current in the electrochemical cell is abruptly changed. However, since the

voltages at capacitances in the equivalent circuit of **Fig. 3.4** cannot change instantaneously, the electrode impedances Z_{ct} are short-circuited at the time of the current interrupt and the only change in the voltage across the cell is associated with the potential drop at the electrolyte resistance $I \cdot R_e$. In our galvanic cycles, the current changes from $+I$ to $-I$; hence; $\Delta I=2I$ and

$$R_e = \frac{\Delta E}{\Delta I} \quad (2)$$

Therefore, using this approach, we can determine the resistance of our solid polymer electrolytes from the potential jumps when the current direction is switched during galvanic cycles.

3.8.1.3 Analysis of the potential vs. time

The shape of the potential response can be rationalized by considering the concentration changes of the redox species as a function of time. If we consider the electron transfer reaction “ $Al + Li^+ + e^- \rightarrow LiAl$ ”, before applying the current, there is no $LiAl$ formed yet and the initial potential is determined by some other equilibria. Once the current density that charges the prototype has been applied, $LiAl$ is formed at the electrode surface, therefore Li^+ is reduced to $LiAl$. This sets up an equilibrium between Li^+ in the electrolyte and $LiAl$ at the electrode surface. The electrode potential will then be described by the Nernst equation for the $Al + Li^+ + e^- \rightarrow LiAl$ reaction (**Eq. 3**):

$$E = E^0 + \frac{RT}{nF} \ln \frac{[Li^+]}{[LiAl]} \quad (3)$$

Since the concentration of Li ions in the solution should stay constant, and the activity of a solid $LiAl$ phase is unity, the electrode potential should also stay constant once the equilibrium is established. Deviations from this behavior could be observed only if the equilibrium conditions at the electrode are violated (e.g., due to slow electrode kinetics). Generally speaking, even if there are some other concurrent processes, the electrode potential will still be determined by the electrochemical equilibrium with the highest exchange current density. Note that for Li^+ intercalation electrodes, the electrode potential will change with charging-discharging as a function of the changing activity of Li^+ in the intercalation compounds.

3.8.2 Morphological analysis

3.8.2.1 Scanning Electron Microscopy (SEM)

The scanning electron microscopy (SEM) has been the most widely used technique to characterize the morphology and topology of different samples especially on the nanoscale. It captures images of a sample by scanning it with a high-energy beam of electron. Different types of signals produced by an SEM include secondary electrons, back-scattered electrons (BSE), characteristic X-rays, and transmitted electrons.

After electrochemical measurements all samples were removed from the cell and immediately soaked in acetonitrile at RT overnight to remove solid polymer electrolyte. Then copper and aluminum discs were separated, rinsed with milliQ water and soaked in milliQ water at RT overnight to remove the left over solid polymer electrolyte completely. Samples were then stored in a desiccator under vacuum until surface analysis was performed.

The morphology of each anode sample was investigated by scanning electron microscopy (SEM). All images were collected at an electron column voltage of 1 kV, with different magnifications from 100 to 20000 if surface charging was not excessive.

Fig. 3.5 (a)-(d) are representative SEM images of the LiFePO_4 cathode and aluminum anode surface of the battery before and after cycling. It can be clearly seen that the structure of the LiFePO_4 cathode was not changed, whereas the porous nanostructure was formed on the surface of bulk aluminum during cycling the prototype at $6.5 \cdot 10^{-5} \text{ A}\cdot\text{cm}^{-2}$. This nanostructure represents the new LiAl phase formed during the electroformation process (**Chapter 1, Section 1.1.1.1**).

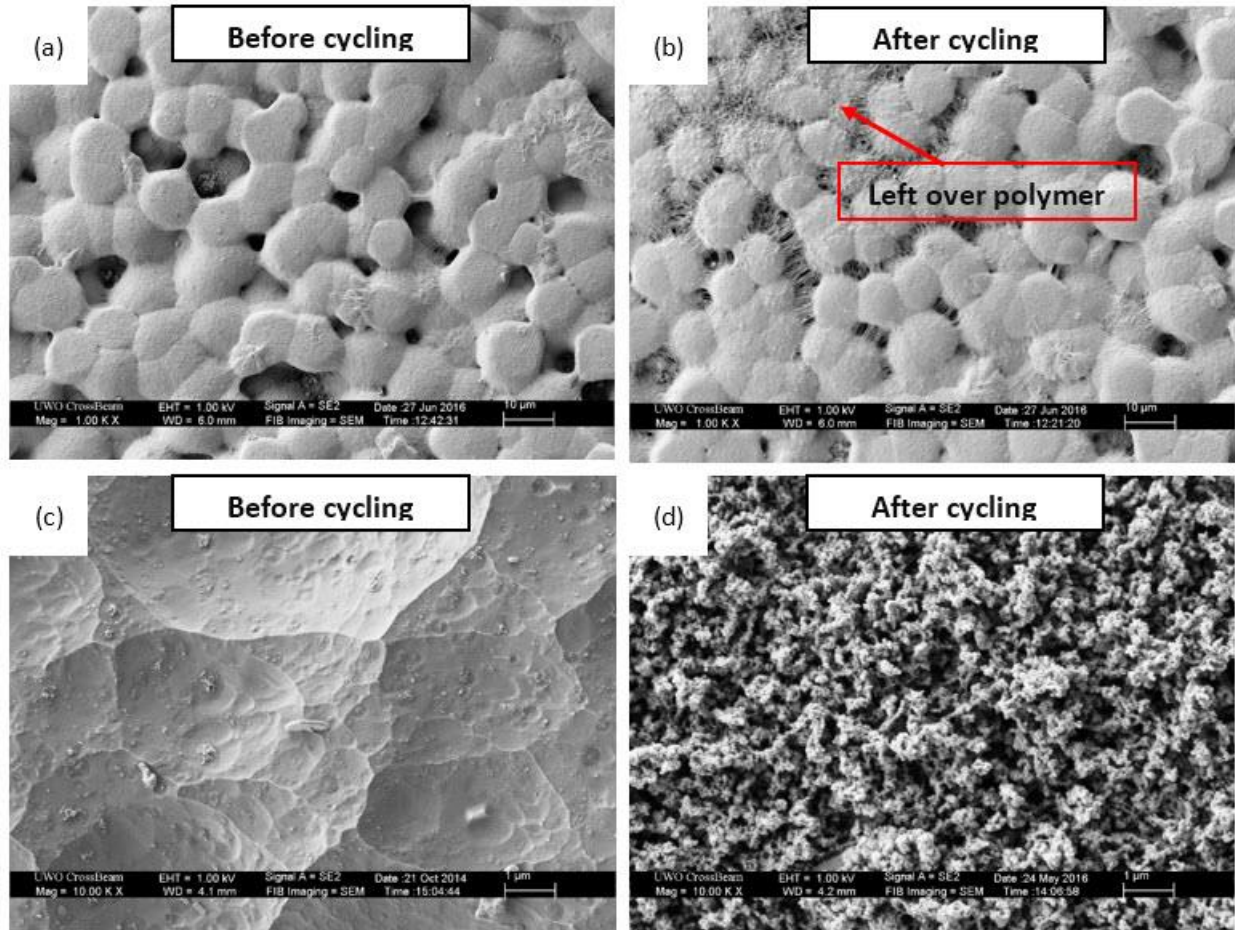


Figure 3.5: SEM image of battery cathode and anode before and after galvanic cycling at $6.5 \cdot 10^{-5} \text{ A.cm}^{-2}$, (a) LiFePO_4 -before (b) LiFePO_4 -after at 100X magnification (c) Al-before (d) Al-after at 10000X magnification.

3.8.3 Thermal analysis

Differential scanning calorimetry (DSC) and thermogravimetric analysis (TGA) are popular thermoanalytical techniques used to determine the glass transition temperatures and the thermal stability of polymer electrolytes.

The DSC is used to detect the polymer electrolyte's phase transitions by monitoring the difference in power or heat supplied to maintain two sample containers at the same temperature. One container holds the material under the investigation, and the other is empty and used as the reference container. Both DSC containers are heated and cooled at the same rate. Since melting is an endothermic process, when a crystalline or semi-crystalline sample melts, more power or heat is needed to maintain the temperature of the sample. Conversely, less power or heat is

required to maintain the temperature when crystallization occurs. By plotting the heat flow as a function of time, we can identify the temperature of the phase transitions. For example, the glass transition of amorphous polymers is an endothermic process which typically corresponds to one or more endothermic peaks (shown in **Fig. 3.6 (a)**). The temperatures corresponding to energy transfer processes from the glass-transition (T_g), crystallization (T_c), melting (T_m) and degradation/decomposition (T_d) can be recorded. DSC can be used to determine the polymer crystallinity by measuring the heat associated with melting (fusion) of the polymer. A partially crystalline polymer has a melting curve which contains information on the size distribution of the crystallites present in the material. This heat is reported as percent crystallinity by normalizing the observed heat of fusion to a 100% crystalline sample of the same polymer. The crystallinity of the polymer can be calculated from the integral area of the baseline and each melting curve. Therefore, the degree of crystallization of a polymer is given by the **Eq (4)**:

$$X_c = \frac{\Delta H_m}{\Delta H_{m,p}} * 100\% \quad (4)$$

where X_c is the percent crystallinity, ΔH_m is the heat of fusion for the sample and $\Delta H_{m,p}$ is the heat of fusion for the 100% crystalline sample. In this work, DSC was performed to investigate the degree of crystallization of different solid polymer electrolytes.

On the other hand, to provide an overview of decomposition in the form of weight loss, TGA can be used. **Fig. 3.6 (b)** illustrates the procedural and the final temperatures (T_i and T_f) as well as the reaction interval (T_i - T_f), which refer to the onset of a mass change and the completion of the change, respectively.

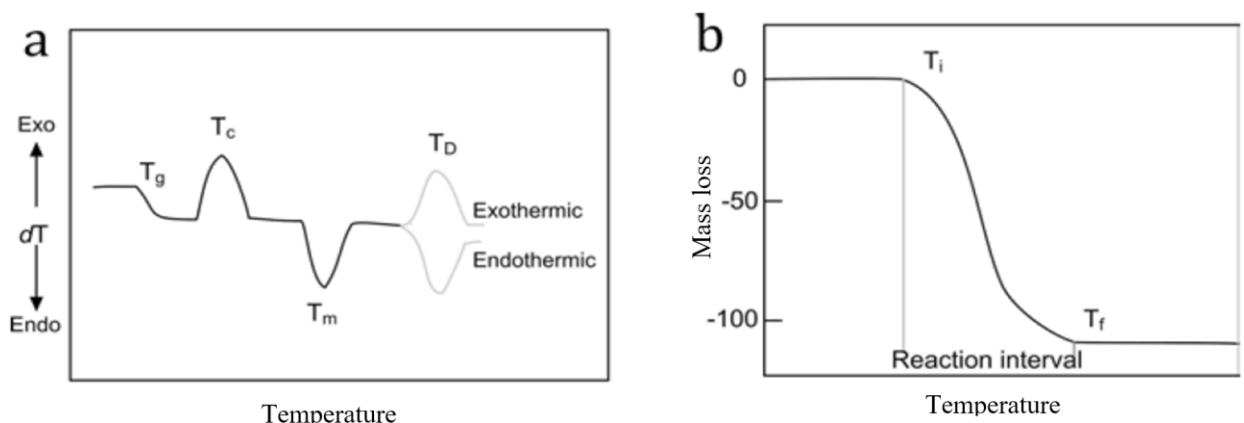


Figure 3.6: (a) DSC scan showing the key features of energy transfer processes in a polymer material; (b) thermogravimetric response illustrating the mass loss as a function of the temperature. Adapted from ref. [3]

3.8.3.1 Thermogravimetric Analysis (TGA)

The prepared electrolyte slurry was poured on to a Teflon plate and dried at room temperature under argon gas for 24 hours to remove the acetonitrile. Then the Teflon plate was placed in a desiccator and dried under vacuum at 50°C for 24 hours, at which point it was ready to be used in TGA and DSC analysis. TGA, from 25 to 600°C at 10°C/min under N₂, to confirm the amount of attached PEO and decomposition temperature, was performed.

3.8.3.2 Differential Scanning Calorimetry (DSC)

DSC was used at 10°C/min under N₂ to measure phase transition temperatures. DSC runs of 5 ~ 7 mg samples were cycled 3 ~ 4 times in the range of -100 to 130°C, in hermetically sealed aluminum pans. Melting and crystallization temperatures (when observed) were defined as the maxima of the melting endotherms and crystallization exotherms, respectively. Enthalpies of melting were reported for the second DSC cycle and were normalized for the mass of ethylene oxide units originating from the high molecular weight of PEO (400K). The glass transition temperature was determined as the mid-point of the step transition from the second heating. Degree of crystallinity was evaluated by normalized ΔH_m .

3.8.4 Data Accuracy and Precision

A variety of methods are used in statistics to characterize the accuracy of the results. The best known of such methods are confidence intervals. This method is most useful when repeated measurements are obtained, since it considers the spread in a group of values about their mean.

We applied this analysis to different groups of our calculated results (N=10). The mean value (\bar{R}) and the standard deviation (S.D.) of a set of resistances for each SPE were calculated as shown in **Table 3.5**. The **standard error of the mean** is a measure of the uncertainty of the mean and depends on the number of results. This is calculated by:

$$\text{Standard Error of the Mean} = SE = \frac{S.D.}{\sqrt{N}}$$

(5)

Finally, an uncertainty was calculated as a confidence interval. For a 95% confidence interval, there will be a 95% probability that the true value lies within the range of the calculated confidence intervals. Confidence intervals are calculated using the **Student's t-distribution**. These are tabulated values that relate the standard error of a mean to a confidence interval. Values of the t-statistic depend on the number of measurements and confidence intervals desired. The **confidence interval** is defined as the range of values calculated using the following equation:

$$\text{Confidence interval} = \bar{R} \pm (SE \times t)$$

(6)

where t is the value of the t-statistic for 10 measurements at the desired confidence interval (95%). The results of estimated uncertainty for different SPEs are summarized in **Table 3.5**. These confidence interval results mean that, there is a 95% probability that the true value of the resistance for each SPE at each current density equals its mean value \pm confidence interval.

Based on the typical accuracy of electrochemical measurements, the number of significant figures was usually limited to 3.

Table 3.5: Confidence intervals for various values of resistance of SPEs at different current densities

Sample code	Current density (A.cm ⁻²)	Mean value (\bar{R}) (Ω.cm ²)	S.D.	S.E.	Confidence intervals
PEO	1.6·10 ⁻⁵	20200	203	64	±150
	3.2·10 ⁻⁵	12000	132	41	±90
	6.5·10 ⁻⁵	4440	149	47	±106
	1.3·10 ⁻⁴	3470	169	53	±120
	3.2·10 ⁻⁴	-	-	-	-
	6.5·10 ⁻⁴	-	-	-	-
PEPV35	1.6·10 ⁻⁵	7650	172	54	±120
	3.2·10 ⁻⁵	3360	114	36	±80
	6.5·10 ⁻⁵	1850	136	43	±100
	1.3·10 ⁻⁴	1680	117	36	±80
	3.2·10 ⁻⁴	1400	107	33	±80
	6.5·10 ⁻⁴	-	-	-	-
PT10	1.6·10 ⁻⁵	6750	155	49	±110
	3.2·10 ⁻⁵	3690	114	36	±80
	6.5·10 ⁻⁵	2250	119	37	±85
	1.3·10 ⁻⁴	1280	112	35	±80
	3.2·10 ⁻⁴	790	105	33	±75
	6.5·10 ⁻⁴	520	101	31	±72
PPT	1.6·10 ⁻⁵	6560	140	44	±100
	3.2·10 ⁻⁵	3030	115	36	±80
	6.5·10 ⁻⁵	1910	112	35	±80
	1.3·10 ⁻⁴	980	114	36	±80
	3.2·10 ⁻⁴	590	104.45	33	±75
	6.5·10 ⁻⁴	500	102.47	32	±70

3.9 References

1. Franger, S.; Benoit, C.; Bourbon, C.; Le Cras, F., *Journal of Physics and Chemistry of Solids*, **2006**, *67*, 5–6, 1338-1342.
2. Macdonald, J. R.; Johnson, W. B., Fundamentals of Impedance Spectroscopy. In *Impedance Spectroscopy*, John Wiley & Sons, Inc.: 2005; pp 1-26.
3. Sun, B. Functional Polymer Electrolytes for Multidimensional All-Solid-State Lithium Batteries. Uppsala Universitet, Sweden, **2015**.

Chapter 4

4 PREPARATION AND STUDIES OF THE POLYMER COMPOSITES TO BE USED AS ELECTROLYTES IN LI ION BATTERY PROTOTYPES

The main goal of this study is to prepare and test the prototypes of novel Li ion batteries with solid polymer electrolyte and determine how the choice of the electrolyte affects the prototype properties and performance. In this chapter, we analyze the properties of selected solid polymer electrolyte systems to be used in the battery prototypes. In **Chapter 5**, we analyze the properties of the prototypes made using these solid electrolytes and determine the system that produce the batteries with the best performance.

Among the polymer system used, we studied both electrolytes based on a single polymer, poly(ethylene oxide) (PEO), as well as those based on polymer blends, specifically, blends of PEO with poly(vinyl acetate) (PVAc). The main advantages that distinguish blend-based electrolytes from other polymer ionic conductors are the simplicity of their preparation and the variety of systems which can be used as additives. It is also known (See **Chapter 2** and references therein) that incorporation of nano-sized TiO₂ fillers into PEO-based polymer electrolytes may give rise to new types of nanocomposite polymer electrolytes with improved properties. Therefore, three different classes of the PEO based electrolytes can be considered:

1. Electrolytes containing low or medium molecular weight polymers;
2. PEO-based electrolytes with dispersed inert inorganic or organic particles;
3. Blend-based composite electrolytes consisting of PEO and a low molecular weight polymer with dispersed inert inorganic or organic particles.

The aim of this chapter is to present the effect of PVAc and TiO₂ on PEO-based solid polymer electrolyte at room temperature and formulate the best blend-based composite electrolyte with the optimum amount of PVAc and TiO₂. These new kinds of nanocomposite blend polymer electrolytes are characterized by superior properties in terms of room temperature ionic conductivity and, importantly, mechanical stability.

4.1 Thermal behaviour of SPEs with different contents of PVAc

4.1.1 DSC analysis

DSC study has been used to elucidate the effect of PVAc on the thermal transitions of the PEO-based SPEs, and the results are shown in **Table 4.1**. The DSC curves for PEO, and PEO with 15, 35, and 50 wt.% PVAc polymer electrolytes (PEPV15, PEPV35, PEPV50) are shown in **Fig. 4.1**. The good miscibility between PVAc and PEO has been confirmed by the single glass transition behaviour of the PVAc : PEO : LiPF₆ matrix as shown in **Fig. 4.1**. The second and third heating scans are also performed immediately after the samples have been cooled to -100°C following the first heating. For these and all subsequent sets, the data from the third cycle was used and the reference was an empty aluminum pan.

Table 4.1: Properties of solid polymer electrolytes with different contents of PVAc were obtained from DSC heating scans (10°C per minute).

Sample code	T _g (°C)	T _m (°C)	ΔH _m (J/g)	ΔH _{rec} (J/g)	X _c (%)
PEO	-26.8	57.07	52.60	-	24.58
PEPV15	-31.17	52.79	29.62	-	13.84
PEPV35	-37.15	49.82	3.09	3.05	0.02
PEPV50	-37.40	-	-	-	-

For the above blends, the temperature T_g of the glass transition was found to decrease with an increase in the PVAc content. This can be interpreted on the basis of chain flexibility, which is reflected by T_g. This is suggestive of enhanced segmental motions at higher PVAc contents, which should result in higher conductivity.

The blend with 50 wt.% PVAc, was presumed to be completely amorphous because no melting peak was seen in the thermograms. The thermograms of blend with 35 wt.% PVAc exhibited an exothermic peak following the glass transition. This peak is attributed to recrystallization in the polymer blend, the quenched-in amorphous structure from cooling becomes sufficiently mobile above the glass transition for crystallization to occur and these crystals melt upon further heating. The values of the recrystallization (ΔH_{rec}) and melting heat (ΔH_m) of the blend were found by integrating the areas under the recrystallization and melting peaks of the DSC curve, respectively. The blend with 35 wt.% PVAc showed that the ΔH_{rec} was almost equal to the ΔH_m.

This indicates that the addition of PVAc in such concentration was able to completely suppress the crystallization of PEO in the blend during the quenching process (before recrystallization). The recrystallization peak was not observed for PEPV15, but the melting peak was still observed, with a significantly increased ΔH_m as compared to PEPV35, which indicates that PEO crystallized during the quenching process, and the PVAc content was not enough to keep PEO in the amorphous phase. The crystalline phase content X_c was found to be 13.84%, which is still significantly lower than X_c for neat PEO ($X_c = 24.58\%$). Therefore, the addition of even small amounts of PVAc could reduce the ΔH_m and X_c values, whereas the addition of 50% PVAc could entirely suppress the crystallinity in this system. However, it is not absolutely clear whether this decrease in the crystalline phase content is a result of the dilution by the amorphous component, the PEO crystallinity change, or both [1, 2].

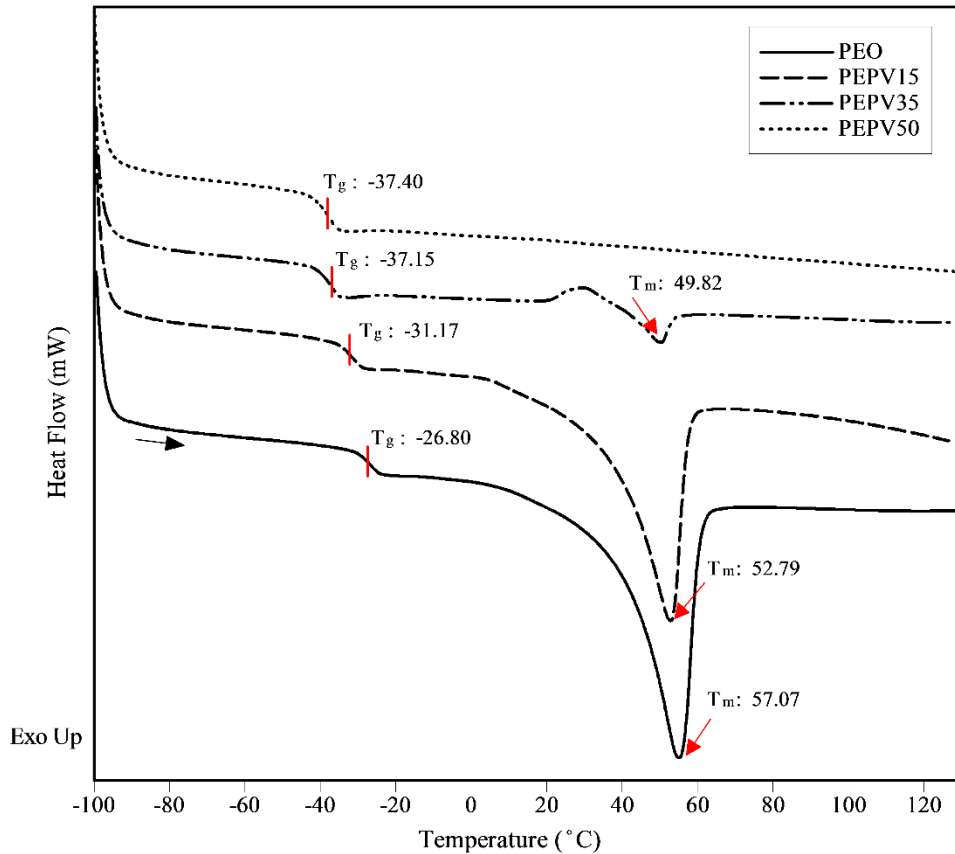


Figure 4.1: Third heating DSC curves for solid polymer electrolytes with different contents of PVAc. The temperature scan range was between -100°C and 130°C . The heating rate was $10^{\circ}\text{C}/\text{min}$.

4.1.2 TGA analysis

To ascertain the thermal stability of the polymer electrolytes, the prepared films were subjected to TGA analysis. The thermogravimetric curve and results for PEO electrolytes at various concentrations of PVAc (0, 15, 35, and 50 wt.%) are shown in **Fig. 4.2** and **Table 4.2**. At elevated temperatures up to 150°C the samples with PVAc showed more weight loss than PEO, which indicated that the addition of PVAc appears to cause a slight decrease in the thermal stability at these temperatures. However, at temperatures below 70°C, which correspond to the typical working temperatures of solid polymer electrolytes in batteries, the blends with PVAc actually showed higher stability as compared to neat PEO. Interestingly, the best stability was shown by PEPV35 blend with 35% PVAc. In all cases, the weight losses were only a few percent.

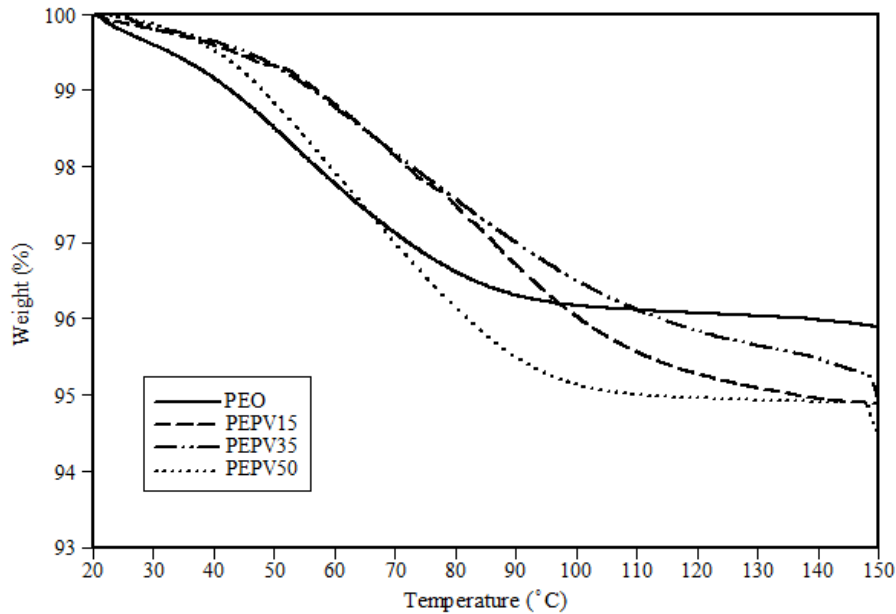


Figure 4.2: TGA curves for solid polymer electrolytes with different contents of PVAc. The heating rate was 10°C/min.

Table 4.2: Properties of solid polymer electrolytes with different contents of PVAc were obtained from TGA analysis (heating rate 10°C/min).

Solid polymer electrolyte	Weight Loss % up to 150°C
PEO	4.13
PEPV15	5.16
PEPV35	5.12
PEPV50	5.57

4.2 Thermal behaviour of SPEs with different contents of TiO₂

4.2.1 Differential scanning calorimetry (DSC)

The composite polymer electrolyte samples with varying concentration of TiO₂ nanofiller were subjected to DSC analysis and the thermograms results are shown in **Fig. 4.3** and **Table 4.3**. The PEO-based electrolyte samples with the addition of 5, 10, and 15 wt.% TiO₂ (PT5, PT10, PT15) were studied. No PVAc was added in these experiments. The data for PEO-only electrolyte are also shown for comparison. Based on the data in **Fig. 4.3**, addition of TiO₂ nanoparticles to P(EO)₁₂LiPF₆ reduces the enthalpy of melting and X_c. Furthermore, addition of 10 wt.% TiO₂ reduces ΔH_m and X_c more than the addition of 5 wt.% or 15 wt.% TiO₂ to the same P(EO)₁₂LiPF₆ systems, which is in agreement with the previous studies [3-7]. The melting and glass transition temperatures also followed the same trend and are at minimum at 10% of TiO₂. Lowering these temperatures should be favourable for the conductivity. Thus, the addition of TiO₂ strongly hinders crystallization and decreases the amount of crystalline phase in PEO. The percent of crystallinity (X_c) (**Eq. 4, chapter 3**) in the SPEs was calculated from the ratio of the enthalpy of melting per gram of PEO present in the sample to the enthalpy of melting per gram of 100% crystalline PEO. Here, the enthalpy of melting per gram of 100% crystalline PEO is taken as 214 J.g⁻¹ [8].

Table 4.3: Properties of solid polymer electrolytes with different contents (wt.%) of TiO₂ were obtained from DSC heating scans (10°C per minute).

Sample code	T _g (°C)	T _m (°C)	ΔH_m (J/g)	ΔH_{rec} (J/g)	X _c
PEO	-26.8	57.07	52.60	-	24.58
PT5	-27	55.44	34.71	-	16.21
PT10	-29.5	54.42	26.62	-	12.44
PT15	-26.7	56.86	39.44	-	18.42

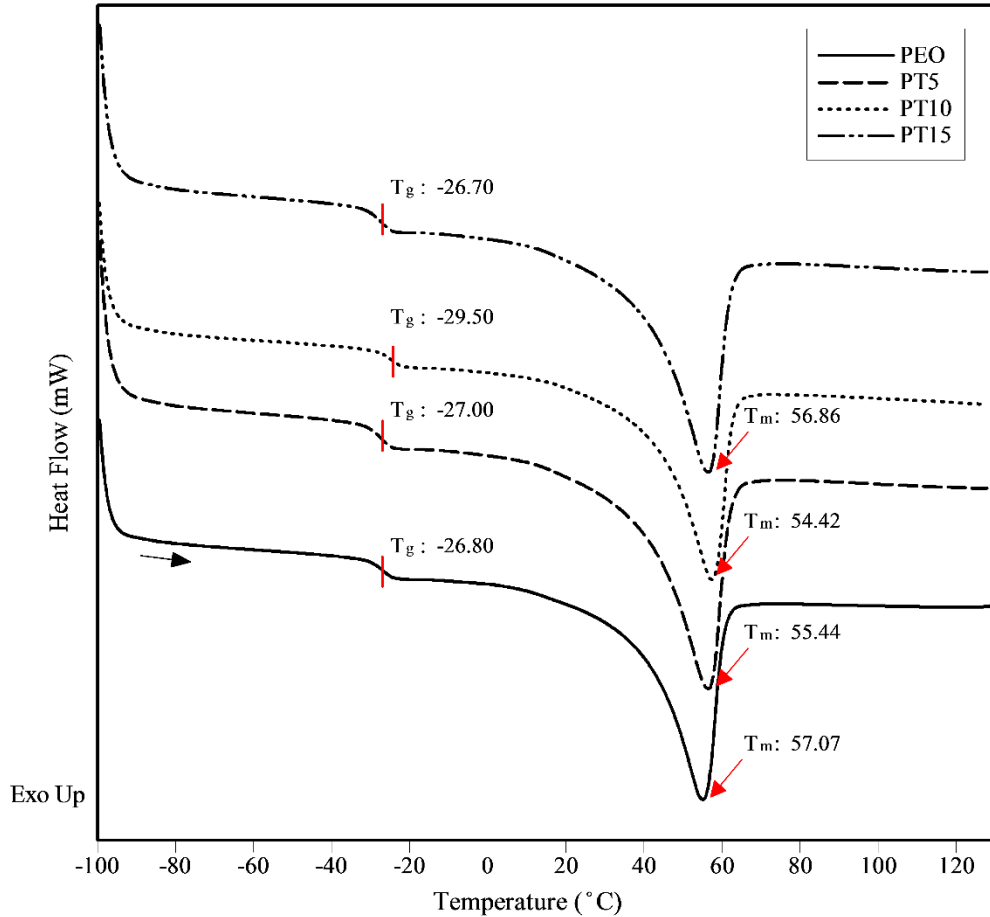


Figure 4.3: Third heating DSC curves for solid polymer electrolytes with different contents of TiO₂. The temperature scan range was between -100°C and 130°C. The heating rate was 10°C/min.

Filler addition to the PEO-salt system is expected to lower the crystallinity by increasing the volume fraction of amorphous phase due to filler-induced distortion of the polymer structure. However, as found from the data of **Table 4.3**, the filler addition does not always give rise to a definite trend between the filler content and crystallinity: addition of 5-10 wt.% TiO₂ decreased the crystallinity of PEO, whereas the addition of 15% TiO₂ nanoparticles increased the crystallinity of PEO.

This behaviour can be attributed to the changes in compatibility between TiO₂ and PEO polymer matrix. TiO₂ nanoparticles in high concentrations may act as nucleation centers, which will enhance the formation of spherulite [7] and lead to greater volume fraction of the crystalline phase. As a result, the random micro-Brownian motion of amorphous chains will be restricted when the amorphous phase is entrapped in or adjacent to more stiff large crystallites [9]. As a

result, the optimal concentration of TiO₂ nanofiller for our purposes was determined to be 10 wt.%.

4.2.2 TGA measurements

The thermal stability of SPE films were measured by thermogravimetric analysis (TGA). The TGA curves are shown in **Fig. 4.4** and the numerical results are shown in **table 4.4**. It can be clearly seen that all samples exhibit minimal weight loss until the temperature reached 150°C. It can be noticed that PEO lost around 5% of its weight up to 150°C, while the films with TiO₂ nanoparticles showed an even better thermal stability that correlated with the amount of TiO₂ added. It is concluded that the addition of inorganic filler effectively increased the thermal stability of the electrolyte.

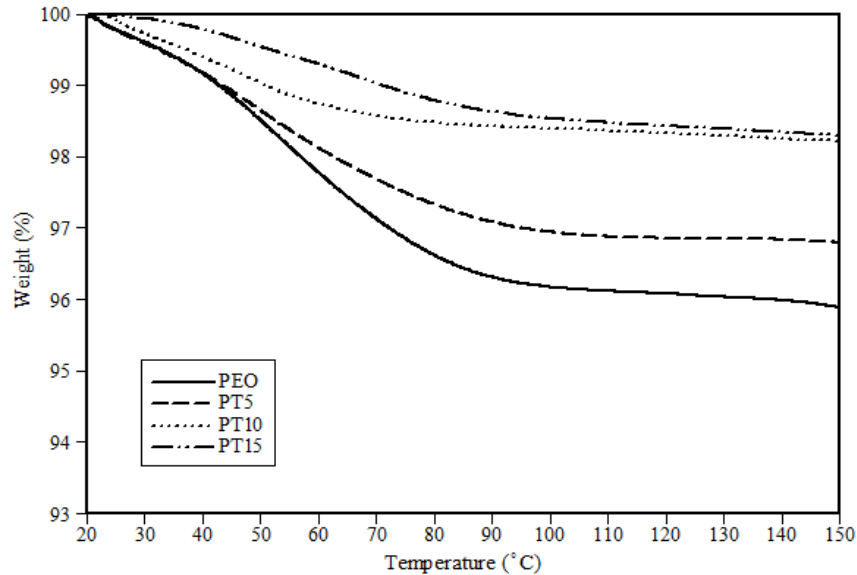


Figure 4.4: TGA curves for solid polymer electrolytes with different contents of TiO₂. The heating rate is 10°C/min.

Table 4.4: Properties of solid polymer electrolytes with different contents of TiO₂ obtained from TGA analysis (10°C per minute).

Solid polymer electrolyte	Weight Loss % up to 150°C
PEO	4.13
PT5	3.23
PT10	1.79
PT15	1.71

4.3 Thermal behaviour of SPEs with the optimum contents of PVAc and TiO₂

4.3.1 DSC analysis

In this set of experiments, we compare the DSC and TGA data for the following SPE systems: P(EO)₁₂LiPF₆, the best PEO-PVAc system (PEPV35) with 35 wt.% of PVAc, the best PEO-TiO₂ system (PT10) with 10 wt.% of TiO₂, and the new multicomponent system (PPT) containing both 35 wt.% PVAc and 10 wt.% of TiO₂. The DSC measurements clearly show the advantages of PPT over PEO, PT and PEPV systems. Based on the data in **Table 4.5** and **Fig. 4.5**, the addition of 10 wt.% TiO₂ to the PEO-LiPF₆ system containing 35 wt% PVAc reduces the enthalpy of melting and X_c even more than the addition of 10 wt.% TiO₂ only. The decrease of X_c with the addition of TiO₂ and PVAc can be explained as follows: after the addition of LiPF₆, PVAc and TiO₂ to the crystalline PEO-based electrolytes, there is a competition between TiO₂ acidic groups and alkali metal cations for the ether and ester oxygen centers of PEO and PVAc, respectively. Ti containing groups can act as nucleation centres in the crystallization of PEO from acetonitrile solutions. Since there are a large number of these centers, the crystallization proceeds more rapidly and, as a result, more disorder is frozen into the new solid. This is manifested by a decrease in the fraction of the crystalline PEO phase as shown in **Fig. 4.5** and **Table 4.5** for the PEO-PVAc-TiO₂-LiPF₆ composite electrolyte. It should be noted that based on the DSC data alone, PEO-PVAc electrolyte has a slightly lower crystallinity without TiO₂; however, crystallinity is not the only factor and the addition of TiO₂ gives rise to the other properties that are beneficial for solid polymer electrolytes in batteries (see below).

Table 4.5: Properties of solid polymer electrolytes with and without 10 wt.% TiO₂ and/or 35 wt.% PVAc obtained from DSC heating scans (10°C per minute).

Sample code	T _g (°C)	T _m (°C)	ΔH _m (J/g)	ΔH _{rec} (J/g)	X _c (%)
PEO	-26.8	57.07	52.60	-	24.58
PEPV35	-37.15	49.82	3.093	3.051	0.02
PT10	-29.5	54.42	26.62	-	12.44
PPT	-36.21	50.19	7.946	8.364	0.19

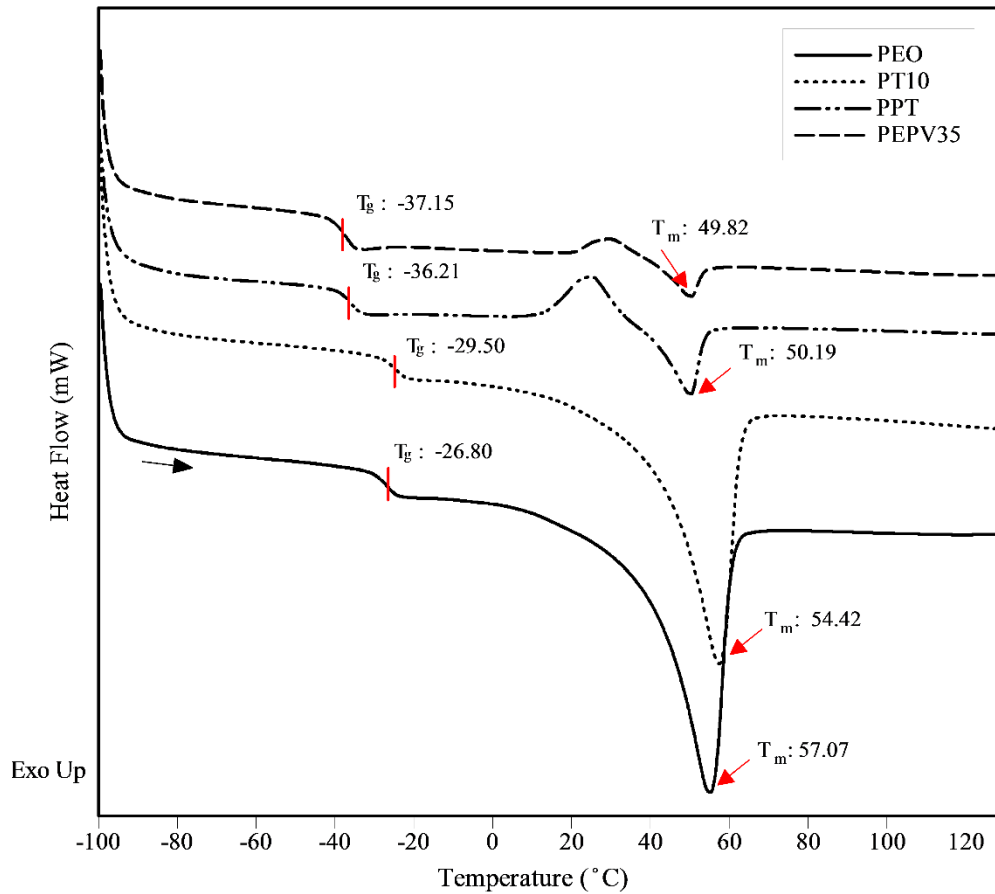


Figure 4.5: Third heating DSC curves for solid polymer electrolytes with and without 10 wt.% TiO₂ and/or 35 wt.% PVAc. The temperature scan range was between -100°C and 130°C. The heating rate was 10°C/min.

4.3.2 TGA analysis

In order to compare the thermal behaviour of the optimized samples, TGA was recorded (**Fig. 4.6** and **Table 4.6**). From the thermogram, it is observed that all the samples were thermally stable up to 150°C. The samples without TiO₂ nanoparticles exhibited gradual weight loss of about 5% in the temperature range 25-150°C, whereas the addition of inorganic nano-fillers (TiO₂) improved the stability and decreased the weight loss to 2%, which is due to the removal of the residual solvent and the moisture [10].

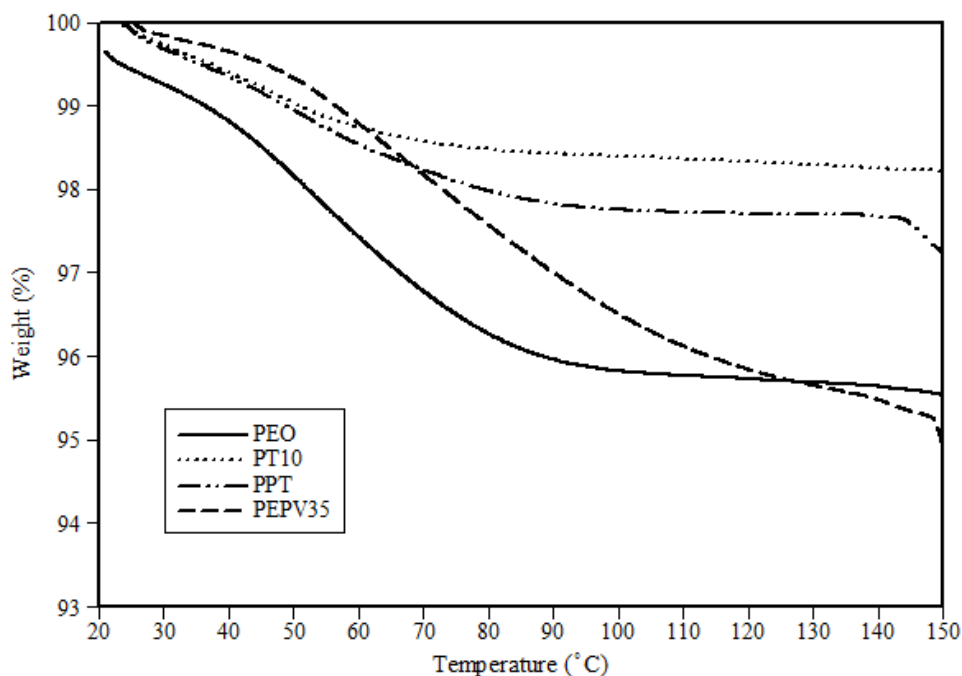


Figure 4.6: TGA curves for solid polymer electrolytes with and without 10 wt.% TiO₂ and/or 35 wt.% PVAc. The heating rate is 10°C/min.

Table 4.6: Properties of solid polymer electrolytes with and without 10 wt.% TiO₂ and/or 35 wt.% PVAc obtained from TGA analysis (10°C per minute).

Solid polymer electrolyte	Weight Loss % up to 150°C
PEO	4.13
PEPV35	5.12
PT10	1.79
PPT	2.77

4.3.3 Transport mechanism of ions in the PEO-PVAc-TiO₂ system

The polymer structure of PVAc and PEO are illustrated in **Fig. 4.7**. When an electric field is applied across the sample, the polar groups present in the polymer blends (C=O, C(O)-O-C, and C-O-C) may become polarized and form dipoles, which will interact with the corresponding ions due to the coulombic electrostatic forces. It has also been reported that the free Li⁺ ion has more mobility than free PF₆⁻ ion whose mobility is greater than that of ion pairs [11-14]. The interaction of ester and ether oxygens with the Li⁺ assists the cations in their transport through the polymer chains. According to Druger *et al.* ion conduction in polymer electrolytes may take place by hopping of ions through inter-chain and intra-chain ion movement [15, 16]. The Li⁺ ion

transportation in the present system may happen through the ester oxygen centers of PVAc as well as the ether oxygen centers of PEO by inter- and intra-chain ion hopping during the process of segmental mobility. At higher PVAc concentration there might be more vacancies for the ions to move. The proposed coordination of cation with the ester oxygen and C-O in PVAc-LiPF₆ polymer complex is shown in **Scheme 4.1**.

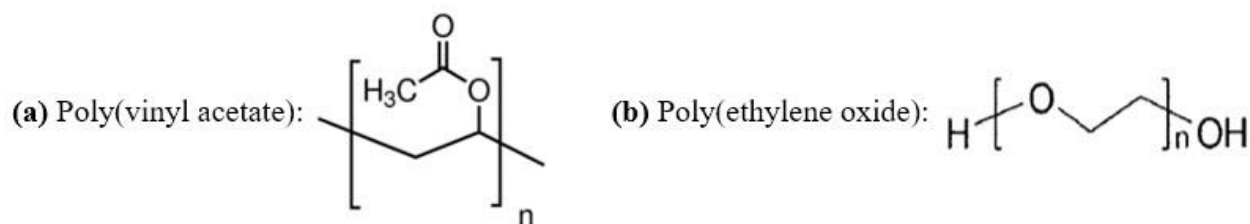
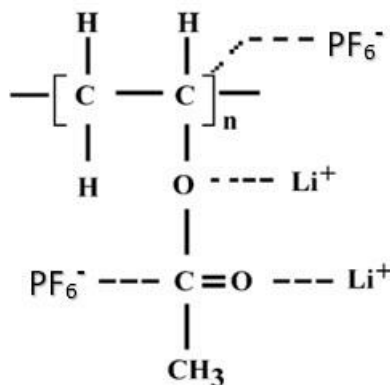


Figure 4.7: Polymers structure (a) PVAc, (b) PEO.



Scheme 4.1: The coordination of cation with the ester oxygen and C-O in PVAc-LiPF₆ polymer complex. Reproduced from ref. [17].

According to Croce *et al.* [18], the Lewis acid groups of the inert filler added to the electrolyte may compete with the Lewis acid-type lithium cations for the formation of complexes with polymer chains as well as the anions of the added lithium salt. The Lewis acid-base interaction centers react with the electrolytic species, which lowers the ionic coupling and promotes the salt dissociation via a sort of “ion-filler complex” formation. Therefore, at low filler contents, TiO₂ would contribute to dissociation of lithium salt, resulting in enhancement of the total ionic conductivity. However, at high filler contents, continuous non-conductive phase built up by the large amount of filler (which is an electrically inert component) blocks up the lithium ion transport, which results in an increase in the total resistance of the composite polymer electrolyte [19, 20].

According to these models, yet another effect of the added filler may be structural modifications and changes in the morphology of composite electrolytes due to the specific actions of the polar groups, which may act as cross-linking centers for the PEO segments and for the PF_6^- anions, thus lowering the PEO reorganization tendency. The expected effect of such structural modification is the promotion of Li^+ conducting pathways at the filler surface which, together with the interaction of ester and ether oxygens with the Li^+ , should assist the cations in their transport through the polymer chains. These two effects would result in the promotion of 'free' ions and may, indeed, account for the enhancement of the conductivity of the nanocomposites at ambient temperatures.

4.4 Summary

Calorimetric data were obtained for blends of PVAc, with a nominal molecular weight of 140,000, and high molecular weight poly(ethylene oxide), PEO (M_w 400,000), with LiPF_6 at O:Li ratios of 12:1. From the depression of crystallization rate and melting point and the single T_g of the blend, it was inferred that the PVAc-PEO blends were miscible. The crystallization of PEO was easily suppressed by blending it with PVAc.

For the PEPV50 blends, incorporation of 50 wt.% PVAc completely suppressed the crystallinity of the PEO. The blends were all viscoelastic, with mechanical strengths increasing with decreasing PVAc concentration due to decreased crystallinity and dilution of the polymer blends. Increasing the ratio of PVAc to PEO decreased the crystallinity at room temperature, but the mechanical stability was limited by the amount of PVAc that could be incorporated into the PEO; consequently, this optimized concentration of PVAc was found to be 35 wt.%.

It has been shown that mixing with 10 wt.% of TiO_2 nanoparticles in P(EO)_{12} - LiPF_6 matrix system presented an excellent thermal stability. The addition of lower concentrations of TiO_2 nanoparticles (up to 10 wt.%) are more compatible with PEO matrix, proven by the lowered crystallinity, T_g and T_m . At high concentration of TiO_2 , negligible decrement of crystallinity was observed since TiO_2 nanoparticles in PEO matrix act more likely as inert foreign particles serving as nucleation centers of the crystalline polymer phase.

After founding the optimum content of each component, a new type of blended composite polymer electrolyte has been made by adding 35 wt.% PVAc and 10 wt.% TiO₂ to PEO-based solid polymer electrolyte with LiPF₆ (O:Li = 12:1). The new electrolyte had an amorphous structure with a crystallinity as low as 0.19%, the glass transition temperature of -36.21°C and an excellent thermal stability. The low glass transition temperature, suppression of crystallinity and the presence of TiO₂ nanocrystalline filler were expected to contribute to enhanced dissociation of the lithium salt and improved conductivity of the corresponding solid polymer electrolytes at room temperature, which was confirmed by the subsequent electrochemical studies.

4. 5 References

1. Wu, W. B.; Chiu, W. Y.; Liao, W. B., *Journal of Applied Polymer Science*, **1997**, *64*, 3, 411-421.
2. Ramesh, S.; Winie, T.; Arof, A. K., *European Polymer Journal*, **2007**, *43*, 5, 1963-1968.
3. Ji, K.-S.; Moon, H.-S.; Kim, J.-W.; Park, J.-W., *Journal of Power Sources*, **2003**, *117*, 1-2, 124-130.
4. Pan, C.-y.; Feng, Q.; Wang, L.-j.; Zhang, Q.; Chao, M., *Journal of Central South University of Technology*, **2007**, *14*, 3, 348-352.
5. Liang, G.; Xu, J.; Xu, W.; Shen, X.; Bai, Z.; Yao, M., *Journal of Wuhan University of Technology-Mater. Sci. Ed.*, **2012**, *27*, 3, 495-500.
6. Lakshman Dissanayake, M. A. K., *Ionics*, **2004**, *10*, 3, 221-225.
7. Yarmolenko, O. V.; Khatmullina, K. G.; Bogdanova, L. M.; Shuvalova, N. I.; Dzhavadyan, E. A.; Marinin, A. A.; Volkov, V. I., *Russian Journal of Electrochemistry*, **2014**, *50*, 4, 336-344.
8. Jelena D. Djokić, A. K., Dušica Stojanović, Aleksandar Marinković, Goran Vuković, Radoslav Aleksić, Petar S. Uskoković, *Journal of the Serbian Chemical Society*, **2012**.
9. Walczak, M. Role and properties of the confined amorphous phase of polymers. Ecole nationale supérieure d'arts et métiers - ENSAM, 2012.
10. Mohamed Ali, T.; Padmanathan, N.; Selladurai, S., *Ionics*, **2013**, *19*, 8, 1115-1123.
11. Selvasekarapandian, S.; Baskaran, R.; Kamishima, O.; Kawamura, J.; Hattori, T., *Spectrochim Acta A Mol Biomol Spectrosc*, **2006**, *65*, 5, 1234-1240.
12. Baskaran, R.; Selvasekarapandian, S.; Kuwata, N.; Kawamura, J.; Hattori, T., *Journal of Physics and Chemistry of Solids*, **2007**, *68*, 3, 407-412.
13. Baskaran, R.; Selvasekarapandian, S.; Kuwata, N.; Kawamura, J.; Hattori, T., *Solid State Ionics*, **2006**, *177*, 26-32, 2679-2682.
14. Jacobs, P. W. M.; Lorimer, J. W.; Russer, A.; Wasiucionek, M., *Journal of Power Sources*, **1989**, *26*, 3, 483-489.
15. Golodnitsky, D.; Strauss, E.; Peled, E.; Greenbaum, S., *Journal of The Electrochemical Society*, **2015**, *162*, 14, A2551-A2566.
16. Druger, S. D.; Ratner, M. A.; Nitzan, A., *Physical Review B*, **1985**, *31*, 6, 3939-3947.

17. Selvasekarapandian, S.; Baskaran, R.; Kamishima, O.; Kawamura, J.; Hattori, T., *Spectrochimica Acta Part A: Molecular and Biomolecular Spectroscopy*, **2006**, *65*, 5, 1234-1240.
18. Croce, F.; Persi, L.; Ronci, F.; Scrosati, B., *Solid State Ionics*, **2000**, *135*, 1-4, 47-52.
19. Croce, F.; Curini, R.; Martinelli, A.; Persi, L.; Ronci, F.; Scrosati, B.; Caminiti, R., *The Journal of Physical Chemistry B*, **1999**, *103*, 48, 10632-10638.
20. Appetecchi, G. B.; Hassoun, J.; Scrosati, B.; Croce, F.; Cassel, F.; Salomon, M., *Journal of Power Sources*, **2003**, *124*, 1, 246-253.

Chapter 5

5 ELECTROCHEMICAL PROPERTIES OF LI ION BATTERY PROTOTYPES WITH SOLID POLYMER ELECTROLYTES

The aim of this chapter is to fabricate and investigate Li ion battery prototypes made using selected solid polymer electrolytes. The main parameters that determine the performance of a battery are:

1. The discharging voltage, coulombic efficiency, and the number of the charge-discharge cycles. These parameters show the performance of the battery.
2. An additional and very important parameter that may limit the battery performance is the resistance of the electrolyte. High electrolyte resistance will have a crucial effect on the charging and discharging voltage and current, thus severely limiting the power the battery can produce.

An additional factor studied in this work is the effect of the type and composition of the electrolyte on the electroformation of the porous nanostructures on the surface of the bulk aluminum that forms the anode in our battery prototypes. It can be anticipated that this process will occur differently in different electrolyte systems, as dependent on the electrolyte conductivity, distribution of the resistivity and currents during the electroformation process, as well as the mechanical stability of the polymer electrolyte and its ability to withstand the volume changes that accompany the charging-discharging and electroformation processes. Eventually, the battery prototype with the best performance is introduced.

It needs to be mentioned that the focus of this chapter is more on the discharging portion of the cycles. The mechanism of the charging and electroformation processes in our systems is less understood and is the subject of a separate study currently underway in our group.

5.1 Galvanic cycles of the battery prototypes

Shown in **Fig. 5.1** are typical galvanic cycles measured for a battery prototype utilizing an Al anode and LiFePO_4 cathode as well as a PEPV35 solid polymer electrolyte at a current density of

$1.3 \cdot 10^{-4} \text{ A.cm}^{-2}$. One can see that the battery prototype could readily withstand 100 charging-discharging cycles without noticeable changes.

Fig. 5.2 (a)-(c) show the characteristic features of the 2nd, 50th, and 100th cycles, respectively. The galvanic cycles show the charging and discharging regions, the IR drop due to the electrolyte resistance, the coulombic efficiency and the discharging voltage.

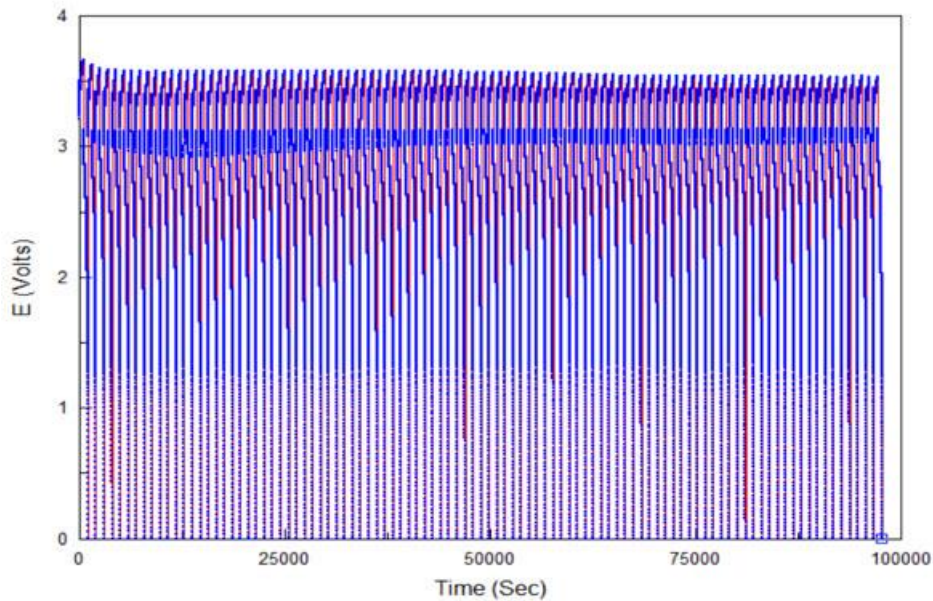


Figure 5.1: Battery galvanic cycles of sample with a PEPV35 solid polymer electrolyte, LiFePO_4 cathode and an Al anode at current density of $1.3 \cdot 10^{-4} \text{ A.cm}^{-2}$ for 100 cycles.

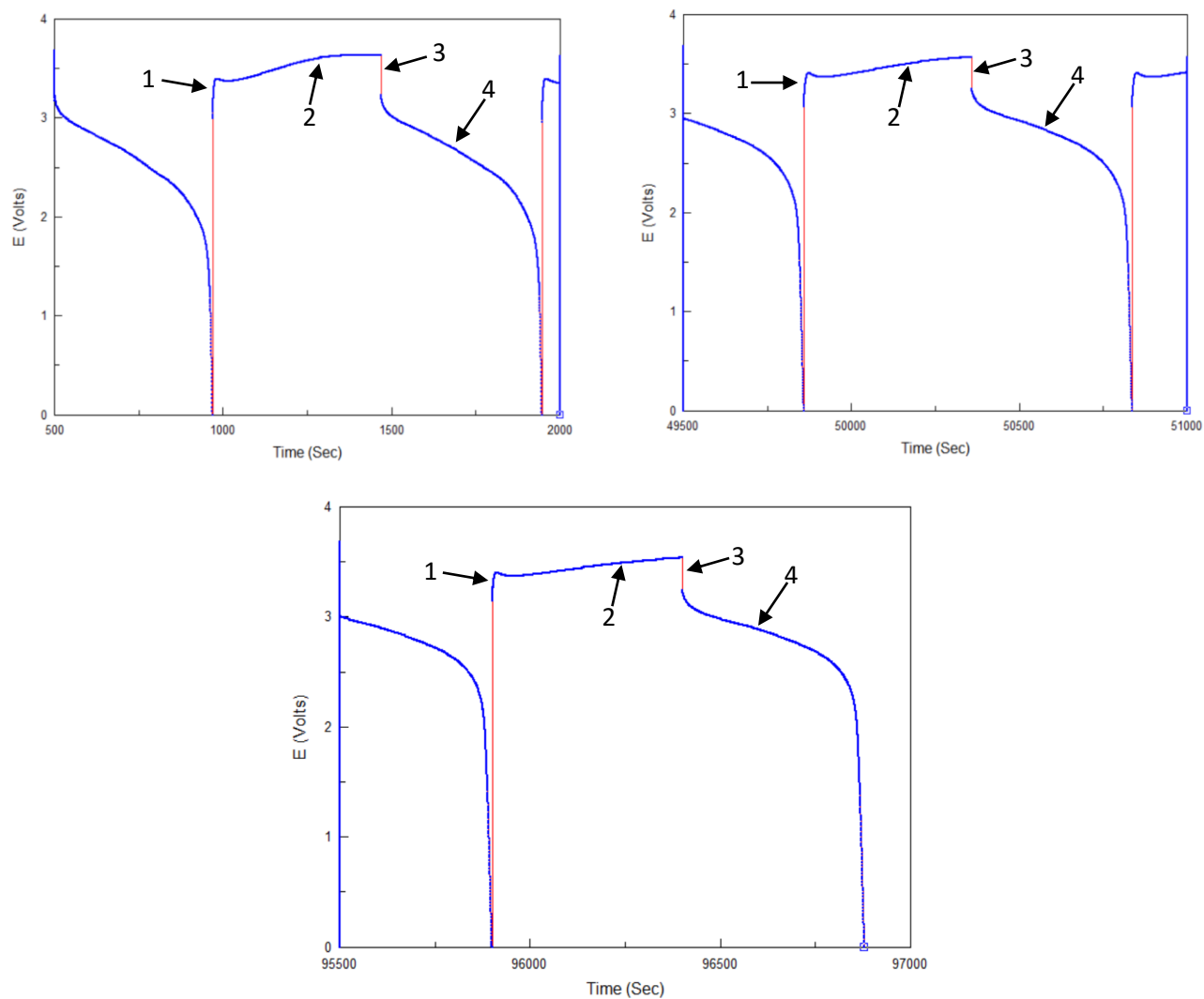


Figure 5.2: Battery galvanic cycles of prototype with a PEPV35 solid polymer electrolyte, LiFePO₄ cathode and an Al anode at current density of $1.3 \cdot 10^{-4} \text{ A.cm}^{-2}$ for 100 cycles. (a) 2nd, (b) 50th, (c) 100th cycle.

As described in **chapter 3, section 3.8.1.1**, after applying the current density that charges the prototype, a small overshoot of the potential was observed at the beginning of each charging region, which indicates the start of the charging process (1). Most likely this local potential maximum is associated with the formation of new LiAl phase in the porous structure that has been formed before (during the electroformation procedures, the aluminum electrode was pre-conditioned by galvanic cycles at low current densities of $1.6 \cdot 10^{-5}$ and $3.2 \cdot 10^{-5} \text{ A.cm}^{-2}$). Formation of a new phase usually requires a higher overvoltage. This overshooting potential was followed by a charging plateau (2). This indicates that the porous nanostructure starts forming at

the beginning of the cycles, then spreads across the reacted surface area of the anode as the battery proceeds through consecutive cycles of charging and discharging.

As described in **Chapter 1, section 1.1.1.1**, this porous nanostructure represents the new LiAl phase formed during the electroformation process. In this process, new portions of LiAl phase are formed at the surface of Al anodes. This is accompanied by a significant volume change. When discharged, the LiAl phase undergoes delithiation, which is accompanied by a decrease in the phase volume. However, the expanded portions of the Al anode cannot return to its original shape and form a porous sponge-like nanostructure instead. Next lithiation cycles are also accompanied by the volume changes, but these processes now occur predominantly in the pores of the existing nanostructure without additional volume changes, which is extremely favorable for the reversibility of the processes occurring at the battery anodes. However, if the charge passed during the charging process exceeds the amount of charge passed previously during the charging-discharging processes, new portion of the nanostructured phase will be formed. This requires a higher overvoltage and is seen as the additional growth in the potential in the charging cycles.

By applying the opposite current density the IR drop was observed (3) which was then followed by a long discharging plateau (4) involving delithiation of the anode and lithiation of the cathode. It is terminated when all the LiAl phase formed at the anode is delithiated as indicated by the drop in the battery output voltage. **Fig. 5.3** shows the Voltage/time profile of the last charge/discharge cycles obtained at current density of $1.3 \cdot 10^{-4} \text{ A.cm}^{-2}$ for 100 cycles for an Al/SPE/LiFePO₄ polymer cell. It can be clearly seen that the charging plateau of all the samples is flat except the cell with a PEO solid polymer electrolyte. The appearance of different charging plateau and a greater IR drop for the battery with a PEO SPE may be related to a difference in the mechanical properties of this electrolyte.

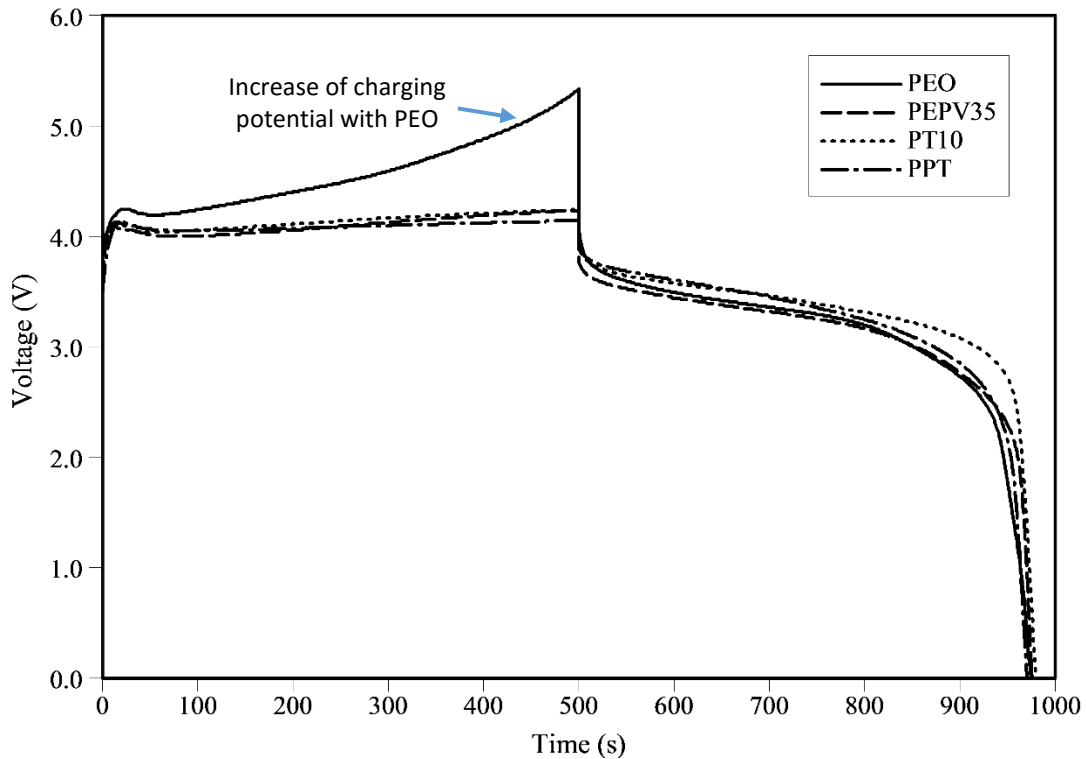


Figure 5.3: Voltage/time profile of the last charge/discharge cycles obtained at current density of $1.3 \cdot 10^{-4} \text{ A.cm}^{-2}$ for 100 cycles for an Al/SPE/LiFePO₄ polymer cell. See the legend for different types of SPEs.

The coulombic efficiency and the discharging voltage are crucial parameters that determine the performance of the battery and were calculated as mentioned in **chapter 3, section 3.8.1.1**.

5.2 Solid polymer electrolytes with different contents of PVAc

The concentration dependencies of resistance as determined from galvanic cycles for PEO blends with 15, 35, and 50 wt.% PVAc polymer electrolytes (PEPV15, PEPV35, PEPV50) as well as neat P(EO)₁₂LiPF₆ (PEO) are presented in **Fig. 5.4** and **Table 5.1**. The ambient temperature resistance of these blends was found to decrease with an increase in the PVAc content. Similar effect (maximum conductivity by adding of amorphous polymer) was observed by many authors [1-5] and is discussed in **Chapter 2**. In brief, it is believed that such a relationship between ionic conductivity and polymer blend composition is a consequence of a combination of two different processes; (1) decreasing the PEO-crystallinity and (2) a diluent effect of the other component. In fact, many reasons have been used for the interpretation of electrical data of the polymer blends, such as changing in segmental motion and as a consequence in ion motion, dielectric and

viscosity changes. These effects can be observed mainly in mostly amorphous and homogeneous regions of polymer systems [5, 6].

It can be also seen from the figure that the resistance of the electrolyte does not remain constant and varies both with the current density and increasing the number of cycles. This effect is related to the changes in the contact area between the anode and electrolyte due to continuing electroformation of the LiAl nanostructure and will be discussed in more detail later.

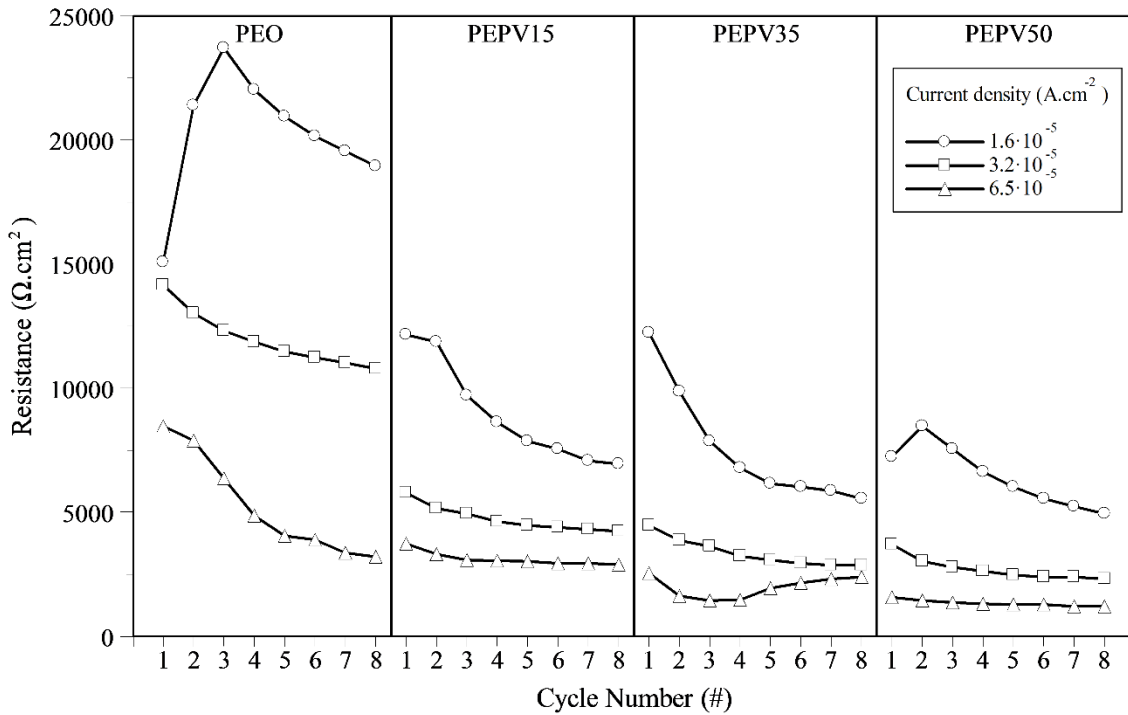


Figure 5.4: Resistance of solid polymer electrolytes with different contents of PVAc, with LiFePO₄ cathode and an Al anode at current densities of $1.6 \cdot 10^{-5}$, $3.2 \cdot 10^{-5}$, and $6.5 \cdot 10^{-5}$ A.cm⁻².

Table 5.1: The average resistance (Ω.cm²) of solid polymer electrolytes with different contents of PVAc, with LiFePO₄ cathode and an Al anode.

Current density (A.cm ⁻²)	PEO	PEPV15	PEPV35	PEPV50
$1.6 \cdot 10^{-5}$	20200	9000	7600	6400
$3.2 \cdot 10^{-5}$	11900	4700	3300	2700
$6.5 \cdot 10^{-5}$	4400	3100	1800	1300

The coulombic efficiency of the PEO-based electrolytes at various concentrations of PVAc (0, 15, 35 and 50 wt.%) are shown in **Fig 5.5** and **Table 5.2**. In general, comparable battery performance at lower current densities with different PVAc contents in the SPEs was observed.

The charge/discharge response is reasonably stable and the coulombic efficiency exceeds 93%. It can be seen that the coulombic efficiency was limited by the amount of PVAc that could be incorporated into the PEO. The blend with 50 wt.% PVAc, showed the lowest resistance among all samples, but the coulombic efficiency was also found to be the lowest. This may be related to two factors. First, PVAc is known [7] to have a narrower electrochemical window and thus may undergo electrochemical oxidation and reduction upon charging-discharging of the battery prototype. This will lower the coulombic efficiency of the battery containing this component as an electrolyte. Next, PEPV blends with high amounts of PVAc were shown to be relatively soft and have poorer mechanical stability. This may affect the growth of the LiAl nanostructure as discussed below. At the same time, the battery sample with a PEPV35 SPE showed a low resistance ($1800 \Omega \cdot \text{cm}^2$ at high current density) as well as high coulombic efficiency (94%). Consequently, the blend of 35 wt.% PVAc and 65 wt.% PEO appears to be most suitable for the reversibility of lithiation/delithiation and controlling the growth of the LiAl alloy nanostructure on the aluminum surface, as well as for Li transport through the film.

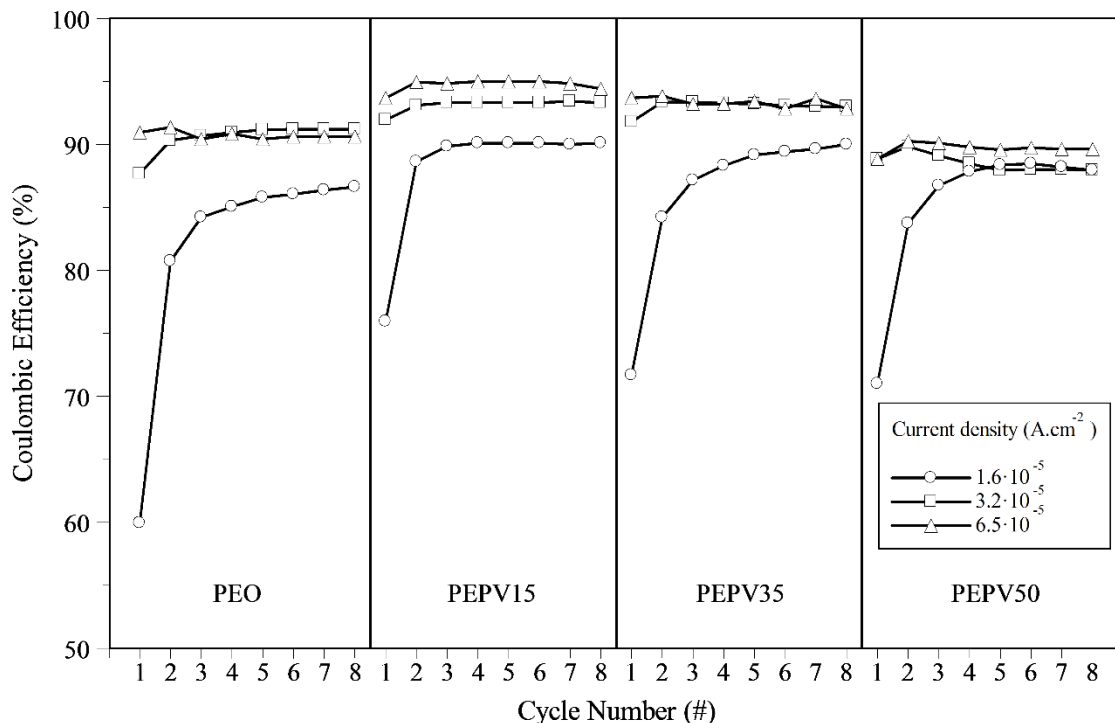


Figure 5.5: Coulombic efficiency of solid polymer electrolytes with different contents of PVAc, with LiFePO_4 cathode and an Al anode at current densities of $1.6 \cdot 10^{-5}$, $3.2 \cdot 10^{-5}$, and $6.5 \cdot 10^{-5} \text{ A} \cdot \text{cm}^{-2}$.

Table 5.2: The average coulombic efficiency (%) of solid polymer electrolytes with different contents of PVAc, with LiFePO₄ cathode and an Al anode.

Current density (A.cm ⁻²)	PEO	PEPV15	PEPV35	PEPV50
1.6·10 ⁻⁵	81.8	88.1	86.9	86
3.2·10 ⁻⁵	90.5	93.1	93	88.5
6.5·10 ⁻⁵	90.2	94.4	93.8	89.7

5.3 Solid polymer electrolytes with different contents of TiO₂

The concentration dependencies of resistance for PEO electrolytes at various concentrations of TiO₂ (0, 5, 10, and 15 wt.%) are shown in **Fig. 5.6** and **Table 5.3**. No PVAc was added in these experiments. Based on the data in **Fig. 5.6**, addition of TiO₂ nanoparticles to the PEO-based electrolytes in concentrations up to 10 wt.% decreases the bulk electrolyte resistance. The composite polymer electrolyte with 15 wt.% TiO₂ shows higher resistance, which was expected based on our DSC results (Section 4.2.1). At higher concentrations of TiO₂, inter-particle interaction may lead to aggregation of particles and blockage of the conduction pathways. It is believed that filler addition to the P(EO)₁₂LiPF₆ system helps to increase the conductivity of composite polymer electrolyte in two ways [8-11]: (1) increasing the volume fraction of amorphous phase of PEO matrix which improves the Li⁺ transport, by lowering the PEO reorganization tendency; and (2) providing Li⁺ conducting pathways at the fillers' surface through Lewis acid-base reactions occurring among species in the composite polymer electrolyte. This was extensively discussed in the previous chapter.

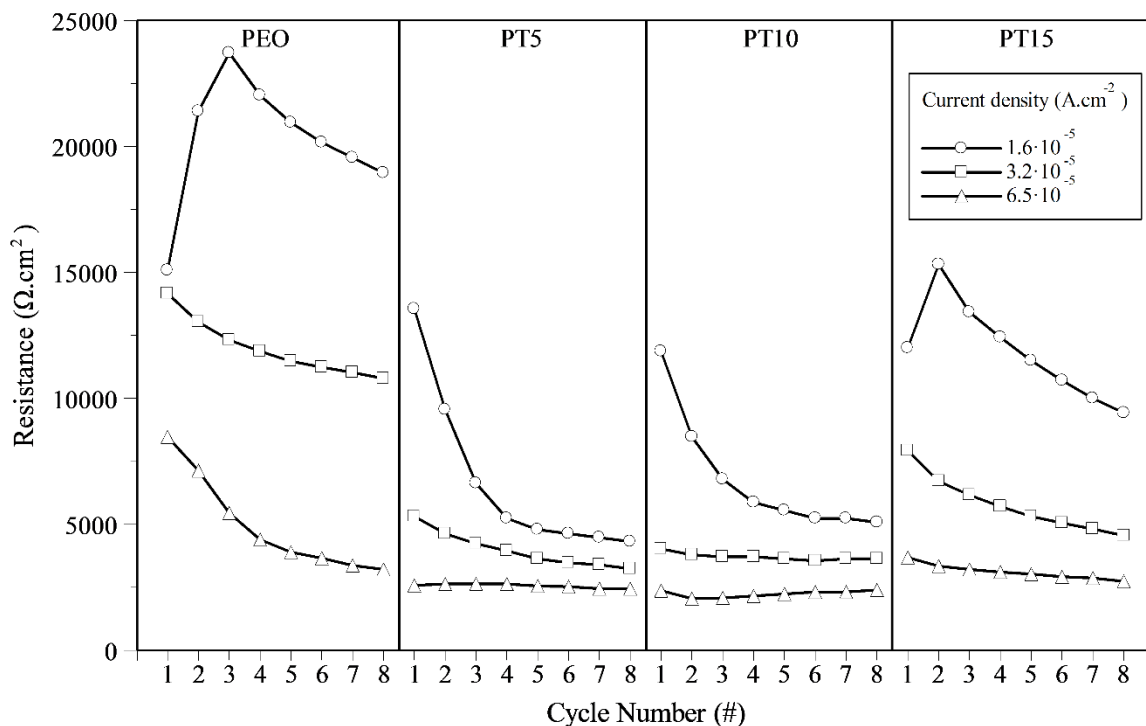


Figure 5.6: Resistance of solid polymer electrolytes with different contents of TiO₂, with LiFePO₄ cathode and an Al anode at current densities of $1.6 \cdot 10^{-5}$, $3.2 \cdot 10^{-5}$, and $6.5 \cdot 10^{-5}$ A.cm⁻².

Table 5.3: The average resistance ($\Omega \cdot \text{cm}^2$) of solid polymer electrolytes with different contents of TiO₂, with LiFePO₄ cathode and an Al anode.

Current density (A.cm ⁻²)	PEO	PT5	PT10	PT15
$1.6 \cdot 10^{-5}$	20200	6600	6700	11800
$3.2 \cdot 10^{-5}$	11900	4000	3700	5800
$6.5 \cdot 10^{-5}$	4400	2500	2200	3100

The values of the coulombic efficiency of battery prototypes utilizing PT5, PT10 and PT15 solid polymer electrolytes were again calculated from galvanic cycles and the results are presented in **Fig. 5.7** and **Table 5.4**. It can be clearly seen that all prototypes with TiO₂ showed higher coulombic efficiency than those based on neat PEO SPE due to the presence of inorganic fillers which improved the mechanical stability. These considerations point out that an optimum concentration of TiO₂ nanoparticles yields the lowest resistance as well as high efficiency values in a composite polymer electrolyte. Incorporation of 10 wt.% TiO₂ into PEO-based polymer electrolyte showed the resistance as low as 2200 $\Omega \cdot \text{cm}^2$ and the coulombic efficiency as high as 94%. Therefore, the optimal concentration of TiO₂ nanofillers was determined to be 10 wt.%. These results are in accordance with earlier reported results wherein a decrease in conductivity

was observed for similar loadings of the filler content [12-15]. Importantly, the PT5 and PT10 formulations also showed little variations of both the resistance and the coulombic efficiency with the current density and the number of cycles thus pointing out high electrochemical stability and controlled electroformation of LiAl nanostructure in these conditions.

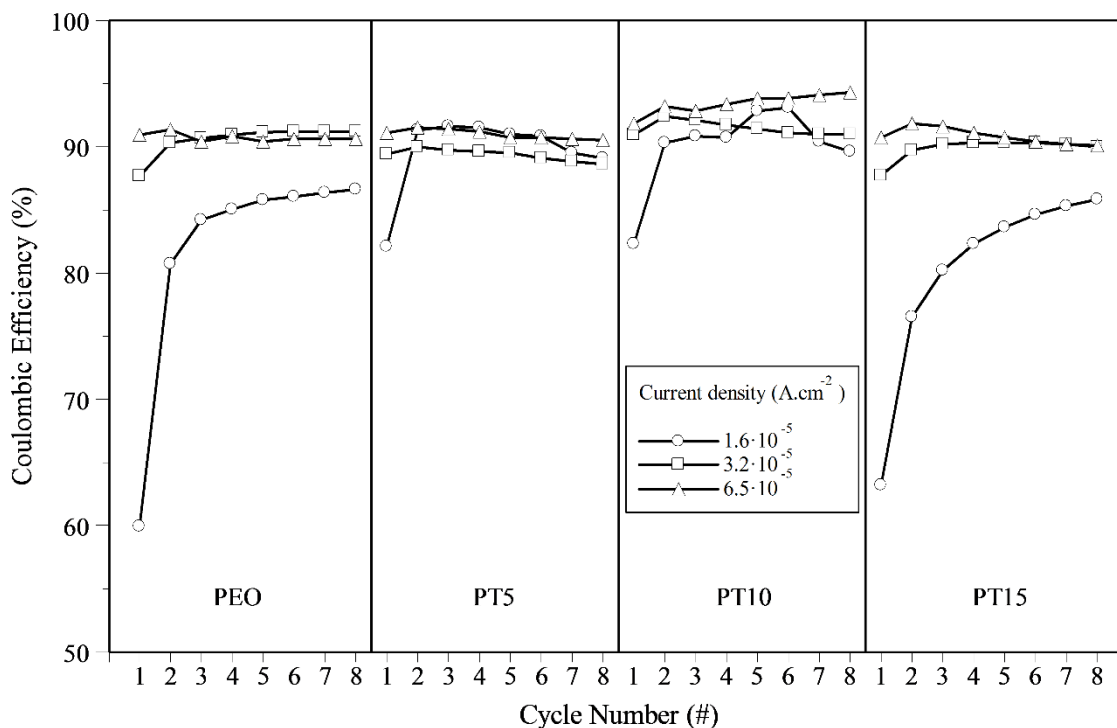


Figure 5.7: Coulombic efficiency of solid polymer electrolytes with different contents of TiO_2 , with LiFePO_4 cathode and an Al anode at current densities of $1.6 \cdot 10^{-5}$, $3.2 \cdot 10^{-5}$, and $6.5 \cdot 10^{-5} \text{ A.cm}^{-2}$.

Table 5.4: The average coulombic efficiency (%) of solid polymer electrolytes with different contents of TiO_2 , with LiFePO_4 cathode and an Al anode.

Current density (A.cm^{-2})	PEO	PT5	PT10	PT15
$1.6 \cdot 10^{-5}$	81.8	89.6	90	80.2
$3.2 \cdot 10^{-5}$	90.5	89.3	91.5	89.8
$6.5 \cdot 10^{-5}$	90.2	91	93.5	90.8

5.4 Solid polymer electrolyte with the optimum contents of PVAc and TiO_2

In the previous experiments, the optimum amounts of PVAc (35 wt.%) and TiO_2 (10 wt.%) were found and the effects of each component on the resistance and coulombic efficiency of the battery prototypes were discussed. In this set of results, we prepare and test a new

multicomponent PPT system containing both 35 wt.% PVAc and 10 wt.% of TiO₂ and compare the resistance and coulombic efficiency data for P(EO)₁₂LiPF₆, PEPV35, PT10 and the new PPT SPE systems. **Fig. 5.8, Fig. 5.9** and **Table 5.5** distinctly show the advantage of the new PPT electrolyte over the other formulations. The addition of 10 wt.% TiO₂ to the PEO-LiPF₆ system containing 35 wt.% PVAc reduces the resistance even more than the addition of 10 wt.% TiO₂ or 35 wt.% PVAc only. Both the coulombic efficiency and the resistance show very little variation with the number of cycles and little variation with the current density. Furthermore, this composition together with PT10 are the only ones that allowed the use of high current densities of charge and discharge with very little variations in the battery parameters and without failures.

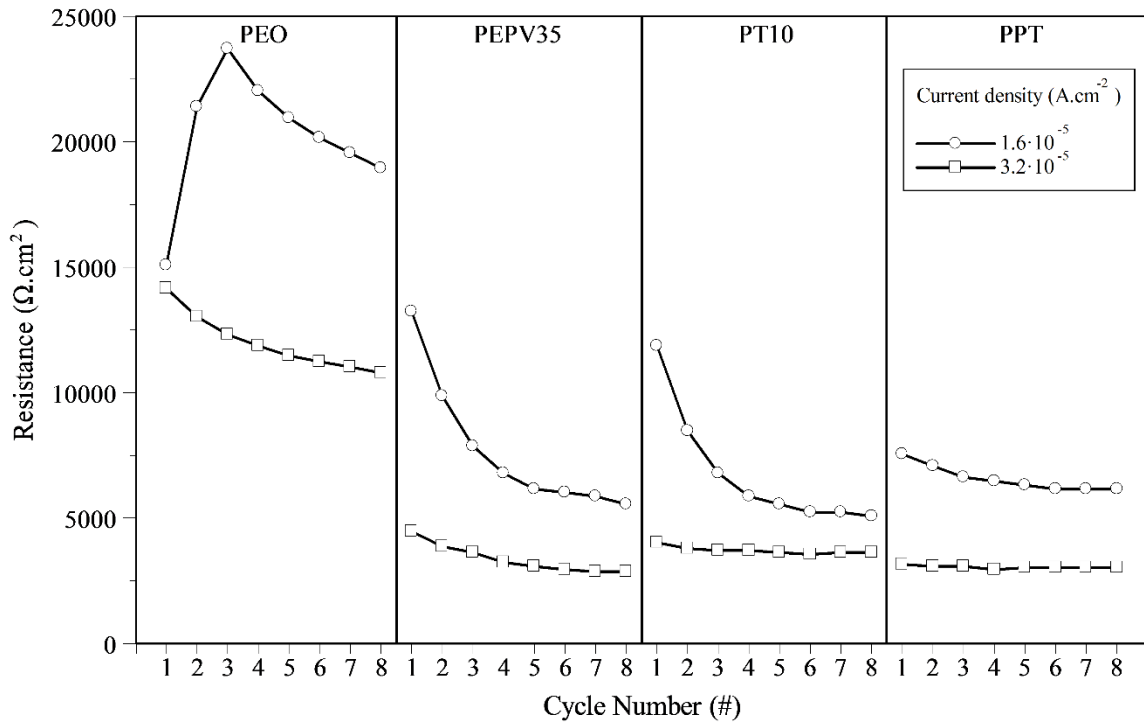


Figure 5.8: Resistance of solid polymer electrolytes with and without 10 wt.% TiO₂ and/or 35 wt.% PVAc, with LiFePO₄ cathode and an Al anode at current densities of $1.6 \cdot 10^{-5}$ and $3.2 \cdot 10^{-5}$ A.cm⁻².

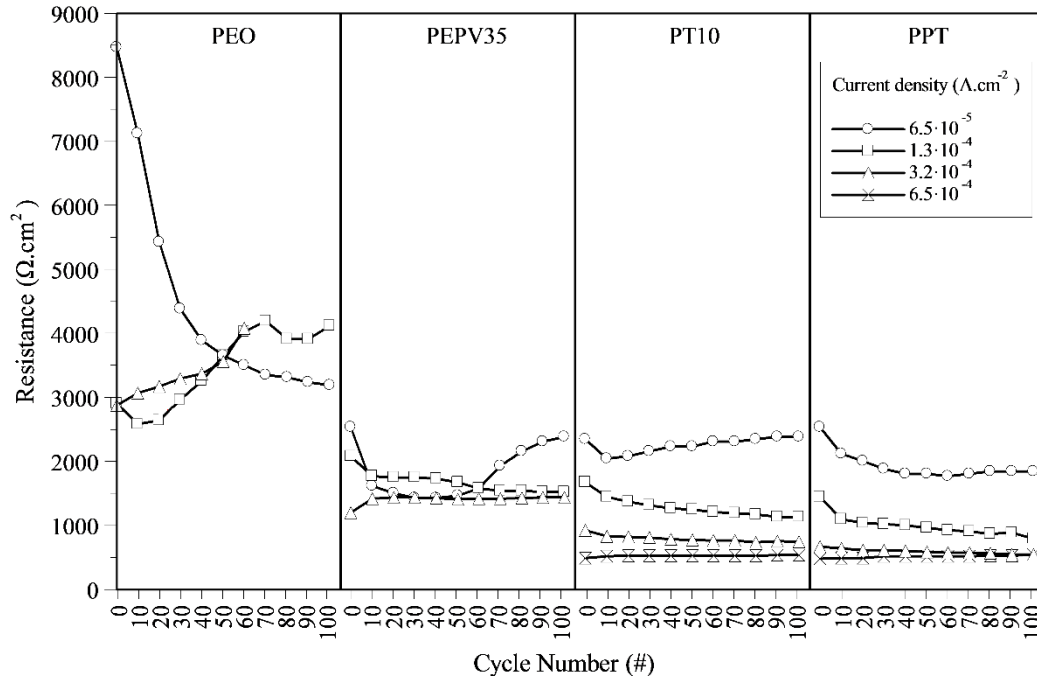


Figure 5.9: Resistance of solid polymer electrolytes with and without 10 wt.% TiO₂ and/or 35 wt.% PVAc, with LiFePO₄ cathode and an Al anode at current densities of 6.5·10⁻⁵, 1.3·10⁻⁴, 3.2·10⁻⁴, 6.4·10⁻⁴ A.cm⁻².

Table 5.5: The average Resistance (Ω.cm²) of solid polymer electrolytes with and without 10 wt.% TiO₂ and/or 35 wt.% PVAc, with LiFePO₄ cathode and an Al anode.

Current density (A.cm ⁻²)	PEO	PEPV35	PT10	PPT
1.6·10 ⁻⁵	20200	7600	6700	6500
3.2·10 ⁻⁵	11900	3300	3700	3000
6.5·10 ⁻⁵	4400	1800	2200	1900
1.3·10 ⁻⁴	3500	1700	1300	1000
3.2·10 ⁻⁴	failed	1400	800	600
6.4·10 ⁻⁴	-	-	600	500

The coulombic efficiency data are shown in Fig. 5.10, Fig. 5.11 and Table 5.6. It can be clearly seen that all prototypes exhibit higher coulombic efficiency than those based on neat PEO SPE. The addition of TiO₂ noticeably improved the coulombic efficiency, especially at high current densities. The composition with TiO₂ nanoparticles and PVAc showed an increase in the coulombic efficiency at higher current densities as compared to low current densities, which is quite unusual and correlates with the compatibility between TiO₂ and PEO-PVAc polymers matrix. It also points at high stability of LiAl nanostructure in these electrolytes.

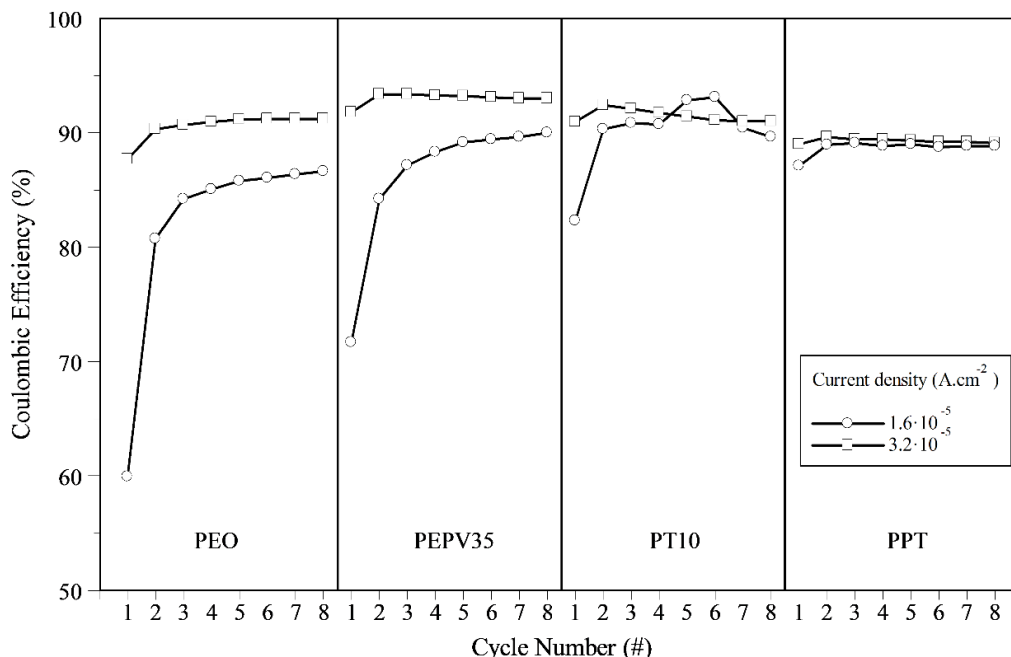


Figure 5.10: Coulombic efficiency of solid polymer electrolytes with and without 10 wt.% TiO₂ and/or 35 wt.% PVAc, with LiFePO₄ cathode and an Al anode at current densities of 1.6·10⁻⁵ and 3.2·10⁻⁵, A.cm⁻².

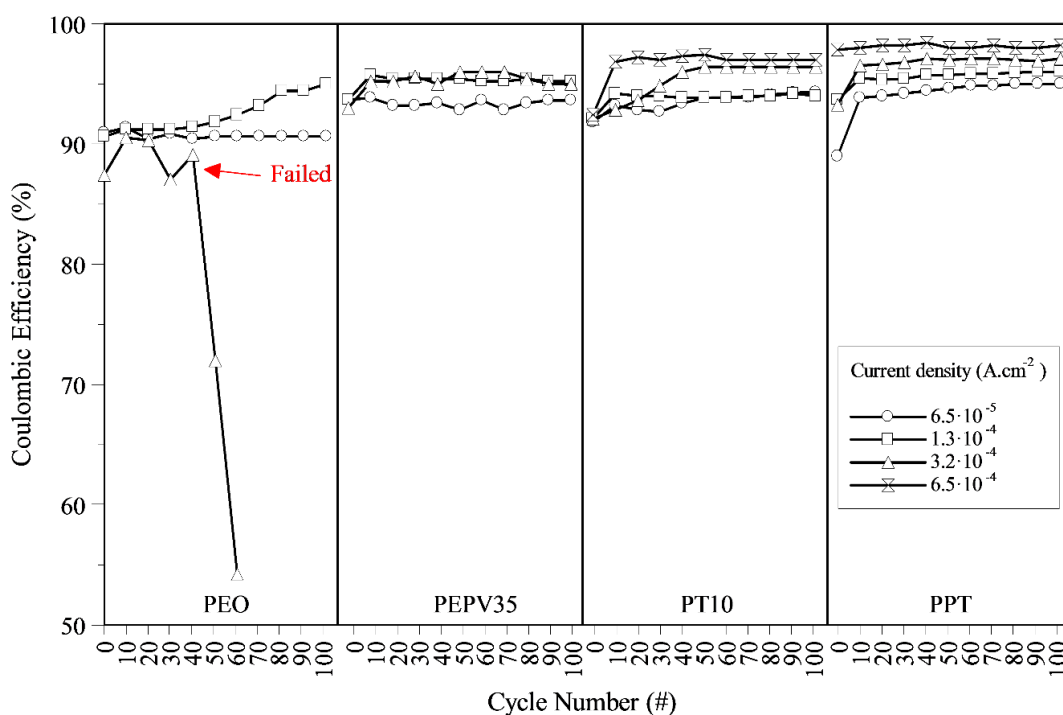


Figure 5.11: Coulombic efficiency of solid polymer electrolytes with and without 10 wt.% TiO₂ and/or 35 wt.% PVAc, with LiFePO₄ cathode and an Al anode at current densities of 6.5·10⁻⁵, 1.3·10⁻⁴, 3.2·10⁻⁴, 6.4·10⁻⁴ A.cm⁻².

Table 5.6: The average coulombic efficiency (%) of solid polymer electrolytes with and without 10 wt.% TiO₂ and/or 35 wt.% PVAc, with LiFePO₄ cathode and an Al anode.

Current density (A.cm ⁻²)	PEO	PEPV35	PT10	PPT
1.6·10 ⁻⁵	81.8	86.9	90	88.7
3.2·10 ⁻⁵	90.5	93	91.5	89.3
6.5·10 ⁻⁵	90.2	93.8	93.5	94.3
1.3·10 ⁻⁴	92.4	95	93.9	95.6
3.2·10 ⁻⁴	failed	95.2	95.2	96.7
6.4·10 ⁻⁴	-	-	96.6	98.2

5.5 Determination of the properties of the electroformed nanostructure from the resistances and discharging potentials

Fig. 5.12 shows the values of the discharging potential of different battery prototypes measured in different experiments and at different current densities. The discharging potentials were calculated from the output voltages of the battery prototypes by correcting for the IR drops. It can be clearly seen that all prototypes except PEO-based ones showed very close discharging potential values centered slightly above 3.0 V regardless of the current densities or cycle numbers. Since the corrected discharging potential in galvanic cycles should follow the Nernst equation as discussed earlier in **chapter 3**, having the same voltage at different current densities and different cycles for different samples is an indication of the presence of the same unique electroactive phase. From the electrochemical thermodynamics we know that, if a bulk phase with sufficiently high exchange current is formed, the potential will be determined by that phase and will be independent of the amount of that phase present since the activity of a bulk phase is always equal to unity irrespective of the amount of Li reacted. Therefore, this finding indicates that the lithiation-delithiation processes indeed involve the formation of a new bulk phase at the surface of Al electrodes rather than formation of some intercalation compounds or solid solutions. Most likely, this phase should be attributed to the porous nanostructured LiAl intermetallic alloy. In case of PEO, the mechanism should be different since there is a pronounced deviation from the single potential value with increasing the number of cycles. This is probably due to the formation of another phase at the electrode surface, or pronounced kinetic

limitations, which results in higher discharging voltages and higher resistances. This behavior requires further research.

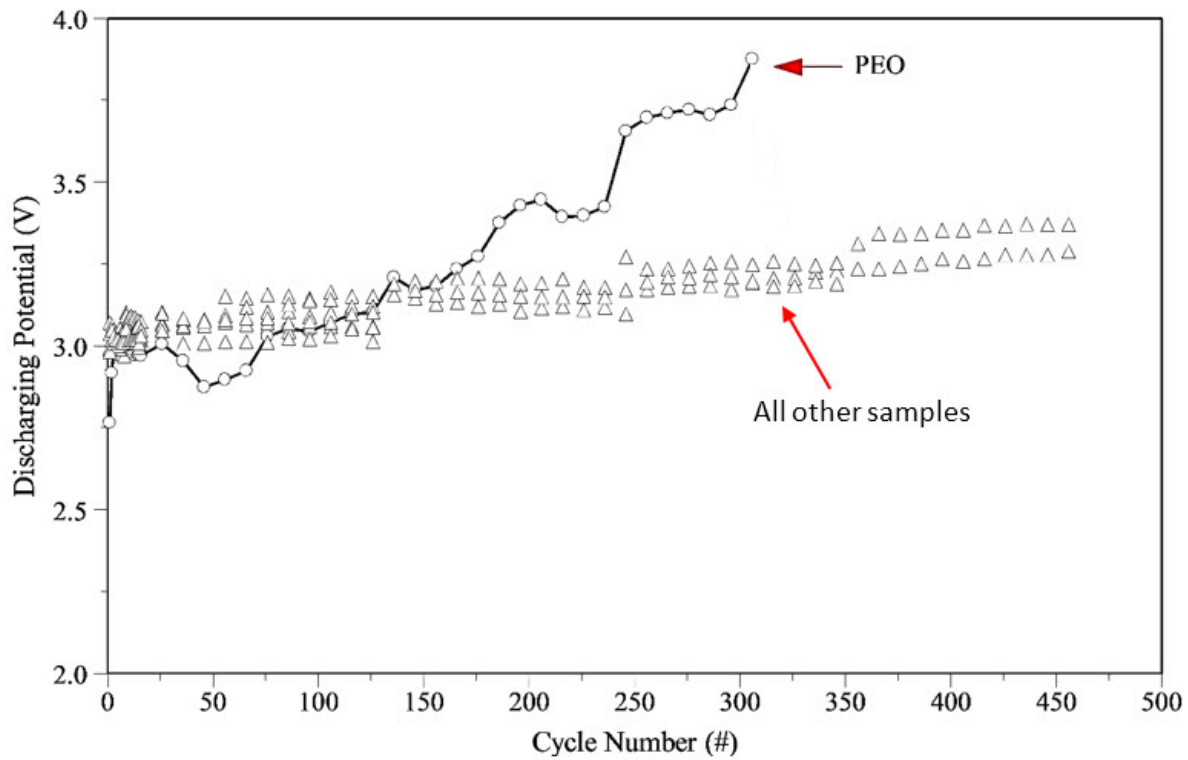


Figure 5.12: Discharging potential corrected for IR drop of all SPEs at different current densities and all the cycles.

As has been already mentioned, the resistance of the solid electrolytes in various experiments (Figs. 5.4, 5.6, 5.8, 5.9) was found to depend on the current density and cycle numbers. In particular, the resistance was found to drop at high current densities. This was attributed to the continuing formation of the porous nanostructure on the surface of bulk aluminum during the charging-discharging of the prototypes. If the changes in the electrolyte resistance were due to some degradation of the polymer electrolyte, it would be expected to increase, not decrease, at high current densities.

If we assume that the specific resistivity ρ of the electrolyte remains unchanged, the resistance R of the electrolyte can be found using the well-known equation (Eq.1):

$$R = \rho \frac{d}{A}, \quad (1)$$

where d is the distance between the electrodes, A is the contact surface area.

Since the distance d remains constant too, we must conclude that the changes in the electrolyte resistance R must be attributed to an increase in the contact area A . This is likely due to the formation of the nanostructure that penetrates the polymer electrolyte that acts as a kind of scaffold. In this context, the electrolyte resistivity can also serve as an indicator of the properties of the porous LiAl nanostructure formed at the electrode during charging-discharging and the electroformation processes. In particular, one can expect that the growth of the nanostructure will be affected by the mechanical properties of the electrolyte as well as its homogeneity. It is important to remember in this context that the battery performance is not only related to the conductivity of the electrolyte but also depends on the properties of the porous nanostructure. This indicates yet another mechanism through which the battery efficiency can depend on the structure of the solid polymer electrolyte. The properties of the electrolyte will also affect the battery failure. For instance, at increased current densities, the solid polymer electrolyte will become softer, which will facilitate the growth of the dendrites into the polymer and subsequent short-circuiting of the cell. If the polymer electrolyte is not stable enough, the battery will fail at higher current densities due to this phenomenon.

Our data indicate that the highest resistance towards failure is observed with the SPE formulations that contained TiO_2 nanoparticles (PT and the new PPT). This should be attributed to the fact that inorganic ceramic fillers like TiO_2 improve the mechanical properties and stability of the polymer electrolyte. This prevents the formation of dendrites. As follows from **Fig. 5.8** which shows galvanic cycling at low current densities where the electroformation of the new phase is most pronounced, the new PPT electrolyte system showed the smallest variation in the resistance during cycling indicating that the formation of the nanostructure was highly controlled. At the same time, the lowest resistances were found in both the new PPT and the blend PEPV35 systems indicating, among other things, the most developed contact in these conditions. These findings are supported by our SEM studies.

Shown in **Fig. 5.13 (a)-(d)** are representative SEM images of the anode surface of the battery with different solid polymer electrolytes. After cycling, the anode and cathode were separated from the electrolyte as mentioned in **section 3.7.2.1**. It can be seen that the use of different types and compositions of the electrolyte had a pronounced effect on the structure of porous regions formed on the surface of the bulk aluminum during cycling.

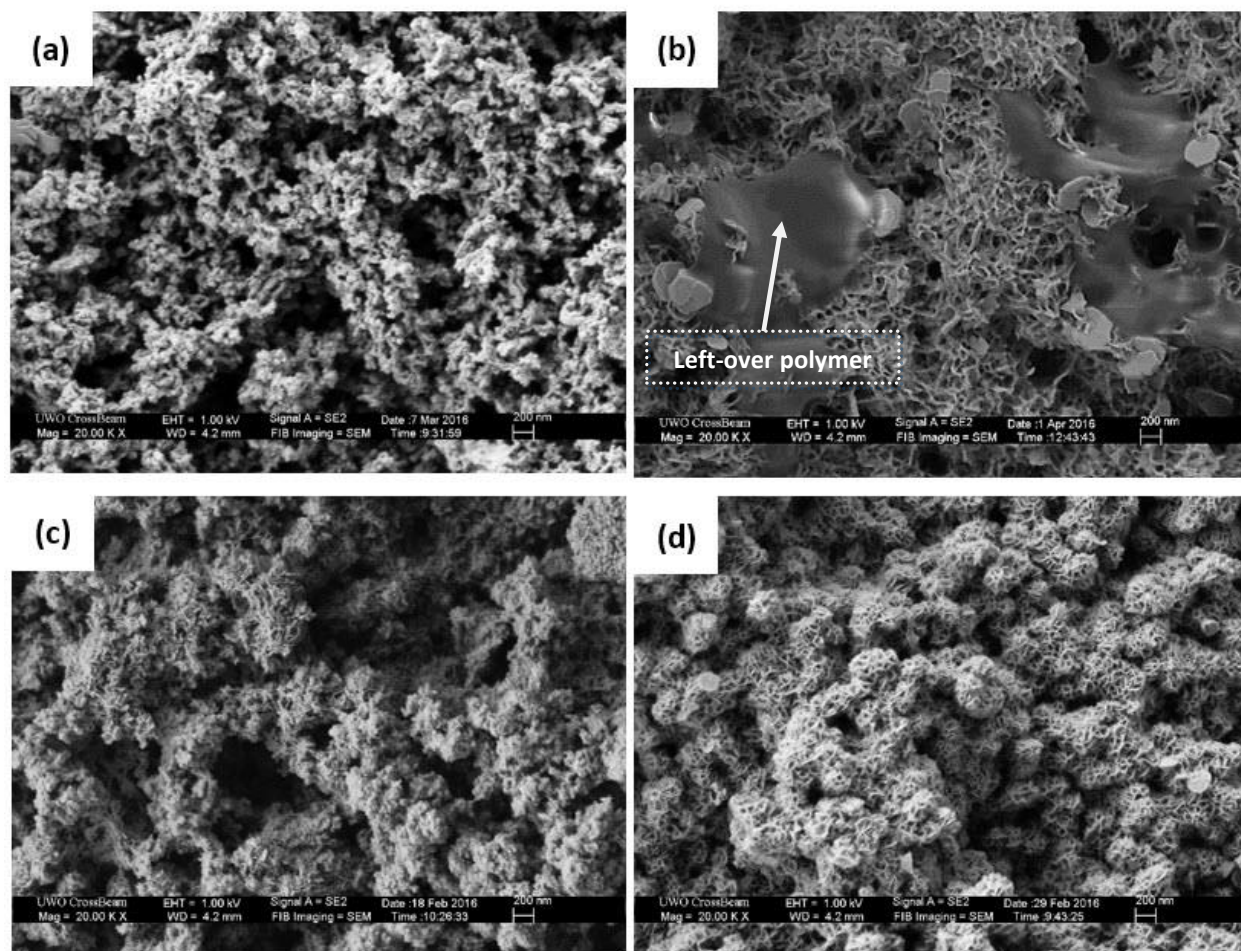


Figure 5.13: SEM image of battery anode with SPE after galvanic cycling followed by separation from the solid polymer electrolyte and cathode at 20000X magnification, (a) PEO (b) PEPV35 (c) PT10 (d) PPT.

Fig. 5.13 (a) shows the porous LiAl alloy structure obtained using PEO as a SPE in a battery prototype. The image clearly shows a highly developed dendrite structure that grew into the solid polymer electrolyte. **Fig. 5.13 (b)** shows the porous structure of the alloy that was formed during cycling of an Al anode with PEPV35 electrolyte. Parts of the alloy still covered with the polymer electrolyte are indicated by an arrow in this image. One can see that the structure is totally different and consists of a large amount of fine honeycomb-like nanopores. **Fig. 5.13 (c)** shows the structure after using PT10 as the SPE in the battery prototype. The structure looks coarser than the other images which should be related to the presence of the TiO₂ nanoparticles. These inorganic fillers are dispersed all over the SPE film and made it more mechanically stable, therefore the polymer film might exude a better control on volume expansion of the porous alloy structure. At the same time, no or very little fine honeycomb structure is seen in the image. **Fig.**

5.13 (d) shows the porous nanostructures obtained using PPT as the SPE. The alloy structure in this sample more looks like **Fig. 5.13 (b)** and clearly shows the honeycomb pores. At the same time, it is significantly rougher and sturdier, which can be again due to the presence of TiO₂ nanoparticles in its structure. We believe that it is the combination of these two factors, the presence of fine nanopores and the sturdy structure of the electroactive phase, combined with the high conductivity of the electrolyte itself, that determine the excellent performance of the battery prototypes based on the PPT electrolyte system. The first factor accounts for the excellent reversibility of the charging-discharging processes, while the second one ensures high resistance to failure at high current densities and during prolonged cycling.

5.6 The performance of the best battery prototype made using PPT solid polymer electrolyte

Based on our results described above, a Li-ion battery prototype with an Al anode, LiFePO₄ cathode and PPT electrolyte was designed. At first, the nanostructured phase was formed at low current densities to ensure the best and most uniform structure. Then the prototype was cycled for 500 cycles for 5 days at current densities from $1.6 \cdot 10^{-5}$ to $6.4 \cdot 10^{-4}$ A.cm⁻². Care was taken not to exceed the capacity of nanostructure formed at low current densities. In order to do this, the cycle duration was reduced at high current densities to keep the total charge constant. Under this conditions, this prototype showed the highest coulombic efficiency of 98% along with the lowest resistance of 500 Ω.cm². As expected, in addition to the highly conductive and amorphous structure of the solid polymer electrolyte which was improved enough (section 4.3), controlling the charging and discharging time was another reason for the great performance of this battery at high current densities. **Fig. 5.14 - Fig. 5.20** show the galvanic cycles of this battery at different current densities. In general, comparable battery performance at all current densities was observed. The charge/discharge response was reasonably stable and the coulombic efficiency exceeded 98%. No indications of a failure were observed after 500 cycles even at the highest current densities. It is important to stress this type of behavior cannot be achieved with batteries using PEO polymer electrolyte, at least with the samples examined under comparable conditions in our laboratory. Therefore, our careful design of the solid polymer electrolyte for battery prototypes allowed us to greatly improve their performance and achieve high reversibility, cyclability and stable performance without failure even at high current densities.

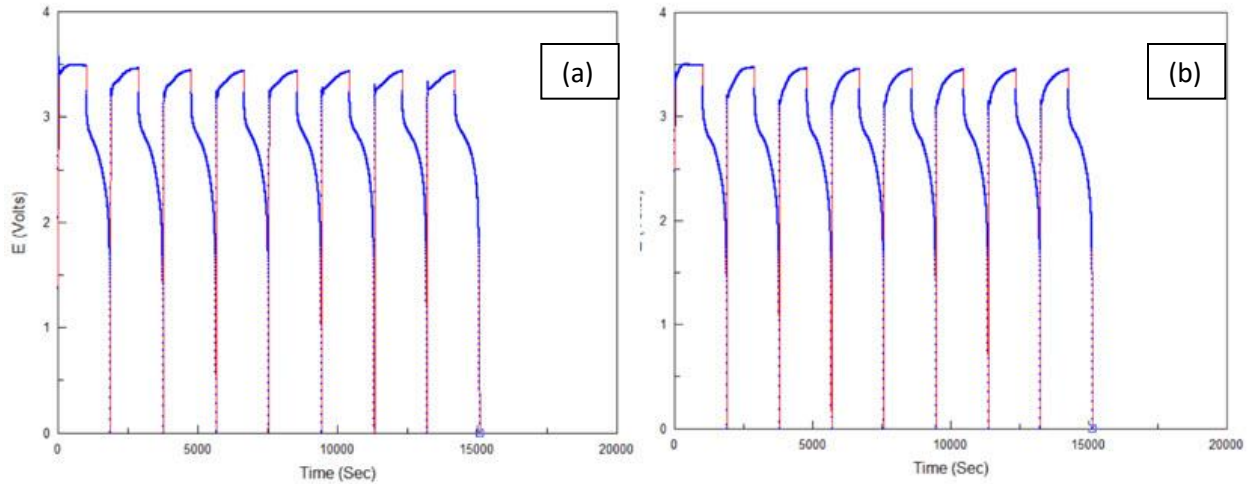


Figure 5.14: Battery galvanic cycles of sample with a PPT solid polymer electrolyte, LiFePO₄ cathode and an Al anode at current density of (a) $1.6 \cdot 10^{-5} \text{ A.cm}^{-2}$ for 8 cycles and (b) $3.2 \cdot 10^{-5} \text{ A.cm}^{-2}$ for 8 cycles.

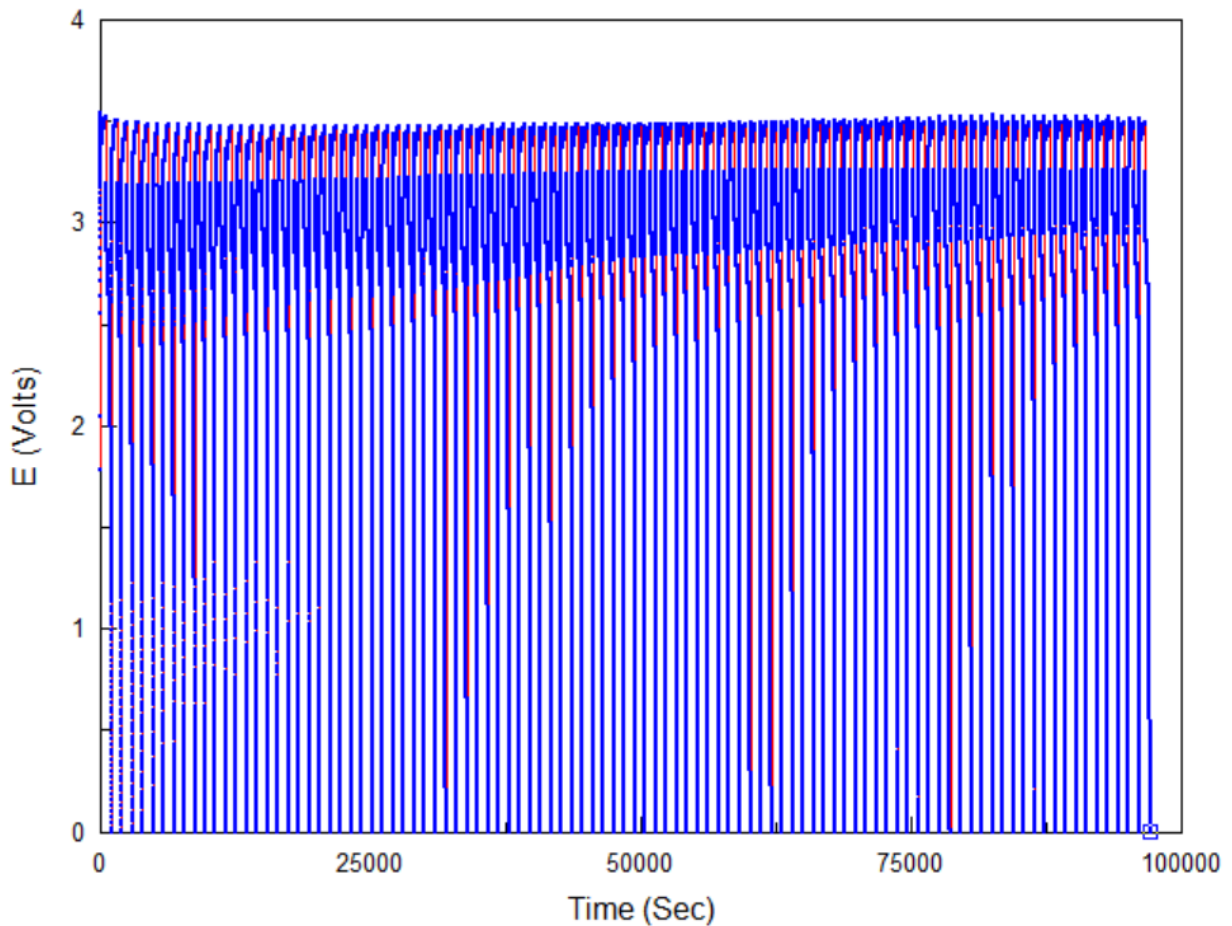


Figure 5.15: Battery galvanic cycles of sample with a PPT solid polymer electrolyte, LiFePO₄ cathode and an Al anode at current density of $6.5 \cdot 10^{-5} \text{ A.cm}^{-2}$ for 100 cycles.

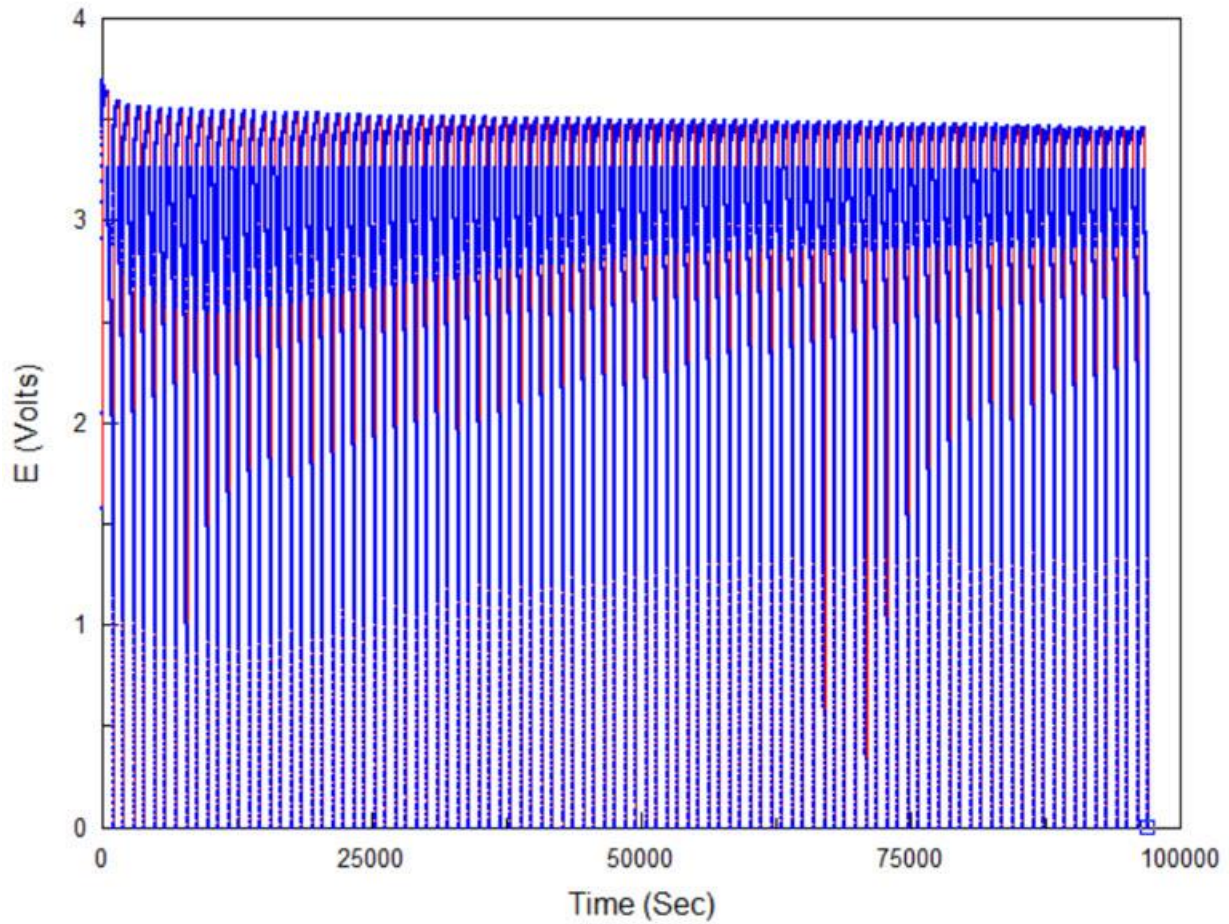


Figure 5.16: Battery galvanic cycles of sample with a PPT solid polymer electrolyte, LiFePO₄ cathode and an Al anode at current density of $1.3 \cdot 10^{-4} \text{ A.cm}^{-2}$ for further 100 cycles.

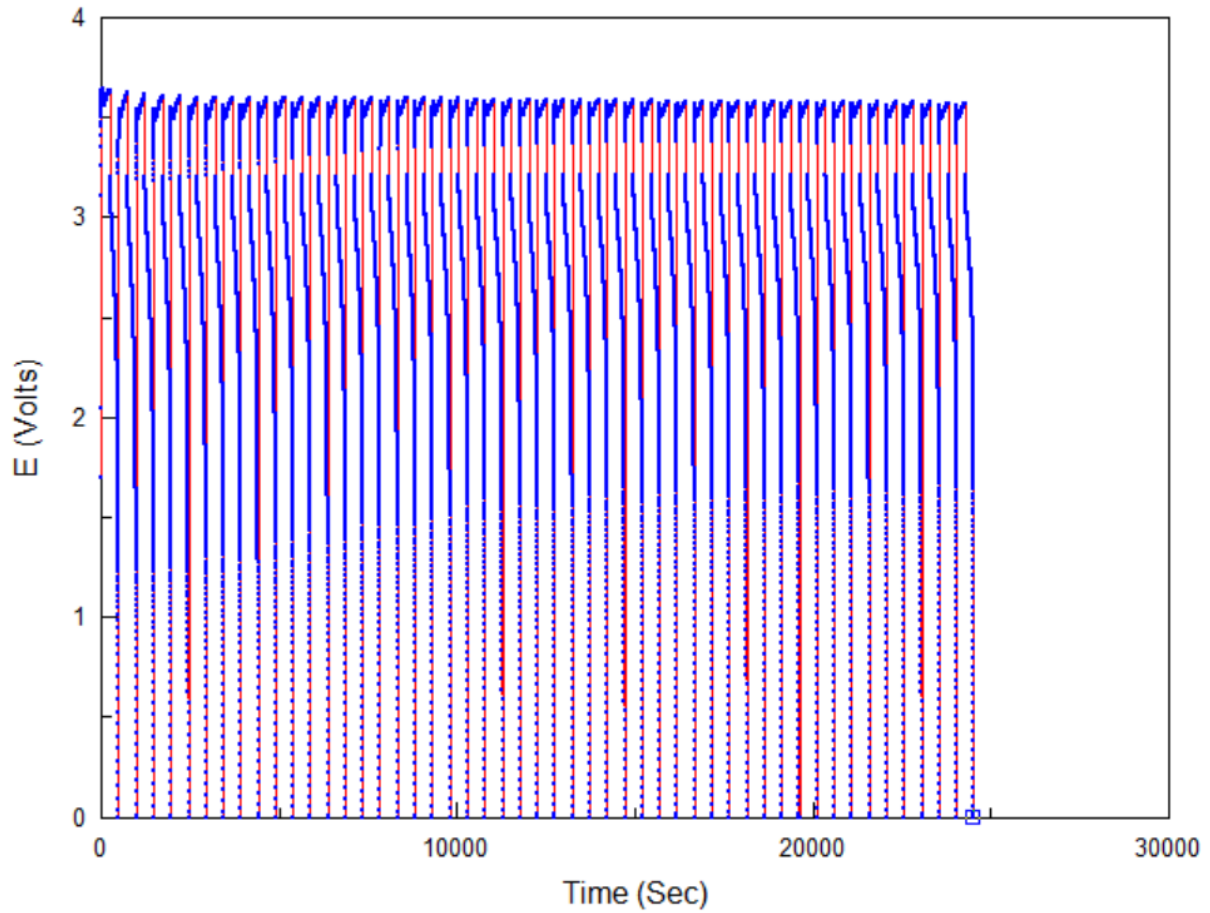


Figure 5.17: Battery galvanic cycles of sample with a PPT solid polymer electrolyte, LiFePO_4 cathode and an Al anode at current density of $3.2 \cdot 10^{-4} \text{ A.cm}^{-2}$ for further 50 cycles.

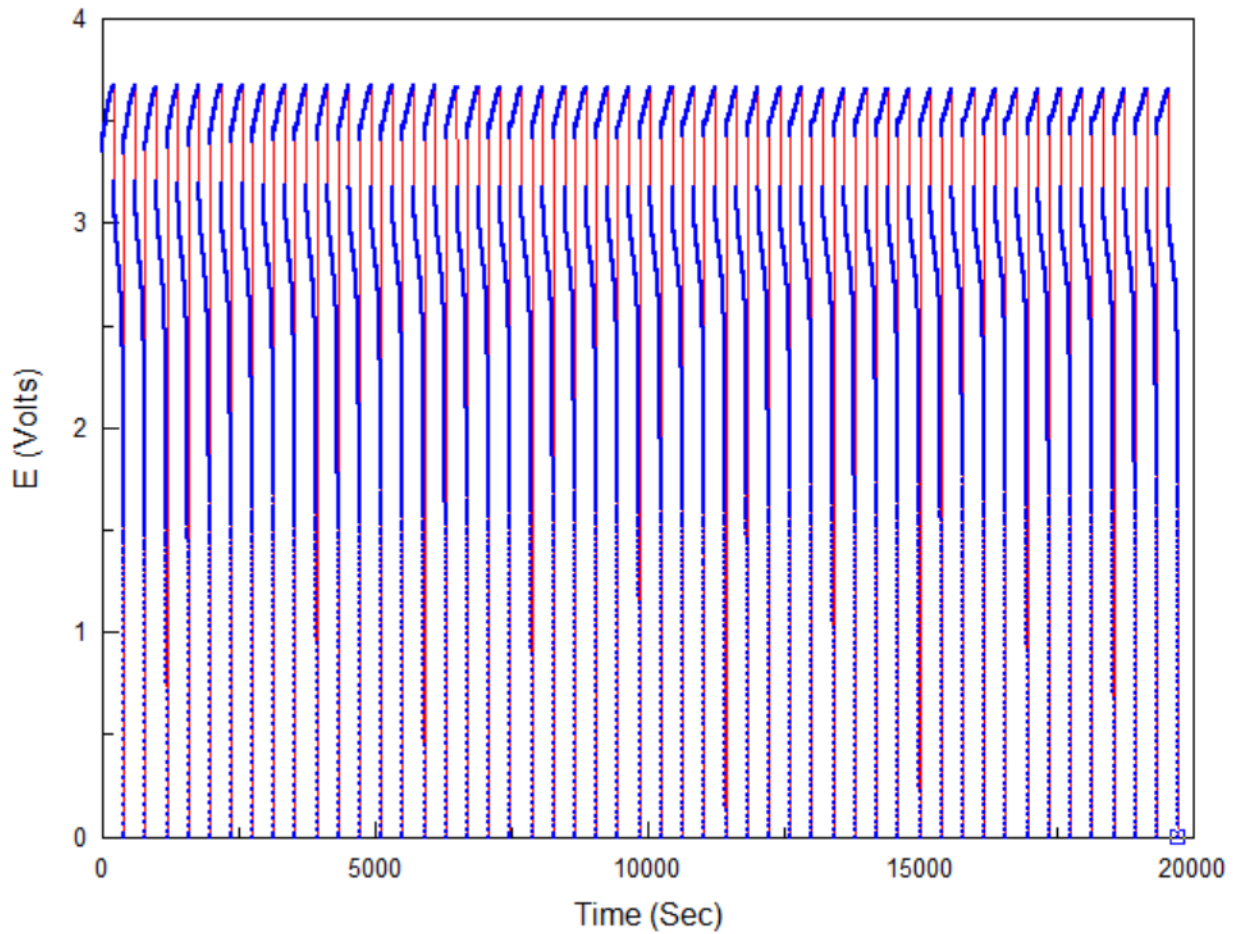


Figure 5.18: Battery galvanic cycles of sample with a PPT solid polymer electrolyte, LiFePO₄ cathode and an Al anode at current density of $4.5 \cdot 10^{-4}$ A.cm⁻² for further 50 cycles.

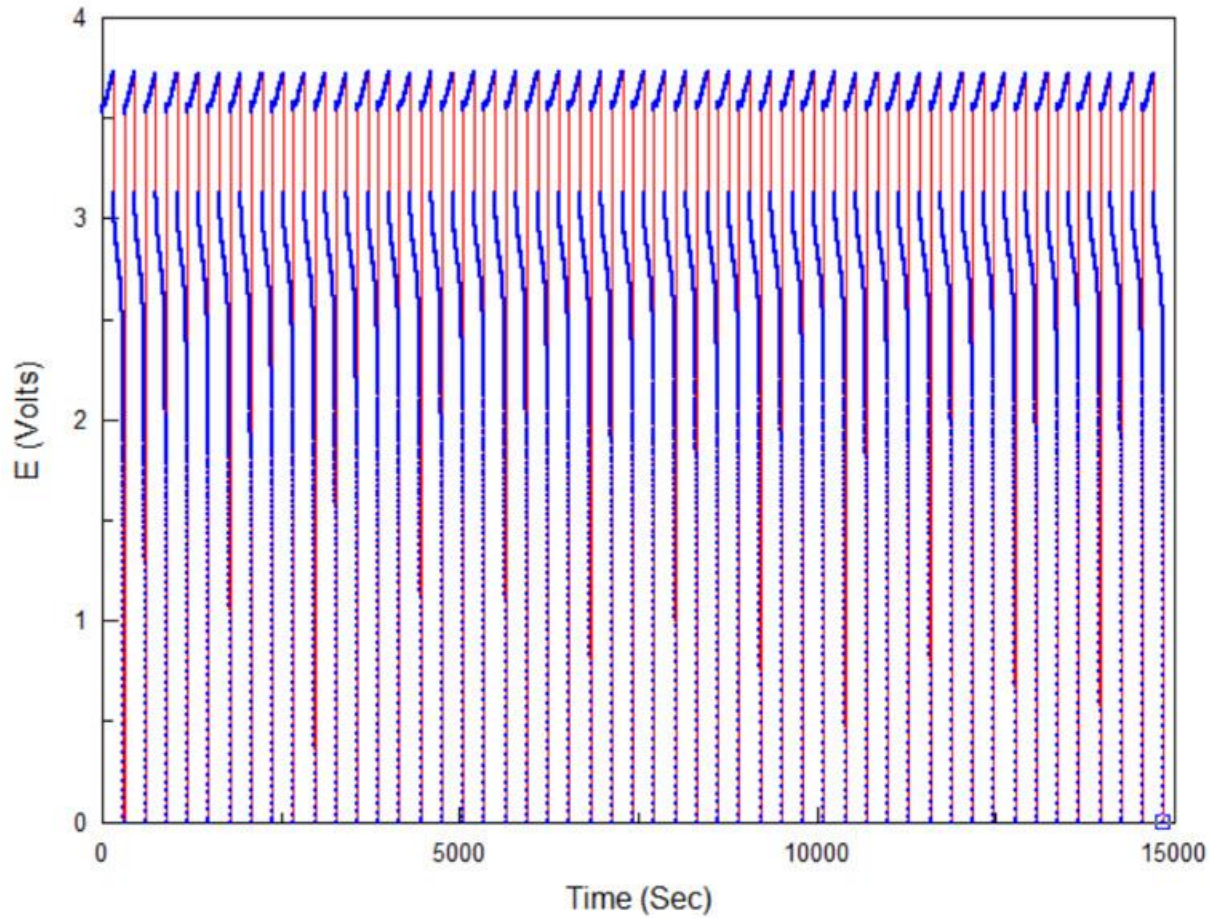


Figure 5.19: Battery galvanic cycles of sample with a PPT solid polymer electrolyte, LiFePO_4 cathode and an Al anode at current density of $5.8 \cdot 10^{-4} \text{ A.cm}^{-2}$ for further 50 cycles.

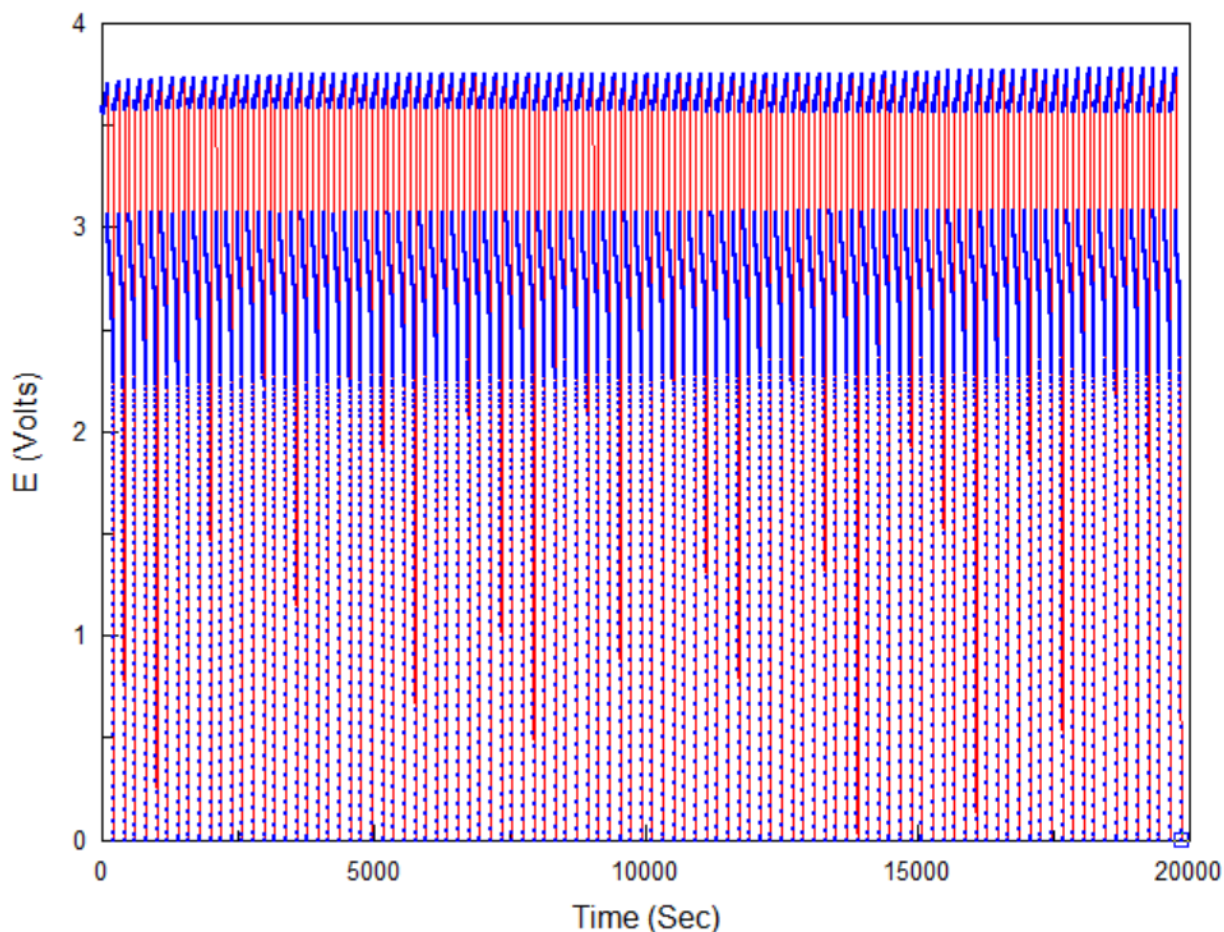


Figure 5.20: Battery galvanic cycles of sample with a PPT solid polymer electrolyte, LiFePO_4 cathode and an Al anode at current density of $6.5 \cdot 10^{-4} \text{ A.cm}^{-2}$ for further 100 cycles.

5.7 References

1. Reddeppa, N.; Reddy, T. J. R.; Achari, V. B. S.; Rao, V. V. R. N.; Sharma, A. K., *Ionics*, **2009**, *15*, 2, 255-259.
2. Fragiadakis, D.; Runt, J., *Macromolecules*, **2010**, *43*, 2, 1028-1034.
3. Ulaganathan, M.; Pethaiah, S. S.; Rajendran, S., *Materials Chemistry and Physics*, **2011**, *129*, 1-2, 471-476.
4. Rajendran, S.; Bama, V. S.; Prabhu, M. R., *Ionics*, **2010**, *16*, 3, 283-287.
5. Animitsa, I. E.; Kruglyashov, A. L.; Bushkova, O. V.; Zhukovsky, V. M., *Solid State Ionics*, **1998**, *106*, 3-4, 321-327.
6. Zhou, S.; Kim, D., *Polymers for Advanced Technologies*, **2011**, *22*, 12, 2130-2135.
7. Henry, R. M.; Ford, C. A.; Pyati, R., *Solid State Ionics*, **2002**, *146*, 1-2, 151-156.
8. Croce, F.; Persi, L.; Ronci, F.; Scrosati, B., *Solid State Ionics*, **2000**, *135*, 1-4, 47-52.
9. Capiglia, C.; Mustarelli, P.; Quartarone, E.; Tomasi, C.; Magistris, A., *Solid State Ionics*, **1999**, *118*, 1-2, 73-79.

10. Wieczorek, W.; Zalewska, A.; Raducha, D.; Florjańczyk, Z.; Stevens, J. R., *The Journal of Physical Chemistry B*, **1998**, *102*, 2, 352-360.
11. Chiang, C.-Y.; Jaipal Reddy, M.; Chu, P. P., *Solid State Ionics*, **2004**, *175*, 1-4, 631-635.
12. Manuel Stephan, A.; Nahm, K. S., *Polymer*, **2006**, *47*, 16, 5952-5964.
13. Yarmolenko, O. V.; Khatmullina, K. G.; Bogdanova, L. M.; Shuvalova, N. I.; Dzhavadyan, E. A.; Marinin, A. A.; Volkov, V. I., *Russian Journal of Electrochemistry*, **2014**, *50*, 4, 336-344.
14. Ahn, J. H.; Wang, G. X.; Liu, H. K.; Dou, S. X., *Journal of Power Sources*, **2003**, *119-121*, 422-426.
15. Zhou, J.; Gao, D.; Li, Z.; Lei, G.; Zhao, T.; Yi, X., Nanocomposite polymer electrolytes prepared by in situ polymerization on the surface of nanoparticles for lithium-ion polymer batteries. In *Pure and Applied Chemistry*, 2010; Vol. 82, p 2167.

Chapter 6

6 CONCLUSIONS AND FUTURE WORK

Using solid polymer electrolytes (SPEs) in lithium-ion batteries has numerous advantages. It is even more true for our systems with Al-based anodes that exhibit pronounced volume changes during charging-discharging. In such systems, in addition to providing ionic conductivity, SPEs could act as a mechanical scaffold and help to control the pulverization of active material and dendrite formation. However, SPEs typically suffer from very poor room temperature ionic conductivity ($\sigma < 10^{-7}$ S/cm). To address this deficiency, three types of solid polymer electrolytes have been developed based on PEO to enhance lithium ion conductivities at ambient temperatures: (i) blends of high molecular weight PEO and low molecular weight PVAc; (ii) composites of high molecular weight PEO and TiO₂ nanoparticles; and (iii) blend-based composite electrolytes consisting of PEO and PVAc with dispersed TiO₂.

The concentration dependencies of resistance and coulombic efficiency were determined from galvanic cycles for PEO blends with 15, 35, and 50 wt.% PVAc polymer electrolytes (PEPV15, PEPV35, PEPV50) as well as neat (PEO). Calorimetric data showed the crystallization of PEO was easily suppressed by blending it with PVAc. The miscibility of PVAc-PEO blends was confirmed by the depression of crystallization rate and melting point and the single T_g of the blend. The blends were all viscoelastic, with mechanical strengths increasing with decreasing PVAc concentration due to decreased crystallinity and dilution of the polymer blends. The crystallinity and ambient temperature resistance of these blends were found to decrease with an increase in the PVAc content, while the mechanical stability and coulombic efficiency were limited by the amount of PVAc that could be incorporated into the PEO. The blend of 35 wt.% PVAc and 65 wt.% PEO (PEPV35) demonstrated a low resistance ($1800 \Omega \cdot \text{cm}^2$ at high current density) as well as high coulombic efficiency (94%). Therefore, PEPV35 appeared to be most suitable for the reversibility of lithiation/delithiation and controlling the growth of the LiAl alloy nanostructure on the aluminum surface, as well as for Li transportation through the film. SEM images showed that using PEO as a SPE in a battery prototype exhibited the porous LiAl alloy and a highly developed dendrite structure that grew into the solid polymer electrolyte, whereas the porous structure of the alloy that was formed during cycling of an Al anode with PEPV35

electrolyte showed a totally different structure with a large amount of fine honeycomb-like nanopores.

The effects of the addition of inorganic nanocrystalline fillers to the solid polymer electrolytes were also investigated. Compositions containing various amounts of TiO₂ nanoparticles in PEO-based solid polymer electrolytes were prepared and the values of the resistance and coulombic efficiency of the battery prototypes were calculated from the galvanic cycles. Calorimetric data showed that adding TiO₂ nanoparticles to P(EO)₁₂-LiPF₆ matrix system resulted in an excellent thermal stability of the SPEs. The best results were achieved at lower concentrations of TiO₂ nanoparticles (up to 10 wt.%). The nanoparticles were more compatible with PEO matrix, as indicated by the lowered crystallinity, T_g, T_m and the bulk electrolyte resistance. At high concentrations of TiO₂, a negligible decrease in crystallinity was observed due to TiO₂ nanoparticles acting as nucleation centers of the crystalline polymer phase in the PEO matrix.

All prototypes with TiO₂ exhibited higher coulombic efficiency than those based on neat PEO SPE due to the presence of inorganic fillers which improved the conductivity and mechanical stability. These considerations point out that an optimum concentration of TiO₂ nanoparticles yields the lowest resistance as well as high efficiency values in a composite polymer electrolyte. Incorporation of 10 wt.% TiO₂ into PEO-based polymer electrolyte produced the resistance as low as 2200 Ω.cm² and the coulombic efficiency as high as 94%. Therefore, the optimal concentration of TiO₂ nanofiller was determined to be 10 wt.%. SEM images indicated a coarser and sturdier structure of LiAl alloy formed on the surface of Al anodes in electrolytes containing TiO₂ nanoparticles.

After finding the optimum amounts of PVAc (35 wt.%) and TiO₂ (10 wt.%), a new multicomponent PPT solid polymer electrolyte composition containing both 35 wt.% PVAc and 10 wt.% of TiO₂ was designed. The new electrolyte had an amorphous structure with a crystallinity as low as 0.19%, the glass transition temperature of -36.21°C and an excellent thermal stability. Li-ion battery prototype using this electrolyte showed the highest coulombic efficiency of 98% along with the lowest resistance of 500 Ω.cm² as well as an excellent cycling ability. No indications of a failure were observed after 500 cycles even at the highest current densities. The addition of TiO₂ noticeably improved the coulombic efficiency, especially at high

current densities. The SEM images showed that the LiAl alloy structure contained the honeycomb nanopores which have been seen in the LiAl nanostructure with PVAc-based SPE combined with the sturdy and robust structure due to the presence of TiO₂ nanoparticles.

In summary, new efficient formulations of solid polymer electrolytes for lithium-ion batteries were prepared and tested. Practical battery prototypes using these electrolytes were fabricated and their performance was evaluated. The prototypes with the optimized electrolytes showed high coulombic efficiency and cycling ability for over 500 cycles even at high current densities. It was demonstrated that solid polymer electrolyte could efficiently control the growth and volume changes associated with charging-discharging in lithium-ion battery electrodes and prevent pulverization of the active material.

Future work in this area will focus on further optimization of the properties of electrolytes and search for the way to further improve their conductivity and mechanical properties. More extensive battery testing at high current densities will be also required. The failure mechanisms will need to be investigated in more detail.

Curriculum Vitae

Name: Ladan Eskandarian

Post-secondary Education and Degree: The University of Western Ontario
London, Ontario, Canada
2014-2016 M.Sc. Physical Chemistry

Amirkabir University of Technology (Tehran Polytechnic)
Tehran, Iran
2009-2013 B.Sc. Textile Engineering (textile chemistry and fiber science)

Related Work Experience: Teaching Assistant
The University of Western Ontario
2014-2016

Chemistry 1301A: First Year Chemistry Laboratory	2014-2015
Chemistry 1302B: First Year Chemistry Laboratory	2015
Chemistry 2384B: Second Year Chemistry Laboratory	2016

- Publications:**
1. L.Eskandarian, M. Arami, E.Pajootan, Evaluation of Adsorption Characteristics of Multiwalled Carbon Nanotube Modified by a Poly(propylene imine) Dendrimer in Single and Multiple Dye Solutions: Isotherms, Kinetics, and Thermodynamics, J. Chem. Eng. Data 59 (2014) 444-454.
 2. L. Eskandarian, E. Pajootan, M. Arami, Novel Super Adsorbent Molecules, Carbon Nanotubes Modified by Dendrimer Miniature Structure, for the Removal of Trace Organic Dyes, Ind. Eng. Chem. Res. 53 (2014) 14841-14853.
 3. S. A. Iranagh, L. Eskandarian, R. Mohammadi, Synthesis of MnO₂-Polyaniline Nanofiber Composites to Produce High Conductive Polymer, Synth. Met. 172 (2013) 49-53.